UNIVERSITA' DI PADOVA  FACOLTA' DI INGEGNERIA

Dipartimento di Ingegneria dell'Informazione

Scuola di Dottorato di Ricerca in Ingegneria dell'Informazione
Indirizzo: Bioingegneria

CICLO XXIII

DESIGN AND DEVELOPMENT OF ALGORITHMS AND WEB-BASED APPLICATIONS FOR THE TRACKING OF VASCULAR STRUCTURES AND FOR THE ASSESSMENT OF CLINICAL PARAMETERS IN RETINAL IMAGES

Direttore della Scuola: Ch.mo Prof. Matteo Bertocco

Supervisore: Ch.mo Prof. Alfredo Ruggeri

Dottorando: Diego Fiorin

To Irene
and to my parents

Contents

List of Figures

List of Tables

Sommario

Questa tesi tratta l'analisi automatica di immagini a colori del fondo dell'occhio. In particolare, essa si focalizza sull'implementazione di software per l'analisi e la valutazione quantitativa delle retinopatie, prevalentemente ipertensiva e diabetica su soggetti adulti e retinopatia della prematurità (ROP) su soggetti nati prematuri.

Sia l'ipertensione che il diabete colpiscono, anche se con modalità e decorso temporale differente, il microcircolo sanguigno. La retinopatia è una delle conseguenze di tale danno circolatorio. I vasi retinici sono assai sensibili a cambiamenti nella microcircolazione: è stato dimostrato che i singoli segni della retinopatia hanno un alto valore prognostico per infarto, sclerosi carotidea e danno coronarico. Anche nel caso di neonati altamente pretermine, nei quali la vascolarizzazione retinica è inizialmente incompleta e può svilupparsi succesivamente in modo anomalo, i segni della retinopatia risultano importanti per una valutazione della sua gravità e per la prevenzione di potenziali peggioramenti che possono compromettere le capacità visive del soggetto. Inoltre, la retinopatia è una malattia sociale, con una ricaduta economica (diretta ed indiretta) elevata: la perdita o la diminuzione della capacità visiva porta infatti ad una ridotta capacità lavorativa ed all'impossibilità di condurre una vita indipendente.

Nonostante anche altri organi siano sensibili ad alterazioni del microcircolo sanguigno, la retina ha il grande vantaggio di essere facilmente disponibile ad un controllo non invasivo. Tale caratteristica suggerisce un modo efficiente ed efficace per seguire il decorso di malattie locali e sistemiche associate alla retinopatia. Inoltre, con riguardo alla prevenzione della perdita della vista, il riconoscimento della retinopatia al suo insorgere è il punto più critico per evitare che degeneri in cecità. Ciò è particolarmente importante nella retinopatia diabetica in cui, allo stato attuale della farmacologia, i danni alla retina non recedono con il trattamento farmacologico o col controllo del diabete.

Sfortunatamente, le fasi iniziali della retinopatia, sia negli adulti che nei neonati, sono quasi asintomatiche. Un programma di *screening* potrebbe evitare, alla maggior parte della popolazione a rischio, lo sviluppo di retinopatie che minaccino la vista. Allo stesso tempo, nel mondo occidentale non ci sono abbastanza risorse, sia in termine di tempo e soprattutto in termine di disponibiltà di oftalmologi esperti, per organizzare uno *screening* di tal genere. E' dunque forte il bisogno di strumenti che valutino automaticamente la retina, per diagnosticare la presenza e la severità dell'eventuale retinopatia.

Nell'ambito di questa tesi sono state prese in esame le *features* dell'apparato vascolare: l'identificazione del reticolo dei vasi (arterie e vene), consente la misurazione dei suoi principali descrittori geometrici (lunghezza, direzione, calibro, presenza di biforcazioni, tortuosità, etc.); da questi vengono calcolati specifici indici di rilievo diagnostico, che forniscono ai clinici informazioni sul grado complessivo di

retinopatia del paziente, la cui significatività è molto importante per la diagnosi delle patologie retiniche.

Lo strumento utilizzato per acquisire le immagini del fondo retinco è la fundus camera, un microscopio a bassa potenza accoppiato con una fotocamera, progettato per fotografare la superficie interna dell'occhio. L'acquisizione su pazienti adulti per l'identificazione o lo screening di retinopatia è solitamente effettuato con fundus camere non portatili a contatto, che forniscono immagini ad alta risoluzione ad un field of view (FOV) compreso tra i 30 e i 60 gradi. Diversamente, l'acquisizione su neonati prematuri per lo screening di ROP viene fatta usando strumenti ad-hoc con caratteristiche particolari. Ne è un esempio la fundus camera portatile NidekNM200D (Nidek Co., Gamagori, Japan) che non richiede il contatto diretto con l'occhio e che produce immagini ad alta risoluzione e stretto field of view (30 gradi). Un'altra fundus camera tipicamente usata per l'acquisizione di immagini su neonati è RetCam (Clarity Medical System, Pleasanton, CA, USA), che fornisce immagini a bassa risoluzione con field of view fino a 130 gradi. L'utilizzo di RetCam è generalmente limitato ai neonati in virtù della minima opacità di cornea e cristallino e per ragioni di qualità dell'immagine non è solitamente usata con soggetti adulti.

Le immagini acquisite su adulti e su neonati presentano diverse caratteristiche, legate essenzialmente alle differenze anatomiche tra le due classi di soggetti, ai diversi tipi di fundus camera usata e ai diversi protocolli di acquisizione. Di conseguenza, algoritmi che risultano molto efficienti per l'analisi di immagini di soggetti adulti, spesso si rivelano inadeguati se applicati a immagini di neonati. Per questo motivo, allo scopo di garantire sempre una stima accurata e precisa dei parametri clinici estratti, sono stati sviluppati algoritmi *ad-hoc* per i diversi tipi di immagini da analizzare. In particolare in questa tesi vengono presentati tre sistemi, progettati rispettivamente per l'analisi di immagini di soggetti adulti, immagini acquisite da neonati con Nidek NM200D e immagini di neonati acquisite con RetCam.

Viene presentato un nuovo metodo per estrarre automaticamente la rete vascolare su immagini di adulti, acquisite a diverse risoluzioni e field of view. Questo si basa su una tecnica di ricerca multi-direzionale su grafi, per l'identificazione degli assi dei vasi: dopo la ricerca sull'immagine di punti notevoli (*seed points*) i cammini a costo minimo che connettono diversi *seeds* identificano gli assi dei vasi. . I bordi vengono poi trovati applicando filtri matched monodimensionali efficienti: la direzione del kernel è scelta perpendicolarmente agli assi trovati e la scala viene stimata mediante un'analisi preliminare dei profili trasversali ai vasi.

A causa della grande variabilità e la scarsa qualità delle immagini acquisite su neonati con Nidek NM200D, è stato sviluppato un sistema semi-automatico *ad-hoc* per tracciare singoli segmenti vascolari e valutarne le caratteristiche geometriche. I vasi da analizzare vengono selezionati manulamente delineandone l'asse approssimativo. A partire da questa informazione *a priori* i bordi dei vasi vengono trovati mediante tecniche di filtraggio basate sul metodo di Canny. I calibri e l'asse preciso lungo il segmento analizzato vengono valutati associando opportunamente coppie di punti appartenenti ai bordi opposti.

Il tracciamento automatico dei vasi in immagini acquisite su neonati con RetCam è un compito particolarmente complesso a causa della bassa risoluzione, dello scarso contrasto, del field of view particolarmente ampio e della visibilità dei vasi della coroide. Per questo scopo viene presentata una tecnica innovativa. Questa si basa sul miglioramento del contrasto tra strutture vascolari e sfondo utilizzando filtri matched con diversi kernel orientabili e scalabili. Una sogliatura locale e operazioni morfologiche vengono usate per l'estrazione degli assi della rete vascolare a partire dai filtraggi precedentemente menzionati. L'ultimo passaggio consiste in una classificazione supervisionata, basata su Support Vector Machines (SVM), allo scopo di riconoscere e scartare i falsi vasi, generati da rumore, artefatti o dalla presenza dei vasi della coroide sottostanti alla retina.

A partire dagli algoritmi sviluppati, sono stati progettati dei sistemi software allo scopo di proporre ai clinici e ai ricercatori degli strumenti, pratici e intuitivi, per la diagnosi e lo screening di retinopatie. In particolare, per l'analisi di immagini acquisite su soggetti adulti è stato sviluppato AVRnet, un sistema web dotato di un'interfaccia grafica *user-friendly* che permette di estrarre la rete vascolare e calcolare a partire da essa gli indici CRAE (Central Retinal Arteriolar Equivalent), CRVE (Central Retinal Venular Equivalent) e AVR (Arteriolar Venular Ratio) secondo il metodo di Knudtson. Per l'analisi di immagini acquisite da neonati è stato sviluppato ROPnet, un'applicazione web per la stima di indici clinici (come l'allargamento vascolare e la tortuosità) utili a definire la presenza e l'eventuale gravità della ROP. Il tool in questione è specifico per l'analisi di immagini acquisite con Nidek NM200D e le analisi possono essere effettuate con un setup di tipo *client-server* usando un web browser. Attualmente è in fase di sviluppo un analogo strumento specifico per lavorare su immagini ad ampio field of view acquisite con RetCam.

Il software riguardante l'identificazione delle strutture vascolari retiniche su immagini di adulti è stato testato su diversi datasets ed il confronto tra i risultati automatici prodotti, contro i riferimenti manuali, ha evidenziato alte sensitività e specificità. Il sistema in questione è al momento oggetto di valutazione clinica presso il Department of Ophthalmology and Visual Sciences, University of Wisconsin, USA, il cui Fundus Photograph Reading Center valuterà la possibilità di acquisire il programma come standard per la determinazione di features diagnostiche. Un'ulteriore collaborazione, con il Department of Twin Research & Genetic Epidemiology, del King's College London Division of Genetics and Molecular Medicine, St Thomas' Hospital, UK, ha portato all'analisi con il sistema sviluppato di più di 2000 immagini di fundus retinico per scopi clinici.

L'interfaccia e le funzionalità del tool web ROPnet sono state progettate in stretta collaborazione con il Department of Ophthalmology del Children's Hospital e dello Scheie Eye Institute di Philadelphia, US, allo scopo di soddisfare le esigenze dei clinici, sia per quanto riguarda l'usabilità sia per le prestazioni dello strumento. L'accuratezza dei parametri estratti da ROPnet (calibro e tortuosità dei vasi) è stata confermata dall'elevata correlazione ottenuta confrontando i risultati automatici con

quelli di riferimento, calcolati manualmente da esperti retinici. Inoltre l'applicazione web è già stata utilizzata per alcuni studi clinici preliminari e attualmente stiamo indagando l'utilità e la validità di tali parametri nella diagnosi clinica e nella classificazione della ROP.

Le specifiche del sistema per la valutazione di ROP in immagini acquisite con RetCam sono state concordate direttamente con Clarity Medical Systems, la casa produttrice della fundus camera in questione. Per questo recente progetto, come risultati preliminari abbiamo ottenuto un'alta sensitività e specificità relativamente alla segmentazione automatica delle strutture vascolari, un problema particolarmente complesso su questo tipo di immagini. Le tecniche per l'estrazione di indici clinici a partire dalla morfologia dei vasi sono attualmente in fase di sviluppo.

In prospettiva, strumenti pratici e dalla facile distribuzione come quelli da noi proposti potrebbero facilitare ampi programmi di screening delle retinopatie ipertensiva, diabetica e della prematurità, oltre che il controllo nel tempo del progredire della malattia. La loro utilià sarebbe triplice. In primo luogo, potrebbero essere uno strumento diagnostico di aiuto alla pratica clinica. In secondo luogo, i dettagli quantitativi sulla struttura vascolare della retina potrebbero essere utili nella ricerca medica e per meglio caratterizzare gli sviluppi della retinopatia. Infine, nell'ambito della ricerca farmaceutica, si renderebbe disponibile l'utilizzo di una misura quantitativa e riproducibile dell'evoluzione della retinopatia durante un trattamento farmacologico.

I risultati conseguiti nelle sperimentazioni effettuate e le collaborazioni internazionali in atto con gruppi clinici e di ricerca di rilievo ci rendono fiduciosi riguardo la qualità delle metodologie sviluppate e i potenziali successi del loro impiego, con l'auspicio che futuri miglioramenti possano ampliarne l'utilizzabilità.

Abstract

This thesis deals with the automatic analysis of color fundus images and in particular with the development of image analysis algorithms and the implementation of software applications for the evaluation of hypertensive and diabetic retinopathy in adult subjects, and of retinopathy of prematurity (ROP) in newborns.

Microcirculation is affected, with different time courses, by both hypertension and diabetes, and retinopathy is one of the consequences of such circulation damage. The retinal vessels are very sensitive to changes in microvascular circulation, and it has been demonstrated that single features of hypertensive retinopathy have a strong prognostic value for stroke, carotid stiffness, and coronary disease. Also in premature newborns, whose vasculature may be incomplete or may develop in an anomalous way, the retinopathy signs turn out to be important for the assessment of the gravity of the disease and for preventing possible future visual damages for the patients. Moreover, it must be considered that retinopathy in general is a social burden, with heavy direct and indirect costs: visual loss in fact reduces the capacity of working and carrying on with an independent life.

Although the retina is not the only organ affected by microcirculation damage, its clinical examination has the important advantage of being non invasive, therefore enabling a cost-effective monitoring of the progression of the systemic diseases associated with retinopathy. The early detection of retinopathy at its onset is crucial in order to avoid blindness. This is particularly true in the case of diabetic retinopathy, which at the present state of pharmacology does not recede with treatment.

Unfortunately, the first stages of retinopathy for both adults and infants are almost asymptomatic. It has been demonstrated that a screening program could save most of the population at risk from developing sight-threatening retinopathy. In the Western world, there are not enough resources, in terms of time and available expert ophthalmologists, for carrying out an extensive screening program. Thus, reliable automatic tools for evaluating retinopathies are strongly needed.

This thesis concentrates on the automatic extraction and the analysis of the features of the vascular apparatus: the vessel network identification (veins and arteries) allows the assessment of its main geometrical characteristics (length, direction, caliber, bifurcation, tortuosity, etc.). From these findings, specific indexes of diagnostic relevance are computed, providing the clinicians with information regarding the patient's retinopathy degree, whose significance is crucial for the diagnosis of retinal pathologies.

The instrument used to acquire images of the retina is the fundus camera, a specialized low power microscope with an attached camera designed to photograph the interior surface of the eye. The screening of the retina in adult patients for the diagnosis of retinopathies is commonly done with non-handled, contact fundus cameras, which provide high resolution images with a field of view (FOV) between 30 and 60 degrees. The screening on premature infants for the detection of ROP, on the other

side, is done with customized fundus cameras, presenting some peculiar features. One of them is the Nidek NM200D (Nidek Co., Gamagori, Japan), a handled, non-contact fundus camera that provides high resolution 30 degree images. Another fundus camera commonly used for acquisition on infants is RetCam (Clarity Medical System, Pleasanton, CA, USA), which provides low-resolution images for up to 120 degrees of the ocular fundus. The use of RetCam is generally limited to children without media opacity and for image quality reasons is not normally used in adults.

It is worth noticing that images acquired from adults and infants present different characteristics: this is related to the anatomical variability between the two categories of subjects, but also to the different fundus cameras used for image acquisition and to the diverse acquisition protocols. As a consequence, some algorithms perform very well when analyzing adult retinal images, but turn out to be unsuitable with newborns images. Therefore, we developed algorithms customized for the different kinds of images to analyze, in order to achieve satisfactory performance regardless of the varying attributes related to the acquisition system or to the patient age. In particular, in this thesis we present three systems, designed respectively for the analysis of adult images, infant images acquired with Nidek NM200D and infant images acquired with RetCam.

In order to automatically extract the retinal vasculature in adult images, acquired at different resolutions and fields of view, we propose a novel method. This is based on a multi-directional graph search approach for the detection of vessel centerlines: after a seed-finding procedure, vessel axes are detected by connecting the seeds with minimum cost paths. A fast 1-dimensional matched filter technique is employed for the vessel caliber evaluation: the information of the vessel axis is exploited as prior to determine the filter orientation, and the scale of the kernel filter is tuned with the aim of ensuring the regularity of the segmented vessel borders.

Considering the great variability and the poor quality of infant images acquired with Nidek NM200D, we developed a customized semi-automatic technique to track singular vascular structures and consequently assess their geometrical features. Vessels to be analyzed are selected by manually drawing an approximate centerline inside their boundaries. Starting from this *a priori* information, the vessel edges are detected by means of a filtering technique based on Canny method. Refined axis and calibers along the vessel are then obtained by appropriately linking pairs of points on opposite edges.

For the automatic tracking of vessels in infant images acquired with RetCam, which is particularly challenging because of the low resolution, the poor quality, the very wide field of view and the presence of choroidal structures, we propose an innovative technique. As a first step vessel structures are enhanced by means of different matched filtering techniques, and extracted from the background with a local thresholding followed by morphological operations. The second step consists in a supervised classification of vessel structures based on SVM, in order to discard segments originating from noise/artifacts or from choroidal vessels.

Starting from the described algorithms for image analysis, we developed practical and easy-to-use software systems, aimed at supporting the clinicians with the screening and the diagnosis of retinopathies. In particular we developed a web based application for the analysis of retinal images of adult subjects. The tool is endowed with a user-friendly interface and it allows the user to extract the vascular network and to compute CRAE (Central Retinal Arteriolar Equivalent), CRVE (Central Retinal Venular Equivalent) and AVR (Arteriolar Venular Ratio) according to the Knudtson method. For the analysis of infant retinal images we developed ROPnet, a web tool, customized for the extraction of parameters related to ROP (such as vessel dilation and tortuosity) in premature subjects screened with Nidek NM200D. With ROPnet, vessel analysis can be performed by using a web browser with a client-server setup. Moreover, we are currently developing a similar system for the analysis of the very large field of view images acquired with RetCam.

The system for the identification of retinal vascular structures in adult images was tested on different datasets and the comparison of the proposed automatic vessel segmentation versus a manual ground truth showed high sensitivity and low false detection rate. The proposed software is currently under clinical evaluation at the Department of Ophthalmology and Visual Sciences, University of Wisconsin, USA, the world leading center for clinical trial retinal image analysis, whose Fundus Photograph Reading Center is considering the adoption of the proposed system as standard tool for the extraction of diagnostic features. In addition, a recent collaboration with the Department of Twin Research & Genetic Epidemiology, of the King's College London Division of Genetics and Molecular Medicine, St Thomas' Hospital, UK, has involved the analysis of more than 2000 retinal fundus images with our software for the estimation of clinical indexes in retinal vessels.

The interface and the functionality of ROPnet have been designed in collaboration with the Departments of Ophthalmology of the Children's Hospital and the Scheie Eye Institute of Philadelphia, US, with the aim of meeting the requirements of the clinicians for what concerns both the tool performance and usability. The accuracy of parameters extracted by ROPnet (i.e. vessel width and tortuosity) was confirmed by the high correlation obtained comparing automatic results with a ground truth manually provided by retina experts. Moreover, the web tool was already used for some preliminary clinical study and we are currently investigating the reliability of extracted clinical indexes for the diagnosis and classification of ROP.

The system specifications for the analysis of ROP images acquired with RetCam were discussed directly with Clarity Medical Systems, the manufacturer of the mentioned fundus camera. In this project, we obtained on a preliminary set of images high sensitivity and specificity in the retinal vessel segmentation, which is a particularly difficult task on RetCam infant images. The techniques for the extraction of clinical parameters starting from the vessel morphology are currently under development.

In perspective, practical and easily deployable tools such as those we propose might significantly contribute to the mass-screening and the monitoring of the pro-

gression of hypertensive/diabetic retinopathies and of ROP. Their usefulness will be threefold: first of all, they will provide a diagnostic tool to aid clinical practice; secondly, they will provide quantitative details of the retinal vessel network, thus constituting a useful tool for clinical research; finally, they will endow pharmaceutical research with a quantitative and reproducible assessment of the disease evolution during pharmacological treatment.

The results achieved in the preliminary trials, carried out in cooperation with relevant international clinical research groups, attest the quality of the developed methodologies and bode well for their future clinical adoption.

Chapter 1

Introduction

Hypertensive retinopathy is associated with systemic arterial hypertension; retinal vascular changes can be seen in both chronic and acute stages. It is likely that an increasing number of patients in the future will suffer from hypertension, a pathology ranked as one of the top-10 risk factors for burden of diseases in developed countries by the World Health Organization. In this context, it must be noticed that ophthalmologists occupy a privileged, central position in the detection of the disease, and consequently in the prevention of the visual loss it causes: indeed, a patient with undiagnosed malignant hypertension will probably consult first an ophthalmologist with a complaint of visual loss.

An even more dramatic situation characterizes diabetes-related retinopathy. Diabetes is a growing epidemic in the world, due to population growth, aging, urbanization and increasing prevalence of obesity and physical inactivity: it is estimated that the population with diabetes will grow by 37% by 2030, and today it already counts around 200 million people worldwide. Following the trend of diabetes, diabetic retinopathy assumes an ever increasing importance as a cause of blindness: in the United States it constitutes the first cause of blindness in subjects in working age, with all the economic and social burdens this implies. The timely diagnosis and referral for management of diabetic retinopathy can prevent 98% of visual loss. It is estimated that the underlying cause of blindness in the majority of diabetic patients is not diabetic retinopathy *per se* but the misdiagnosis of diabetic retinopathy.

Another critical retinal disease is retinopathy of prematurity (ROP), which affects premature babies. It can be mild with no visual defects, or it may become aggressive with new blood vessel formation (neovascularization) and progress to retinal detachment and blindness. The incidence of ROP in premature infants is inversely proportional to their birth weight. More than 50% of premature infants weighing less than 1250 g at birth show evidence of ROP, and about 10% of the infants develop a serious stage ROP. In general, as smaller and younger babies are surviving, the incidence of ROP is increasing. Moreover an observational study from United Kingdom outlined that larger and more mature infants seemed to be developing severe retinopathy of prematurity in less-developed nations. This suggests that individual countries need to develop their own screening programs with criteria suited to their local population [1].

Currently, a periodic dilated direct ophthalmoscopic examination appears to be the best approach for a screening (with different frequency and protocols according to the age of the subjects) with near universal coverage of the population at risk, despite the

proved low sensitivity of direct ophthalmoscopy [2], [3], [4]. However, the number of ophthalmologists available is a limiting factor in initiating an ophthalmological screening [5].

With the increasing availability of digital fundus cameras, there is a wide consensus of opinion that an automatic analysis of such digital images might, at least partially, relieve ophthalmologists of the burden of retinopathy screening.

1.1 Aims and Objectives

The aim of the work presented in this thesis is to develop a set of tools for the automatic analysis of retinal images.

The linchpin of this task is the identification of the retinal vessel network, and its description in terms of geometrical properties. The morphology of the vascular structure can be affected by different abnormalities caused by acute pathologies, such as ROP, or by early signs of certain systemic disease, such as diabetes and hypertension. Ocular fundus images can provide important information about these signs and their accurate analysis is necessary to improve clinical diagnosis of diseases. An automatic and quantitative assessment of vessel morphological features, such as dilation and tortuosity, can reveal important information on the mentioned diseases. To this aim, the exact layout of all relevant vessels in the image must be extracted. A significant issue in fundus images is that the contrast between vessels and background is often very poor, especially for capillaries. Digital noise represents another critical aspect. In addition, wider vessels often present a bright reflex at the center (the central reflex), which causes their profile to be indistinguishable from the one belonging to two narrow parallel vessels. In addition, images acquired from preterm infants present highly visible choroidal vessels, because of the very low retinal pigmentation, and in general a lower quality, due to the critical acquisition conditions and to the lack of the patient cooperation.

The image analysis techniques proposed in this thesis consist in a sequence of independent modules aimed at maximizing the automation of the vessel extraction process and of the clinical parameters estimation in different kind of images.

Starting from the extracted morphology of the vessel network, we concentrated on the exploitation of the geometric characterization of the vascular network in order to estimate tortuosity, caliber dilation, CRAE, CRVE, and AVR indexes as parameters of clinical relevance for the diagnosis of retinal pathologies.

In order to provide some tool that may concretely help clinicians to diagnose or quantitatively assess retinopathies gravity, two systems were created. One is a standalone application, organized as a client-server service, for the assessment of generalized arteriolar narrowing in adult images; the second one is a web tool for the estimation of vessel tortuosity and dilation in preterm newborns. The client-server archi-

tecture of the proposed solutions and the user friendliness of the interfaces make the tools available to a wide range of users, even in a telemedicine context.

1.2 Outline

Chapter 2 is introductory and describes retinal imaging. In particular the fundus camera examination, the appearance of the retina in a fundus image, and the main findings of hypertensive and diabetic retinopathy and retinopathy of prematurity will be described.

In Chapter 3, the list of collected retinal image datasets is given, together with a description of their peculiarity. Most of them have been provided by research and clinical groups working in the field of ophthalmology.

In Chapters 4 and 5, a brief review of previously proposed methods will be followed by a description of the vessel tracking system proposed in this thesis for the analysis of images acquired from adult subjects. It is comprehensive of the modules of preprocessing, seed finding, vessel tracing by means of a graph search approach, false vessel detection, caliber extraction and refinement step.

Chapter 6 describes AVRnet, a client-server application developed starting from the algorithms described in the previous chapters. The clinical usability of the system is presented, particularly as regards the estimation of generalized arteriolar narrowing indicators (CRAE, CRVE, and AVR).

In Chapter 7 a brief state of the art about the existing systems to assess retinopathy of prematurity is presented. A new algorithm to analyze small FOV infant retinal images is proposed. It consists in a semi automatic technique to compute the tortuosity and width of vessels. Such clinical indexes can be estimated by using ROPnet, which is the web based system developed starting from the mentioned algorithms. Its architecture, functionality and validation are presented in Chapter 8.

Chapter 9 deals with the tracking of retinal vessels in very large FOV images (up to 130°) acquired from newborns with RetCam. A brief overview of the existing methods is presented, as well as a novel approach, and some preliminary results.

In Chapter 10 conclusion and final discussion are reported.

Chapter 2

Fundus Imaging and its Findings

In this chapter, a brief review will be presented regarding what is seen in an image from a fundus camera examination and all the most relevant lesions to be found in the hypertensive/diabetic retinopathy and in retinopathy of prematurity.

2.1 Fundus Oculi Examination

The first instrument that allowed the direct examination of the retina was the direct ophthalmoscope, which is still used today. It was first described by Helmholtz at the end of the 19th Century, and since then it has not changed much. In its basic form, it is composed by a light source and a set of lenses. The light is projected through the dilated pupil onto the retina, and the lenses focus on so that the observer can look at the retina. Its use is widespread in the clinical practice, but it has been proved to provide poor sensitivity and results highly dependent on the observer's experience.

In the middle of the 20th Century, the first instrument able to acquire photographs of the retina appeared, i.e. a photographic 35mm back connected to an optic system that focuses on the fundus oculi illuminated by a coaxial flash. This fundus camera enables the photography of different portions of the retina with different magnification ranges, from 10x to 60x. Around 1990, the first digital fundus camera appeared. The optic system is no longer connected to a traditional camera, but to a CCD, and the image is sent to a computer for visualization and storage.

2.1.1 Fundus Oculi Appearance

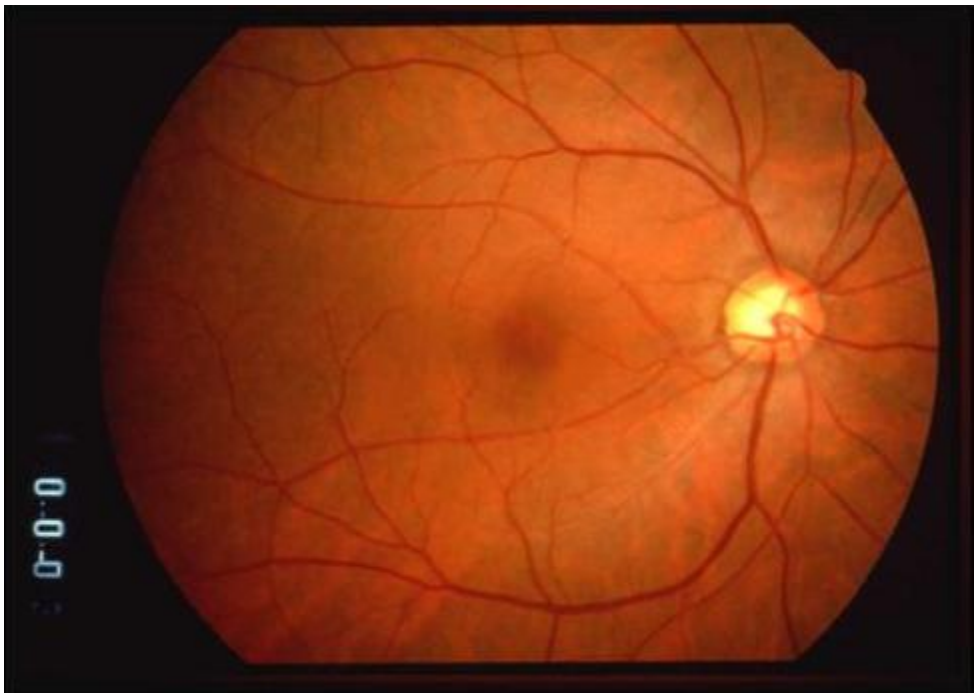

Figure 2.1 An image of a normal fundus oculi. Papilla, fovea and vessel networks are clearly visible.

Using a fundus camera, an image of the fundus oculi is acquired. The visible part consists of the retina with its vascular network, the macula, and the optic nerve head. The choroid is the structure below the retina and is usually obscured by it (at least in adult subjects).

The retina is a multilayered structure, transparent except for the deepest layer, the pigmented epithelium which gives to the retina its reddish colour. More superficial than the pigmented epithelium is the sensorial retina, composed by the photoreceptor cells and by the gangliar cells.

The axons of the gangliar cells run to the papilla, also called optic disc or optic nerve head, which is where the bundle of nervous fibers forms the optic nerve, and leaves the optic bulb. From the center of the optic disc, the ophthalmic artery enters into the optic bulb, and subsequently branches to provide vascularization to most of the retina. From the capillary network the venous vessels originate, which flow into the central retinal vein that exits the ocular bulb through the optic disc.

Topologically, the temporal vessel arcades delimit the posterior pole. At the center of the posterior pole, there is the macula: its center is occupied by a small depression, the fovea, that is the region most densely packed with photoreceptor of the retina and is normally the center of vision. The macula is not fed by retinal vessels, but takes its nutrients from the choroidal vessels below the retina.

Choroidal vessels are not usually visible in an image taken with a fundus camera, but if the pigmented epithelium is very lightly pigmented, or in case of pathological

depigmentation, the retina becomes almost transparent and the choroid becomes visible.

2.2 Main Vascular Abnormalities

2.2.1 Tortuosity

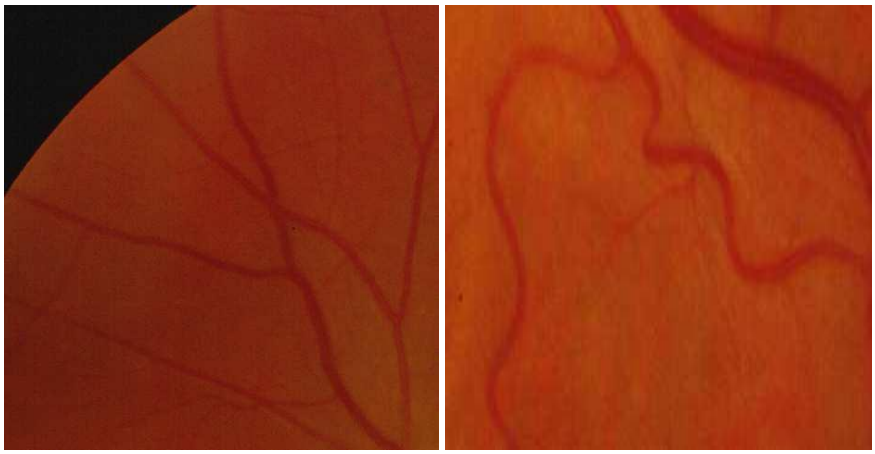

(a) (b)

Figure 2.2 Normal vessel course (a) and tortuous vessels (b).

In presence of high blood pressure, vessels may increase in length and vessel walls may thicken. As a result, they become increasingly tortuous. This is at first seen in arteries, while the veins are affected only in more severe stages of retinopathy.

2.2.2 Generalized Arteriolar Narrowing

The earliest fundus change due to hypertension is the thinning of the retinal arterioles. The narrowing of the arterioles is usually proportional to the degree of elevation of blood pressure. However, retinal arteriolar narrowing is imprecisely quantified from a clinical ophthalmoscopic examination, since the examiner should estimate the normal vessel width prior to the narrowing, in order to be capable of evaluating the severity of the latter.

2.2.3 Focal Arteriolar Narrowing

Figure 2.3 A definite focal narrowing.

In severe hypertension states, irregularities in the caliber of blood vessels may appear. In arterioles, these are due to localized spasm and contractions of the wall. They appear as a focal thinning of the blood column: the narrowing may increase until the vessels become thread-like.

2.2.4 Bifurcation Abnormalities

Arterial diameters and topography at branch points are believed to conform to design principles that optimize circulatory efficiency and maintain constant shear stress across the network [6]. It has been suggested that arterial diameters at a bifurcation should conform to a power relationship, and arterial branches in various circulation have been shown to obey to this design. It has been shown that bifurcation angles are reduced with increasing hypertension, probably because the atheroma fibrosis of the central artery displaces by contraction the arteries toward the disk. Although the mechanisms of bifurcation changes are not clear, both the branching angles and the value of the junction exponent seem to deviate from its optimal values with age [7].

2.2.5 Crossing Abnormalities

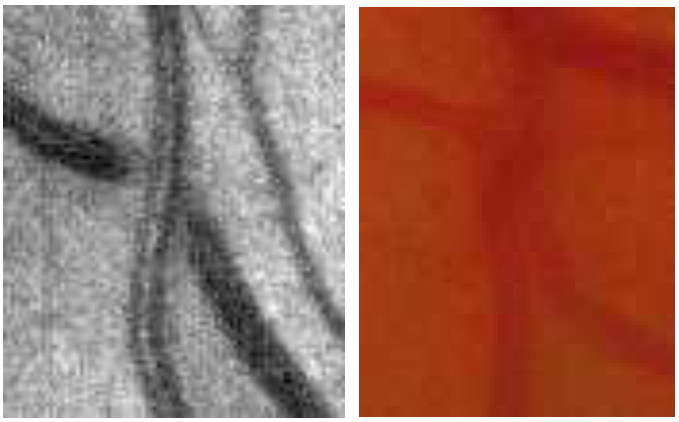

(a) (b)

Figure 2.4 Gunn's sign - vein compression (a) and Salus' sign – vein deflection (b).

The abnormal changes in arterio-venous crossings result from the thickening of the wall of the arterioles due to hypertension and sclerosis, and associated changes in the veins at the crossings. The first appearance of crossing abnormalities is the compression of the vein by the artery, which may vary in severity from a slight indentation to the complete interruption of the vein where the artery crosses. When the sclerosis in the artery extends to the adventitia of the vein, the blood column in the vein will be partially obscured and appear tapered on each side of the crossing.

The constriction and compression of the veins may impede the blood return, so that the veins become distended for some distance peripheral to the crossing: this is the so-called 'Gunn's sign'.

Arterial sclerosis may cause the detection of the vein from its normal course at the point where the artery crosses. The vein may detect both vertically (dipping under the artery or humping over it), or laterally. In the latter case, instead of crossing the artery obliquely, the vein does so at right angles and appears S-shaped at the bend, – a characteristic which has been referred to as the 'Salus' sign'.

2.3 Major Non-Vascular Findings

2.3.1 Microaneurysms and Red Dots

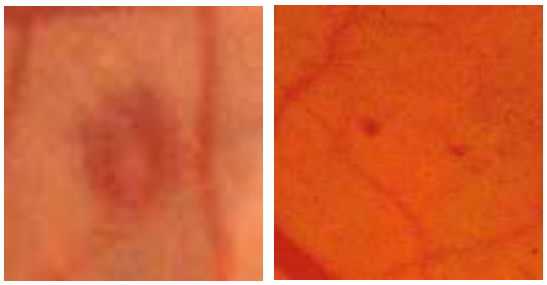

(a) (b)

Figure 2.5 Large microaneurysm with central reflex (a) and microaneurysm (b).

Retinal microaneurysms constitute the most characteristic lesions caused by diabetic retinopathy, but are present also in other pathologies that affect the microvessels. Micoraneurysms are small dilations of capillary walls. It is not clear whether retinal microaneurysms are due to vessel wall damage or to the beginning of a neovascularization. However, the visual consequence is the appearance of small saccular structures, of approximate dimension between 10 μm and 100 μm , which in the retinal fluorescein angiography appear as bright hyperfluorescent spots, whereas in colour fundus images appear as round, red spots. They are indistinguishable from small hemorrhages of the same dimension, since they both are small round regions, with a dark red colour. Therefore, both microaneurysms and hemorrhages smaller than the major vein caliber at the optic disc margin, are considered red dots, and evaluated as microaneurysms [8]. On the contrary, any red spot greater than that is considered an hemorrhage, unless features as round shape, smooth margins and a central light reflex suggest that it is probably a microaneurysm.

2.3.2 Hemorrhages

Retinal hemorrhages are blood deposits on the retina. Hemorrhages disappear as the blood is reabsorbed with time.

They are due to the breaking of a vessel wall or of a microaneurysm, and the increase in their presence is a clear sign of diffuse retinal damage. They have very different shapes, going from the round red spot with sharp margins, to the blot hemorrhage. As the blood is reabsorbed, hemorrhage margins fade and the characteristic red colour turns to a faint grayish-red before disappearing completely.

2.3.3 Hard Exudates

(a) (b) (c)

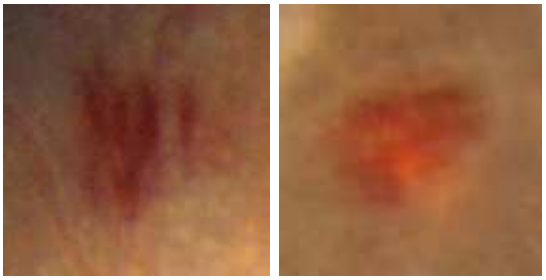

(d) (e)

Figure 2.6 Small hemorrhage (a), barely visible hemorrhage (b), flame hemorrhage (d), large hemorrhage (d), and bright hemorrhage (e).

Hard exudates are small lipidic and proteinic deposits, which appear as white or yellowish-white areas with sharp margins. They may be arranged as individual dots, confluent patches or in partial or complete rings surrounding microaneurysms or zones of retinal edema. In the more severe cases of hypertensive retinopathy, they appear as a confluent ring around the macula (the macular star).

2.3.4 Cotton Wool Spots

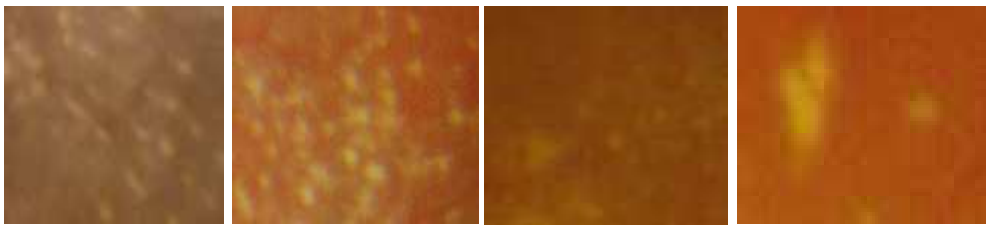

(a) (b) (c) (d)

Figure 2.7 Different hard exudates.

(a) (b) (c)

Figure 2.8 Cotton wool spots.

Cotton wool spots are the consequence of retinal ischemic events, due to precapillary arterioles stenosis. This causes a swelling of the nerve fiber layer, with local deposit of cytoplasmatic material. They are round or oval in shape, white, pale yellow-white or grayish-white, with soft and feathery edges, which give their characteristic aspect and their name. They usually appear along the major vessel arcades, parallel to the nerve fibers, and are sometimes accompanied by the presence of microaneurysms.

2.3.5 Drusen

Drusen are deposits associated with thinning or hypopigmentation of the retinal pigment epithelium. They appear as deep, yellowish-white dots. A stereoscopic view would help to distinguish drusen from hard exudates, since drusen appear very deep, while hard exudates are slightly more superficial. In the protocol used in this thesis the photographs are mono, therefore it is not easy to establish the difference between hard exudates and drusen. Several other features help to distinguish drusen from hard exudates. Drusen are usually scattered diffusely or scattered near the center of the macula. They are usually round in shape, while hard exudates are usually irregular in shape. Finally, drusen often have a faint border of pigment.

2.4 Hypertensive Retinopathy Grading

The classification of hypertensive changes in the retina in a severity scale was first proposed by Keith [9], in what is now currently known as the Keith-Wegener-Barker grading system. It was subsequently modified by Scheie [10] so as to better separate hypertensive from atherosclerotic abnormalities. In Table 2.1 the two classifications for hypertensive retinopathy are shown. It is worth noting that recent literature challenges the prognostic significance of these classifications. The poor correlation with the severity of hypertension variation at the onset and progression of the clinical signs has suggested the use of a two-grade classification of retinopathies: non-

malignant and malignant [11]. This is further confirmed by the fact that the density of perifoveal capillaries and the capillary blood tow velocity analyzed with an angiographic examination correlate more with a two-grade rather than with the classical four-grade classification system. Nevertheless, the Keith-Wegener-Barker is still the *de facto* standard in the evaluation of hypertensive retinopathy.

Keith-Wegener-Baker	
Grade	Features
I	Mild generalized retinal arteriolar narrowing. Increased arterial tortuosity
II	Definite focal narrowing and arterio-venous crossing abnormalities
III	The above and retinal hemorrhages, exudates and cotton wool spots
IV	Severe grade III plus papillar oedema

Scheie	
Grade	Features
1	Barely detectable arterial narrowing
2	Obvious arterial narrowing with focal irregularities and light reflex changes
3	The above plus copper wiring, and retinal hemorrhages and exudates
4	Grade 3 plus silver wire and papillar oedema

Table 2.1 Classification of hypertensive retinopathy as proposed in [9] and [10].

2.5 Diabetic Retinopathy

Two landmark clinical trials set the standard in grading diabetic retinopathy: the Diabetic Retinopathy Study (DRS) [12] and the Early Treatment Diabetic Retinopathy Study (ETDRS) [13]. The ETDRS severity scale was based on the Airlie House classification of diabetic retinopathy and is used to grade fundus photographs. It has been widely applied in research settings and publications, and it has shown satisfactory reproducibility and validity. Although it is recognized as the gold standard for grading the severity of diabetic retinopathy in clinical trials, its use in everyday clinical practice has not proven easy or practical. The first reason for this is that the photographic grading system has 90 levels, many more than what is necessary for clinical care. Given the number of levels to consider, the detailed specific definitions of the levels, and the necessary comparison with standard photographs, it is not surprising that the ETDRS grading procedure is difficult to remember and apply in a clinical setting.

Recently, simplified severity scales have been developed in an effort to improve both the screening of patients with diabetes and communication among caregivers. Yet, to overcome this proliferation of *ad hoc* grading scales, it has been proposed in

[14] a Diabetic Retinopathy Disease Severity Scale, in which separate scales were proposed to grade diabetic retinopathy (4 levels) and macular edema (5 levels). The two scales are summarized in Table 2.2 and Table 2.3.

Disease Severity Level proposed in [14]	Disease Severity Level proposed in [14]
No Apparent Retinopathy	No abnormalities
Mild non-proliferative diabetic retinopathy	Microaneurysms only
Moderate non proliferative diabetic retinopathy	More than just microaneurysm but less than severe non proliferative diabetic retinopathy
Severe non proliferative diabetic retinopathy	Any of the following: more than 20 intraretinal hemorrhages in each of 4 quadrants; definite venous beading in 2 or more quadrants; prominent intraretinal microvascular abnormalities in one or more quadrant and no signs of proliferative diabetic retinopathy
Proliferative diabetic retinopathy	One or more of the following: neo vascularization, vitreous or preretinal hemorrhage

Table 2.2 Classification of diabetic retinopathy as proposed in [14].

Disease Severity Level proposed in [14]	Findings Observable on Dilated Ophthalmoscopy
Diabetic macular oedema apparently absent	No apparent retinal thickening or hard exudates in posterior pole
Mild diabetic macular oedema	Some retinal thickening or hard exudates in the posterior pole but distant from the center of the macula
Moderate diabetic macular oedema	Retinal thickening or hard exudates approaching the center of the macula but not involving the center
Severe diabetic macular oedema	Retinal thickening or hard exudates involving the center of the macula

Table 2.3 Classification of diabetic macular oedema proposed in [14]. Hard exudates are sign of current or previous macular oedema. Diabetic macular oedema is defined as retinal thickening and requires a three-dimensional assessment.

2.6 Retinopathy of Prematurity

Retinopathy of prematurity (ROP), is an eye disease that affects prematurely born babies. It is thought to be caused by disorganized growth of retinal blood vessels which may result in scarring and retinal detachment. ROP can be mild and may resolve spontaneously, but it may lead to blindness in serious cases.

2.6.1 Definition

Retinopathy of prematurity is characterized by abnormal retinal vascularization, which can affect premature newborns. In these babies the growth of retinal blood vessels does not reach the peripheral area of the retina. In fact, usually, blood vessels begin their development, starting from the optic disc, during the 15^{th} gestation week, continuing their growth and ramification until the 9^{th} month of pregnancy.

Several studies showed that retinal blood vessels grow starting from cells called spindle cells which develop from the optic nerve through the ora serrata. Spindle cells reach the ora serrata at 29^{th} week of gestation, whereas the blood vessels develop later and they reach the retinal periphery only during the last weeks of gestation. Consequently, in premature newborns, the blood vessels accretion does not have the time to reach all retinal areas and this leads to several kind of complications. Beyond that, a relevant condition that allows the migration and maturation process of the spindle cells is the hypoxic environment in the uterus (PaO2=25 mmHg). This hypoxic condition strongly changes after birth and the PaO2 reaches values of 70mmHg or more, negatively influencing the retinal blood vessels development. In fact the hyperoxigenated blood leads to formation of dangerous free radicals that decelerate the spindle cells maturation process.

Retinopathy of prematurity is a complex disease caused by several factors and circumstances so the exact pathogenesis is not completely clear yet.

2.6.2 Causes and Risk Factors

Low birth weight (less than 1500 grams) and low gestation age (less than 32 weeks) are considered the two most important causes related to the development of ROP. Generally, the more premature is the baby, the more severe is the sickness.

Retinal blood vessels begin to develop three months after conception and complete their development at the time of normal birth. If an infant is born very prematurely, eye development can be disrupted. The vessels may stop growing or grow abnormally from the retina into the clear gel that fills the back of the eye. The vessels are fragile

and can leak, causing bleeding in the eye. Scar tissue may develop and in severe cases this can result in vision loss. In the past, routine use of excess oxygen to treat premature babies stimulated abnormal vessel growth. Currently, oxygen can be easily and accurately monitored, so this problem is rare.

Today, the risk of developing ROP depends on the degree of prematurity. Generally, the smaller and sicker the premature babies, the higher the risk.

Typically all babies younger than 30 weeks gestation or weighing fewer than 1500 grams at birth are screened. Certain high-risk babies who are born after 30 weeks should also be screened.

In addition to prematurity and low weight, other risks factors may include:

- Brief stop in breathing (apnea)
- Heart disease
- High carbon dioxide (CO2) in the blood
- Infection
- Low blood acidity (pH)
- Low blood oxygen
- Respiratory distress
- Slow heart rate (bradycardia)
- Transfusions

Luckily, the rate of ROP in moderately premature infants has decreased dramatically with better care in the neonatal intensive care unit. However, this has led to high rates of survival of very premature infants who would have had little chance of survival in the past. Since these very premature infants are at the highest risk of developing ROP, the condition might actually become more common again.

2.6.3 Classification of ROP

The international ROP classification (ICROP), used to code correctly epidemiological data, avails of a specific pattern to classify lesions. It was firstly realized in 1984 and then revised in 1987 and 2005 and it has been very useful in order to collect more information about this disease and in order to improve the knowledge of its development. ICROP classification is based on several essential observations aimed at describing the retinopathy, as the location, the extension, the stage, the blood vessels conformation [15].

2.6.3.1 Localization

Considering the localization, the ocular fundus has been subdivided in three concentric zones centered in the optic disc:

- Zone 1 is the posterior zone of the retina, defined as the circle with a radius extending from the optic nerve to double the distance to the macula. Disease in zone 1 is more severe compared with disease limited to zones 2 or 3.
- Zone 2 is an annulus with the inner border defined by zone 1 and the outer border defined by the radius that is the distance from the optic nerve to the nasal ora serrata.
- Zone 3 is the residual temporal crescent of the retina.

2.6.3.2 Extension

The extension is evaluated basing on the horary localization as if the top of the eye was 12 on the face of a clock, that is basing on the "number of hours" characterized by pathology signs. As the observer looks at each eye, the 3-o'clock position is nasal in the right eye and temporal in the left eye, and 9-o'clock position is temporal in the right eye and nasal in the left eye.

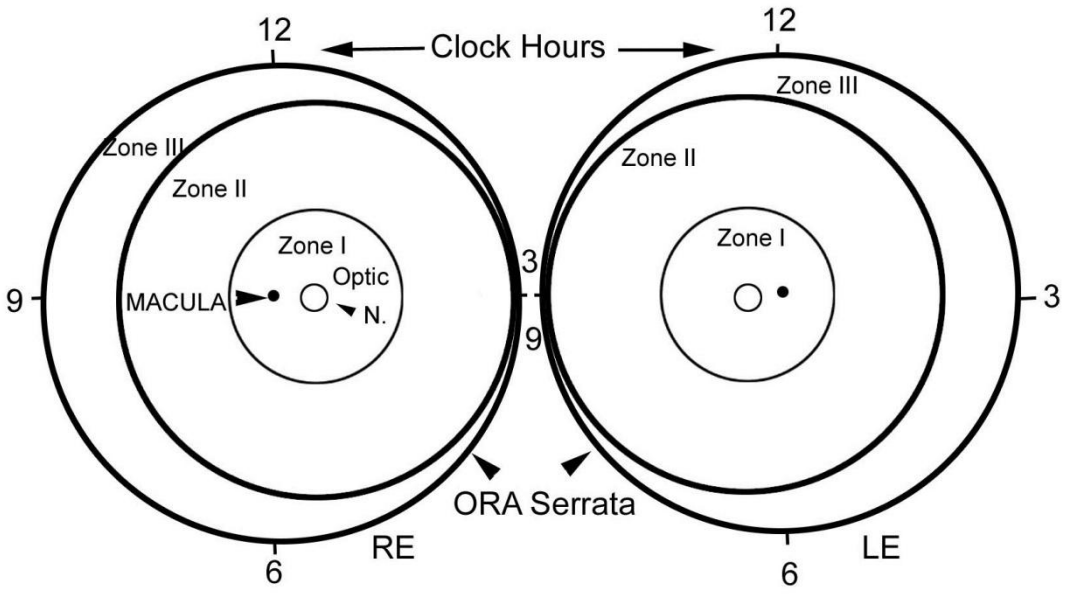

Figure 2.9 Localization and extension of ROP.

2.6.3.3 Pathology Stages

There are five stages that are usually adopted to describe the abnormal vascular response at the junction of the vascularized and avascular retina.

ROP stage 1: examining the premature newborns ocular fundus, the image shows a peripheral area of the retina lacking of blood vessels, really well defined and bordered by an evident demarcation line from the rest of the retina, which is well vascularized. This line is a thin but definite structure that separates the avascular from the vascularized retina.

ROP stage 2: the strong demarcation line that divides the two areas (one vascularized, the other without blood vessels) can disappear during the following weeks, and the blood vessels can develop in a normal way reaching also the peripheral area of the retina. Nevertheless the pathology can also advance achieving the stage 2, in which the demarcation line assumes the morphology of a ridge. The ridge is the hallmark of stage 2 ROP. It arises in the region of the demarcation line but it has measurable height and width and it extends above the plane of the retina. The ridge may change from white to pink and vessels may leave the plane of retina posterior to the ridge to enter it.

ROP stage 3: from ROP stage 2 the pathology can regress spontaneously but it also may develop into an extraretinal blood vessels proliferation; in stage 3, extraretinal fibrovascular proliferation or neovascularization extends from the ridge into the vitreous. This extraretinal proliferating tissue is continuous with the posterior aspect of the ridge, causing a ragged appearance as the proliferation becomes more extensive. The severity of a stage 3 lesion can be subdivided into mild, moderate, or severe depending on the extent of extraretinal fibrovascular tissue infiltrating the vitreous.

ROP stage 3 plus: if the development of the disease is very fast and the posterior vessels are characterized by tortuosity and dilation associated to retinal hemorrhages, the pathology is classified as stage 3 plus which represents the point of no return for this kind of disease, and the moment in which it is indispensable to consider the possibility of a surgery intervention. The ROP in stage 3 that requires treatment is usually called threshold disease.

ROP stage 4: it is divided into extrafoveal (stage 4A) and foveal (stage 4B) partial retinal detachments. Stage 4 retinal detachments are generally concave and most are circumferentially oriented. The extent of retinal detachments depends on the number of clock hours of fibrovascular traction and on their degree of contraction.

ROP stage 5: it is characterized by a total retinal detachment. Retinal detachments are generally tractional and may occasionally be exudative.

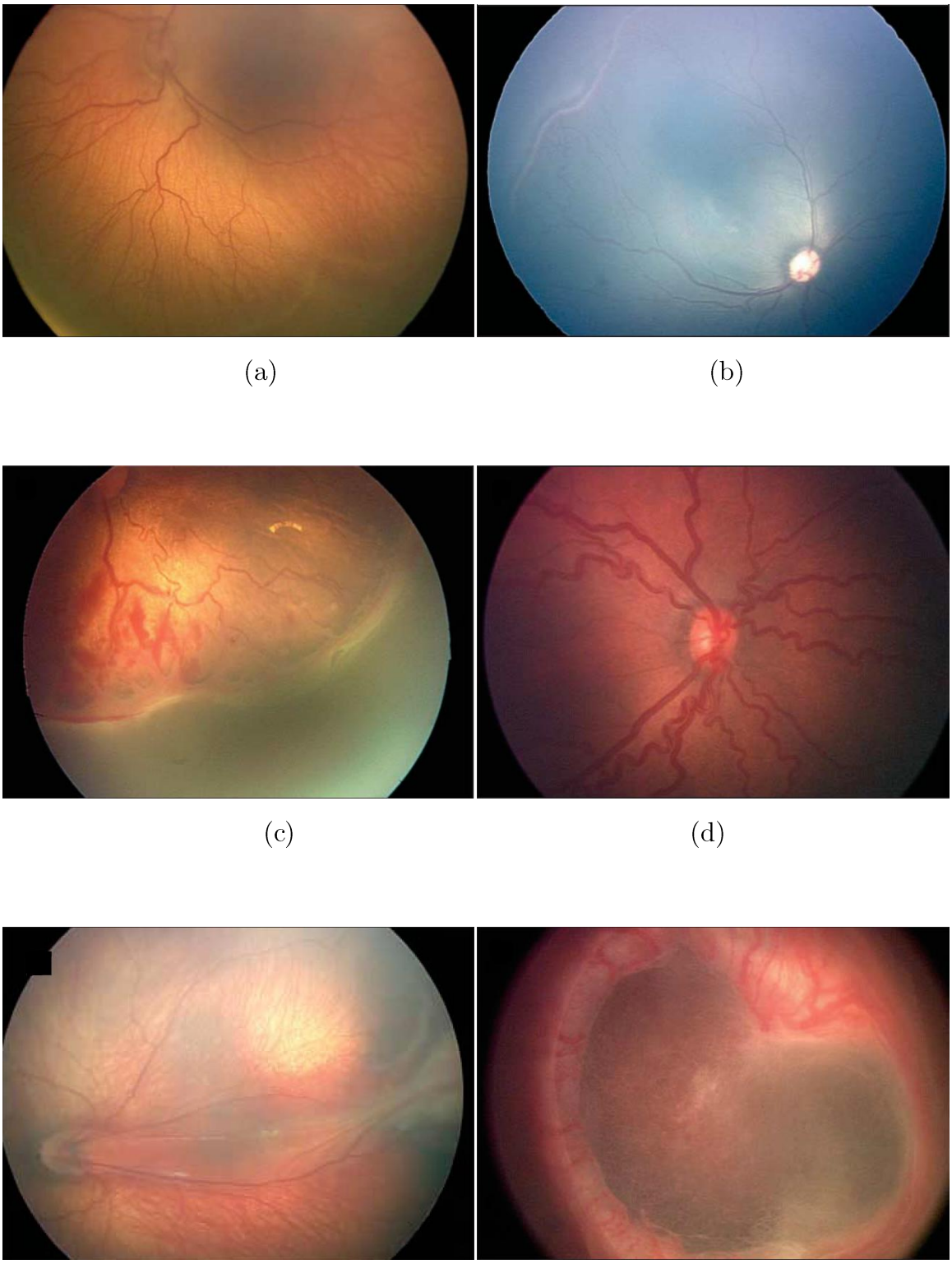

(a) (b)

(c) (d)

(e) (f)

Figure 2.10 Image examples for different ROP stages. (a) stage1, (b) stage2, (c) stage 3, (d) stage 3 – plus, (e) stage 4, (f) stage 5. (Courtesy of [15]).

2.6.3.4 Plus Disease

Along with the changes described earlier at the leading edge of the abnormally developing retinal vasculature, additional signs indicating the severity of active ROP may occur. These include increased venous dilation and arteriolar tortuosity of the posterior retinal vessels and may later increase in severity to include iris vascular engorgement, poor papillary dilatation and vitreous haze. This important constellation of signs in the original classification was referred to as plus disease. Subsequent multicentered clinical trials have used a "standard" photograph to define the minimum amount of vascular dilatation and tortuosity required to make the diagnosis of plus disease. This definition has been further refined in the later clinical trials, in which the diagnosis of plus disease can be made if sufficient vascular dilation and tortuosity are present in at least 2 quadrants of the eye. Plus disease can be present at any stage.

2.6.3.5 Pre-Plus Disease

Pre-plus disease is defined as the presence of vascular abnormalities of the posterior pole that are insufficient for the diagnosis of plus disease but that demonstrate more arterial tortuosity and more venous dilation than normal. Over time, the vessel abnormalities of pre-plus may progress to plus disease as the vessels dilate and become more tortuous.

2.6.3.6 Aggressive Posterior ROP

An uncommon, rapidly progressing, severe form of ROP is designated as AP-ROP. If untreated, it usually progresses to stage 5 ROP. The characteristic features of this type of ROP are its posterior location, prominence of plus disease, and the ill-defined nature of the retinopathy. Aggressive posterior ROP is observed most commonly in zone 1, but it may also occur in posterior zone 2. Early in the development of AP-ROP, the posterior pole vessels show increased dilation and tortuosity in all 4 quadrants and it is often difficult to distinguish between arterioles and venules because of the significant dilation and tortuosity of both vessel types.

Chapter 3

Collected Datasets

This chapter provides a description of the features and the provenience of the datasets used to train and test the developed software for the automatic analysis of the retinal fundus.

We created a database of images combining a number of datasets, which have been kindly shared in the Internet by researchers in the field of ophthalmology, with sets of images we have gathered thanks to the collaboration with national and international clinical centers.

3.1 The DRIVE Dataset

The photographs for the DRIVE database [16], [17] were obtained from a diabetic retinopathy screening program carried out in The Netherlands. The images were acquired using a Canon CR5 non-mydriatic 3CCD camera with a 45° field of view (FOV). Each image was captured using 8 bits per color plane at 768 by 584 pixels. The FOV of each image is circular with a diameter of approximately 540 pixels.

The set of 40 images has been divided into a training and a testing set, both containing 20 images. The authors made available a single manual segmentation of the vasculature for the training images, and two manual segmentations for the test case. As far as the two testing manual segmentations are concerned, the authors suggest using one as gold standard, while the other can be used to compare computer-generated segmentations with those of an independent human observer. All human observers that manually segmented the vasculature were instructed and trained by an experienced ophthalmologist. They were asked to mark all pixels of which they were at least 70% certain that they were vessel.

Thanks to the DRIVE database made publicly available to download at http://www.isi.uu.nl/Research/Databases/DRIVE/, we could evaluate the performances of our vessel tracking algorithm for adult images.

3.2 The STARE Dataset

The STARE dataset [18] consists of twenty retinal fundus slides. The slides were captured by a TopCon TVR-50 fundus camera at 35° field of view. Each slide was digitalized to produce a 605x700 pixel image, 24-bits per pixel (standard RGB). Ten images are from patients with no pathology (normal). Ten images contain pathologies that obscure or confuse the blood vessel appearance in varying portions of the images (abnormal). The authors explained that this selection was made for three reasons. First, most of the referenced methods had only been demonstrated upon normal vessel appearances, which are easy to discern. Second, some level of success with non-normal vessel appearances must be established to recommend clinical usage. Third, they desired to evaluate the performance differences (if any) of the algorithms on normal and abnormal case.

Two human observers carefully labeled by hand each of these twenty images, to produce ground truth vessel segmentation and a second observer's reference. We used the STARE dataset to evaluate the performance of the vessel tracking algorithm for adult images proposed in this thesis. The STARE dataset can be downloaded from the web page http://www.ces.clemson.edu/~ahoover/stare/.

3.3 University of Wisconsin Dataset

Twenty 30° color retinal images acquired during the DCCT study [19] and eighteen acquired during the ETDRS study [20] were made available by the Department of Ophthalmology and Visual Sciences, University of Wisconsin, USA (from now on, called the "UoW dataset"). The images were saved in digital format, with a resolution of 3.7 μm/pixel, resulting in 2346x2652 pixel images for the DCCT dataset and 2983x2344 pixel images for the ETDRS dataset.

Unlike the two previously mentioned datasets, this one is not accompanied by a manual segmentation of the retinal structure. For each image, instead, expert clinicians have provided the AVR parameters as far as the ETDRS set is concerned, and the AVR, CRAE, and CRVE parameters as far as the DCCT set is concerned.

We used the data kindly provided by the University of Wisconsin to assess the capability of our software, paired with the one proposed in [21], to accurately and reproducibly describe the above mentioned clinical parameters, by means of a correlation comparison with the measures obtained by trained and proved personnel (see Chapter 6).

3.4 King's College Dataset

Twenty nine color fundus images were acquired with a commercial fundus camera in normal healthy subjects, according to the NM-1 standard [22]: 50° field focused centrally between the temporal margin of the optic disc and the center of the macula. The image size is 1664x1664 pixels. Images were kindly provided by the Department of Twin Research & Genetic Epidemiology, of the King's College, London, Division of Genetics and Molecular Medicine, St Thomas' Hospital, UK. This dataset is not accompanied by any manual ground truth. It was used to assess the inter- and intra-grader analysis agreement for the software system proposed for the AVR, CRAE, and CRVE parameters quantification in adult images (see Chapter 6).

3.5 DB60 Homemade Dataset

The images used to build this dataset were taken at the Ophthalmology Clinics of the Universities of Padova, Udine and Trieste by experienced technicians.

The films were subsequently sent to the Department of Information Engineering of the University of Padova, where they were digitized at 1360 dpi, 24 bits per pixel, using a Canon scanner. 1444 retinal images of various quality and retinopathy level were digitalized, yielding images of the approximate size of 1400x1200 pixels. An expert ophthalmologist chose 60 images creating what will be called the DB60.

3.5.1 Image Collection

To provide a ground truth evaluation of the images chosen in the DB60, a standard report form has been set up, and it is shown in Figure 3.1 and Figure 3.2. The first page of the report contains all the information relevant in the evaluation of the retinopathy. The second page requires the ophthalmologist to sketch on the scheme the approximate position of individual lesions (crossing abnormalities, focal arteriolar narrowing, non-vascular lesions), on the scheme. The standard clinical evaluation for hypertensive retinopathy is the Keith- Wegener-Barker grading scheme [9], or that proposed by Scheie [10]. The single abnormality is evaluated usually as none, mild, moderate or severe. Such qualitative evaluations provide a very rough assessment of the pathology and of its constituting damages. In order to overcome this limitation, the ophthalmologist was required to fill in for every abnormality a grading in a percent scale, with percent intervals corresponding roughly to the none-mild moderate-severe grading.

The images in the DB60 were evaluated by two experienced ophthalmologists of the Ophthalmology Department of the University of Padova. In the end, a manual segmentation of the vessel network was provided by 3 technicians, opportunely trained by the same ophthalmologists who validated their final work.

The DB60 dataset allowed the evaluation of the performance of the vessel tracking algorithm for adult images proposed in the following chapters of this thesis.

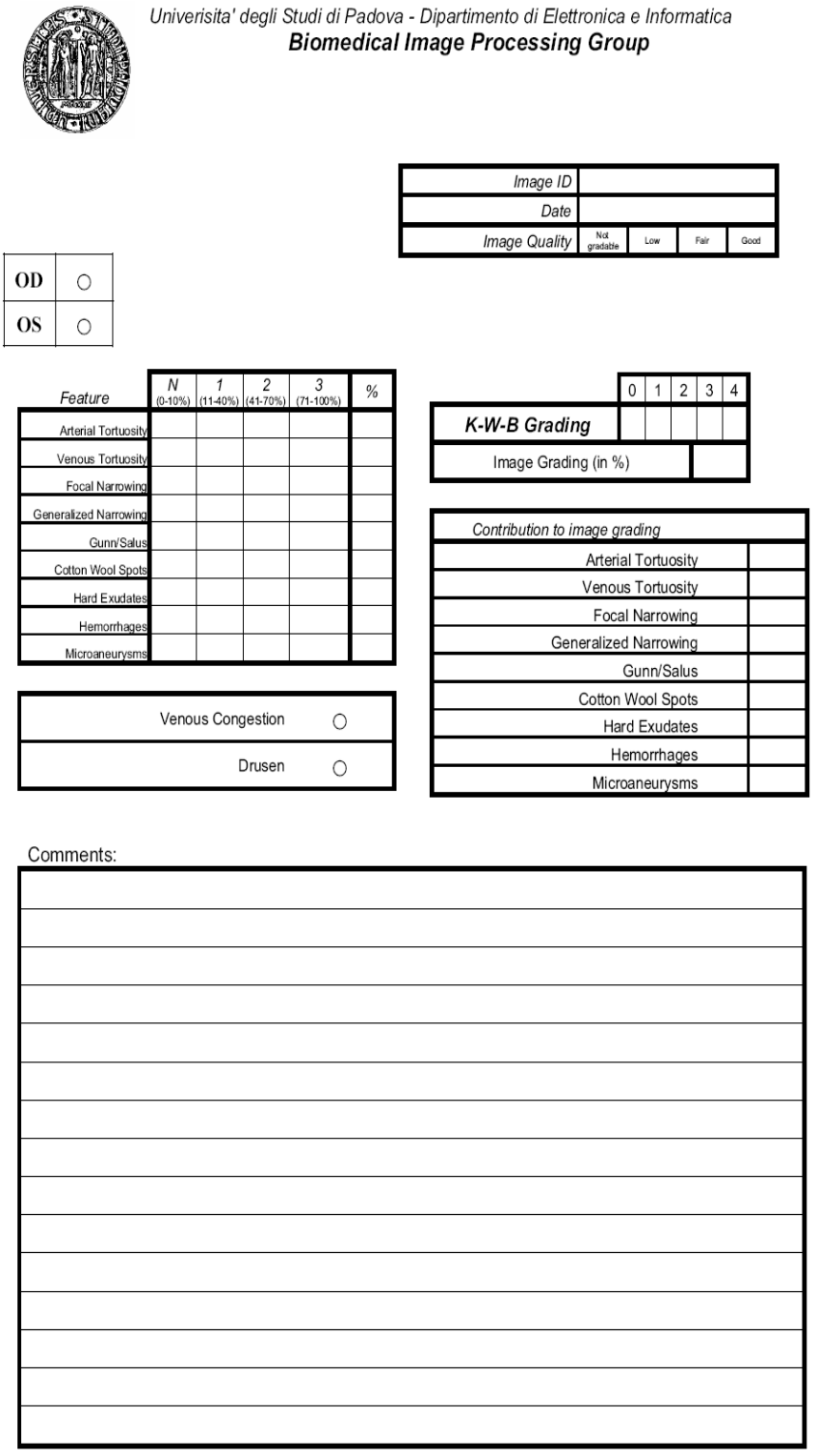

Figure 3.1 Standard report form (front page).

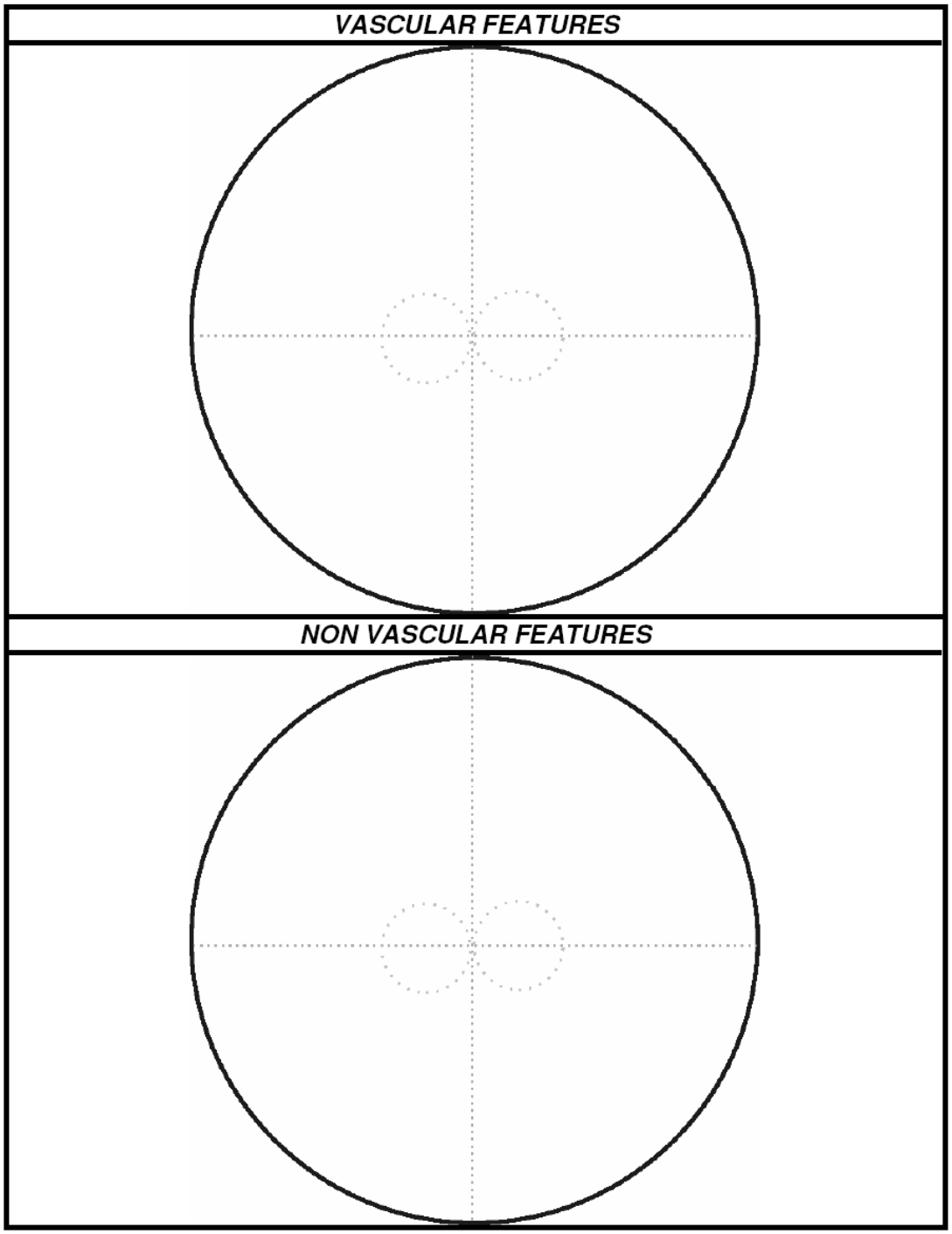

Figure 3.2 Standard report form (rear page).

3.6 Scheie Eye ROP Width Dataset

This dataset includes eighteen vessels extracted from five images acquired at the Departments of Ophthalmology of the Scheie Eye Institute of Philadelphia, with the noncontact Nidek NM200D camera, in the neonatal intensive care unit. The images

were acquired with a 30° field of view optic and saved in digital format with size of 1280x960 pixels. The average gestational age of the infants and average birth weight were 26 weeks and 816 grams, respectively. Average post menstrual age (PMA) at the time of fundus photography was 33 weeks. The vessels composing this dataset were chosen in order to span a wide range of average widths. A manual segmentation of the vessel segments was provided by a retinal expert. This dataset allowed the evaluation of the performance of the vessel tracking algorithm for infant images acquired with Nidek NM200D, proposed Chapter 7 and Chapter 8.

3.7 CHOP ROP Tortuosity Dataset

This dataset includes twenty vessels, extracted from ten images, acquired at the Departments of Ophthalmology of the Children's Hospital of Philadelphia with the noncontact Nidek NM200D camera in the neonatal intensive care unit. The images were acquired with a 30° field of view optic and saved in digital format with size of 1280x960 pixels. The average gestational age of the infants and average birth weight were 26 weeks and 816 grams, respectively. Average post menstrual age (PMA) at the time of fundus photography was 33 weeks. The vessels composing this dataset were chosen in order to span a wide range of tortuosities. A manual ranking was provided by an expert ophthalmologist who ordered the 20 vessels by increasing perceived tortuosity. This dataset allowed the evaluation of the performance of the vessel tracking algorithm for infant images acquired with Nidek NM200D, proposed in the following chapters of this thesis.

3.8 Clarity ROP Dataset

The images used to build this dataset were taken from infants at the Clarity Medical Systems, California, by experienced technicians. For each acquisition a video was registered with the RetCam fundus camera and images were obtained by extracting single frames presenting good quality. RetCam provides images at 120° field of view with size of 640x480 pixels. Fifty one retinal images of various quality and ROP stage were stored and a retina expert created this dataset by choosing twenty images among the fifty one set. A manual segmentation of the vessel network was provided by an expert and used to evaluate the performance of the vessel extraction algorithm for infant images acquired with RetCam, proposed in Chapter 9.

Chapter 4

Vessel Tracking for Adult Images

Most retinopathies, deriving e.g. from hypertension or diabetes, could be early diagnosed and treated if an accurate and objective analysis of symptoms at their initial onset could be performed. The analysis should be accurate enough to detect minor pathological signs, and objective enough to be able to compare results with accepted clinical standards and with results obtained from the same patient at different times. The latter requirement is of paramount importance when assessing the effect of established therapeutic treatments and even more central when evaluating in a quantitative way the efficacy of new drugs during their development.

Most of the early symptoms indicating the onset of retinopathies are related to morphological features of the retinal vascular tree [7]. When no major signs of retinal degeneration are present (such as cotton wool spots, hemorrhages, exudates), the clinical diagnostic procedure for retinopathy always starts with a careful evaluation of the main features of the network of retinal vessels, obtained from fundus camera images. The clinically most relevant signs taken into account by expert ophthalmologists are in general vessel tortuosity, vessel caliber and its distribution among different vessels, presence of vessel caliber irregularities along the same vessel, and the so-called Gunn and Salus signs, i.e., local caliber reduction or local deviation of vessel direction at the crossings between artery and vein [23].

In order to detect and quantitatively describe these diagnostic signs, the information, which has to be extracted from the vascular network, regards the layout and the dimension of all the relevant vessels contained in the image. This task is relatively easy for an expert ophthalmologist if performed at a qualitative level, but rather cumbersome, highly subjective and error-prone if a set of measurements is required [24], [25]. For this reason, a number of research projects have been carried out to develop automatic computerized systems for the extraction of retinal vascular structure.

Here, a new system for the automatic extraction of the vascular structure in retinal images acquired in adult subjects is proposed. Such system is based on a sparse tracking technique via a multi-directional graph search approach. We consider the image as a weighted un-oriented graph with edges connecting adjacent pixels and assume that vessels are minimum cost paths connecting remote nodes.

The first step consists of a preprocessing of the image. After the normalization of contrast and luminosity provided by the method proposed in [26], a simple morphological operation is employed to get rid of arterial central reflexes. Then, a seed-

finding algorithm based on fast 1-dimensional multi-scale matched filters is run over a regular grid. Simultaneous best-first search graph explorations start from each seed: when two search frontiers meet, the computed shortest path is recorded and exploited for a new search starting from it. New paths are found by iterating the procedure, until the entire vessel network is reconstructed. Then, in order to cover the unexplored region with low-contrast vessels and overcome the intrinsic inability of the algorithm to find circular paths, a custom fixing procedure is run. Lastly, a false vessel detection procedure evaluates, for each vessel, a "vesselness" value which is compared with a hard threshold.

4.1 Brief Overview of Available Methods

Automatic techniques for vessel identification have been proposed for general angiography, e.g. [27], [28], [29], and also for more specialized areas such as coronary angiography, e.g. [24], [25], [30], [31], [32], [33], [34], [35], [36], and retinal angiography, e.g. [18], [37], [38], [39], [40].

In order to illustrate the methods proposed to identify vessels in retinal images, algorithms have been grouped in five classes: local operators, matched filters, morphological processing and curvature estimation, pixel-based classification and vessel tracking. It must be noted that this categorization is only functional to a simpler narrative, as most methods include several techniques belonging to different classes of approach.

4.1.1 Local Vascular Segmentation

This set of approaches to vessel segmentation try to exploit the fact that, usually, retinal vessels are darker than their surroundings. Global or local threshold and morphological operators on the image have been proposed to identify the connected regions that represent vessels.

More recently, the local gradient of the image has been used [41], [42] as a method able to recognize the edge pairs that identify the vessels. The second derivative has been used to evaluate the local candidate vessel orientation [43], and then the pixels have been classified as vessel or non-vessel based on the gradient distribution.

4.1.2 Matched Filters

Matched filtering for the detection of the vasculature convolves a 2D kernel with the retinal image. The kernel is designed to model some feature in the image at some unknown position and orientation, and the matched filter response (MFR) indicates the presence of the feature. Three primary characteristics determine properties of the kernel. Vessels usually have a limited curvature and may be approximated by piecewise linear segments; the diameter of the vessels decreases as they move radially outward from the optic disc; and the cross-sectional pixel intensity profile of these line segments approximates a Gaussian curve.

A number of filter shapes have been investigated. The most proposed is a two-dimensional linear kernel with a Gaussian profile for segmentation of the vasculature. In [18], [37], [44] extruded and rotated Gaussian filters are used, together with filters based on lines [42] and partial Gaussian [40].

The profile of the filter is designed to match that of a blood vessel, which typically has a Gaussian or a Gaussian derivative profile. The kernel is typically rotated in 30–45° increments to fit into vessels of different orientations. The highest response filter is selected for each pixel and is typically thresholded to provide a vessel image. A number of strategies have also been proposed to identify true vessels from the filter response. A local entropy thresholding method has been proposed in [45]. In particular in [18] a strategy similar to a multi-resolution approach was proposed, iteratively decrementing an initial threshold, and then checking the obtained connected component for vessel likeliness.

As noted by several authors (Patton et al.[46], Heneghan et al. [47]) a MFR method is effective when used in conjunction with additional processing techniques. However, the convolution kernel may be quite large and needs to be applied at several rotations resulting in a computational overhead which may reduce the performance of the overall segmentation approach. In addition, the kernel responds optimally to vessels that have the same standard deviation of the underlying Gaussian function specified by the kernel. As a consequence, the kernel may not respond to vessels that have a different profile. The retinal background variation and low contrast of the smaller vessels also increase the number of false responses around bright objects such as exudates and reflection artifacts. Other objects within the image such as the boundaries of the optic nerve and some hemorrhages and lesions, can exhibit the same local attributes as vessels. There are also problems associated with detecting very fine neo-vascularization partly due to image resolution. In addition, the use of an overly long structuring element may cause difficulty in fitting into highly tortuous vessels. Several authors have proposed refinements and extensions which address many of these problems (Chaudhuri et al. [37]; Kochner et al. [48]; Hoover et al. [18]; Lowell et al. [49]; Yang et al. [50]).

4.1.3 Morphological processing and curvature estimation

The basic morphology of the vasculature is known a priori to be comprised of connected linear segments. Morphological operators have been applied to vasculature segmentation (Zana and Klein [51]) and also to microaneurysm extraction. Morphological processing for identifying specific shapes has the advantage of speed and noise resistance. Gregson et al. [52] utilize morphological closing to help identify veins in the automated grading of venous beading by filling in any "holes" in the silhouette of the vein created during the processing procedure.

The main disadvantage of exclusively relying upon morphological methods is that they do not exploit the known vessel cross-sectional shape. In order to overcome this limitation, Mendonca et al. [53] presented a hybrid algorithm that starts with the extraction of vessel centerlines, which are used as guidelines for the subsequent vessel filling phase. For this purpose, the outputs of four directional differential operators are processed in order to select connected sets of candidate points to be further classified as centerline pixels using vessel derived features. The final segmentation is obtained using an iterative region growing method that integrates the contents of several binary images resulting from vessel width dependent morphological filters.

4.1.4 Pixel-based classification

Several authors have investigated a number of classification methods for the segmentation of the vessels.

Artificial neural networks have been extensively investigated for segmenting retinal features such as the vasculature (Akita and Kuga [54], Gardner at al. [55]) making classifications based on statistical probabilities rather than objective reasoning. These neural networks employ mathematical "weights" to decide the probability of input data belonging to a particular output. This weighting system can be adjusted by training the network with data of known output typically with a feedback mechanism allowing retraining.

Sinthanayothin et al. [56] preprocessed images with PCA to reduce background noise by reducing the dimensionality of the data set and then applied a neural network to identify the pathology. The result of the approach was compared with an experienced ophthalmologist manually mapping out the location of the blood vessels in a random sample of seventy-three 20×20 pixel windows and requiring an exact match between pixels in both images.

Other classifying methods have been proposed. Soares at al. [57] proposed a Bayesian classifier with class-conditional probability density functions (likelihoods) described as Gaussian mixtures. Feature vectors are composed of the pixel's intensity

and two-dimensional Gabor wavelet transform responses taken at multiple scales. The Gabor wavelet proved to be capable of tuning to specific frequencies, thus allowing noise filtering and vessel enhancement in a single step. The classifier employed yielded a fast classification, while being able to model complex decision surfaces. The probability distributions have been estimated based on a training set of labeled pixels obtained from manual segmentations.

Ricci and Perfetti [58] employed a support vector machine classifier. A line detector, based on the evaluation of the average grey level along lines of fixed length, is passed through every target pixel of the image at different orientations. Two segmentation methods have been considered. The first used the basic line detector whose response has been thresholded to obtain unsupervised pixel classification. As a further development, two orthogonal line detectors have been employed along with the grey level of the target pixel to construct a feature vector for supervised classification using a support vector machine.

Staal et al. [16] proposed a system based on extraction of image ridges, which are the natural indicators of vessels centerlines. The ridges are then used to compose primitives for the vessel in the form of line elements composed by ridge pixels which belong to the same ridge. With the line elements an image is partitioned into patches by assigning each image pixel to the closest line element. Every line element constitutes a local coordinate frame for its corresponding patch. For every pixel, feature vectors are computed by evaluating the properties of the patches and the line elements. The feature vectors are classified using a knn-classifier and sequential-forward feature selection.

Although supervised classification methods have provided remarkable results, they have a noteworthy disadvantage in the necessity for configuring the classifier with training data or a 'gold standard'. This gold standard data set consists of a number of images whose vascular structure must be precisely marked by an ophthalmologist. However, as noted by Hoover et al. [18] there is significant disagreement in the identification of vessels even amongst expert observers.

4.1.5 Vessel Tracking

Vessel tracking algorithms segment a vessel between two points. Unlike the previously described techniques for vasculature segmentation they work at the level of a single vessel rather than the entire vasculature. They start from a point on a vessel and move along it as far as possible by analyzing consecutive local areas, e.g. drawing scan lines across the vessel. The centre of the longitudinal cross-section of vessel is determined with various properties of the vessel including average width and tortuosity measured during tracking.

In order to identify the vessel profile along the scan line, matched filters are still used [18], [27], [28], [30], [38], [40], together with derivative analysis [34], [35], morphological filters [29] or Fuzzy C-Mean classifiers [39].

The main advantage of vessel tracking methods is that they provide highly accurate vessel widths, and can provide information about individual vessels that is usually unavailable using other methods.

Unfortunately, they require the starting point, and usually the end point, of a vessel to be defined by a user and are thus, without additional techniques, of limited use in fully automated analysis. In addition, vessel-tracking techniques may be confused by vessel crossings and bifurcations (Frameet al. [19]). Teng et al. [20] address several of these problems by proposing the use of matched filters.

4.2 Methods

The rationale of our method is to consider the image as a weighted un-oriented sparse graph where each node represents a pixel. The graph edges describe the 8-adjacency among pixels in the image. Under the assumption that vessels are minimum cost paths connecting remote nodes, we employ a graph search approach in order to identify them.

As a first step, luminance and contrast drifts are removed from the images using a correction method previously developed [26]. This pre-processing also ensures uniform and invariant inter-image contrast and luminosity. Then a simple grayscale opening provides an appreciable reduction of the luminosity of the arterial central reflex, whose presence would often hamper the correct tracking of large vessels. A seed point extraction identifies a set of points used as starting nodes for simultaneous searches. The most promising node to be expanded is selected at each iteration. When such node resides also in the exploration frontier of another node, the shortest path connecting the two is recorded, and considered as starting point for a new search. A subsequent refinement step connects the vessel segments with a custom fixing algorithm. In order to locate the estimated axis at the very middle of the vessel, the transversals symmetry along the axis is computed and its position is coherently adjusted. Lastly, a false vessel detection procedure evaluates a "vesselness" function in order to discriminate the true positive vessels from the ones which are to be discarded.

4.2.1 Preprocessing

Luminance and contrast drifts are removed using the iso-illumination method described in [26]. This pre-processing step also ensures uniform inter-image contrast and luminosity, therefore ensuring luminance and contrast invariance.

A second preprocessing step consists in a grayscale opening. Such morphological operation could be considered a naïve approach, since the results of its application depend only on geometrical information. However, in this specific instance, the peculiar features of the graph search algorithm we employed have demonstrated to couple optimally with this operation.

The main reason to employ a grayscale opening consists in the possible presence of central reflex in the retinal arteries and arterioles. In some datasets only a few (if not any) images show central reflexes (sometimes hardly appreciable), while certain datasets have almost all images with a marked central reflex. Namely, while STARE and DRIVE datasets are composed of images in which arteries and veins look almost the same, all the UoW Dataset images show a very marked central reflex in the arteries. This feature alone could strongly hamper a vessel tracking strategy not designed to tackle it. However, the consistency of a tracking algorithm able to track both a "normal vessel" and a vessel with a marked central reflex would come with an increased complexness of the algorithm and the loss of efficiency in the tracking process.

The grayscale opening allows the "filling" of the central of the arteries reflex with a relatively affordable drawback: it merges vessels that are closer than the dimension of the structuring element used. As explained in Sec. 4.3 the false vessel detection easily allows to get rid of those spurious tracked segments.

In grayscale morphology, images are functions mapping a Euclidean space or grid E into $\mathbb{R}\cup\{\infty,-\infty\}$, where $\mathbb{R}$ is the set of reals, ∞ and $-\infty$ are elements respectively larger and smaller than any real number. Grayscale structuring elements are also functions of the same format, called "structuring functions". Opening is the dilation of the erosion of an image *f(x)* by a structuring element *b(x)*:

$$f \circ b = (f \ominus b) \oplus b \tag{4.1}$$

where $\ominus$ and $\oplus$ denote erosion and dilation, respectively. In this application we used a flat structuring element. Flat structuring functions are functions *b(x)* in the form

$$b(x) = \begin{cases} 0, & x \in B \\ -\infty, & otherwise \end{cases} \tag{4.2}$$

where $B \subseteq E$. We are in a bounded, discrete case (E is a grid and B is bounded) so the grayscale erosion of f by b is given by

$$(f \ominus b)(x) = \min_{z \in B} (f(z - x)) \tag{4.3}$$

while the grayscale dilation of f by b is given by

$$(f \oplus b)(x) = \max_{z \in B} (f(z - x)) \tag{4.4}$$

Since we can expect that the width of a central reflex is between 1 and 6 pixels, depending on the µm/pixel ratio of the image, we conservatively chose the dimension of the structuring element depending on the image dimension, namely a 2 pixel radius disk in the DRIVE and STARE datasets, and a structuring element of 4 pixel radius disk in the DB60 and UoW datasets.

Figure 4.1 shows the appearance of an example image after erosion and then after dilation with different structuring element dimensions. Figure 4.2 shows an example of both the advantages and the disadvantages that can be obtained by employing the morphological operation.

(a) original image

(b) erosion with disk of radius 1

(c) opening with disk of radius 1

(d) erosion with disk of radius 2

(e) opening with disk of radius 2

(f) erosion with disk of radius 3

(g) opening with disk of radius 3

(h) erosion with disk of radius 4

(i) opening with disk of radius 4

Figure 4.1 (a) original image and the image results of the erosion with a disk of radii 1, 2, 3, and 4 (left column), and a subsequently dilation with the same structuring element (right column).

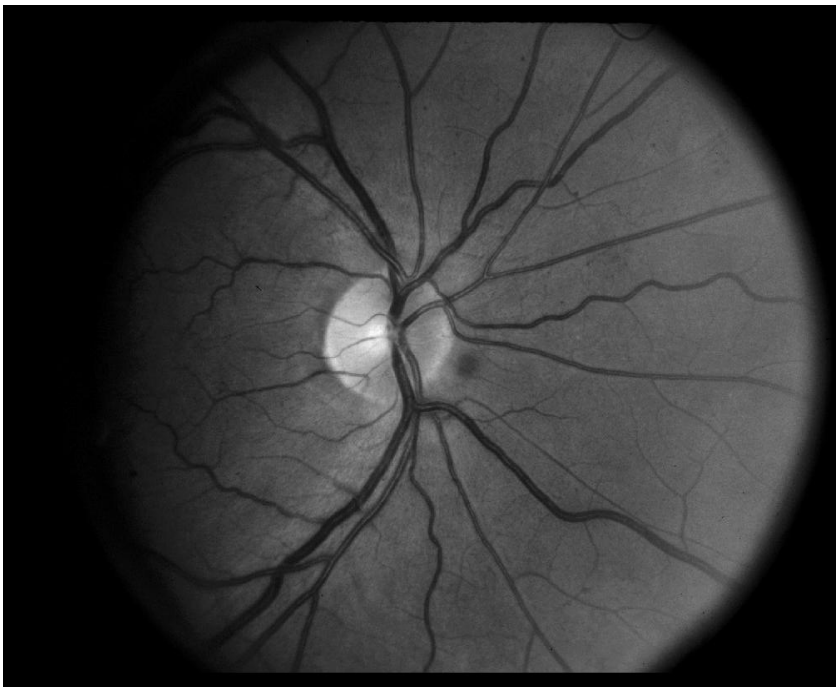

(a)

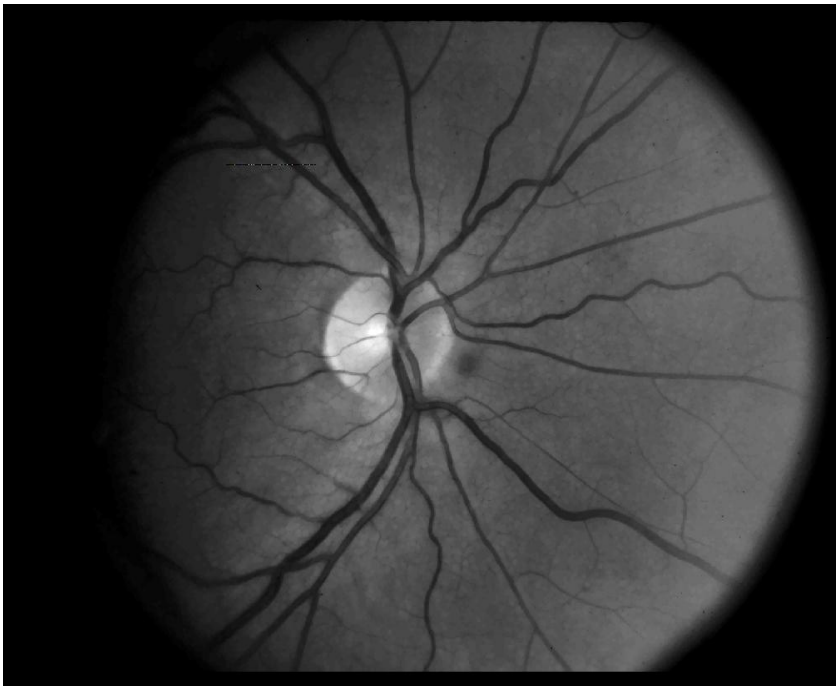

(b)

Figure 4.2 (a) An example image from the UoW dataset; (b) after opening with a disk of 4 disk radius. While the central reflexes become quite attenuated, some vessels are erroneously merged.

4.2.2 Seed-Finding Procedure

An initial seed-finding algorithm, based on multi-scale matched filters over two regular grids, is run (Figure 4.5).

The objective of this module is to extract a set of points (seeds) from which the tracking step will start. Since the whole point of the *sparse* tracking procedure is to ensure that even non-connected vessels can be tracked, these seed points should be as spread-out as possible in the image. In order to do this, a number of lines of the image are analyzed to search for candidate seed points. From each selected line the gray-level profile $p(x)$ is extracted and analyzed by means of a matched filter method, looking for patterns corresponding to candidate vessels. The convolution of the profile with a discretized Laplacian of Gaussian function filter over multiple scales is performed. The output of each filter is then normalized, and the maximum response among the output results is considered (see Eq. 4.5 and Eq. 4.6).

The response of the convolution depends on the angle defined by a vessel and the line, from which the profile is extracted, it crosses. As we would to maximize the difference of appearance in the profile between background and vessel, the aim is to define the grid lines as perpendicular as possible to the vessels.

We opted to design two regular grids: one of equally spaced rows and columns and the other equal but rotated by 45°. As can be seen in Figure 4.3 and Figure 4.4, the

two differently oriented grids allow locating seed points over differently oriented vessels.

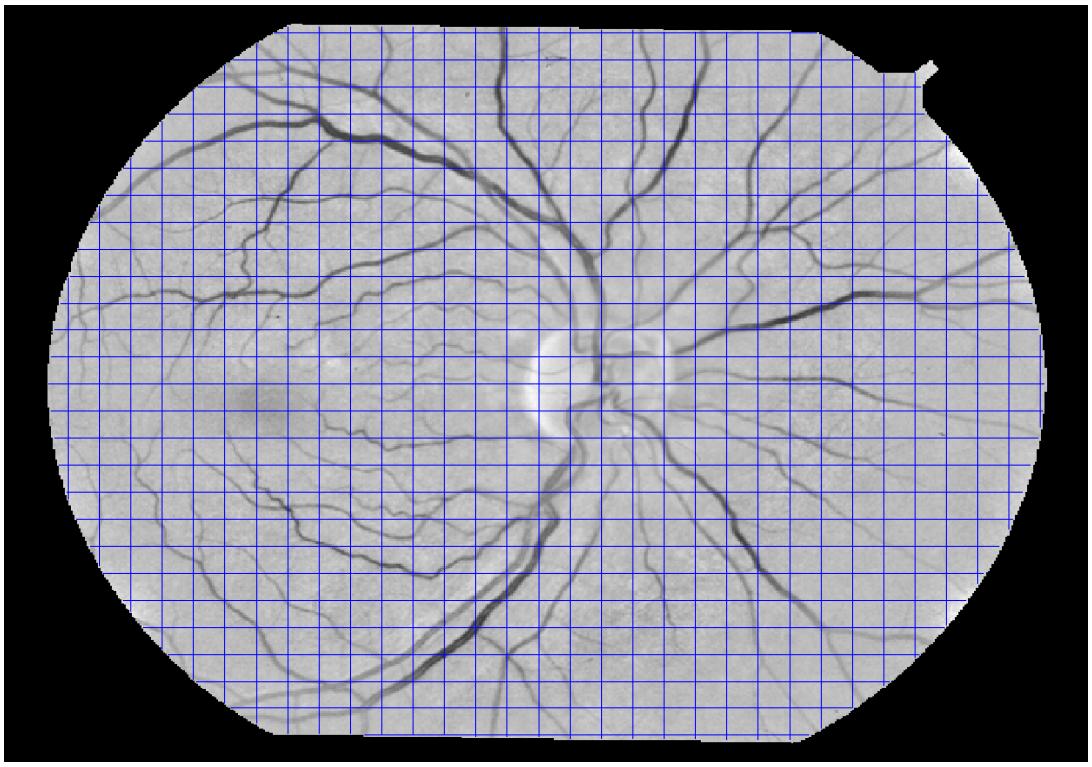

(a)

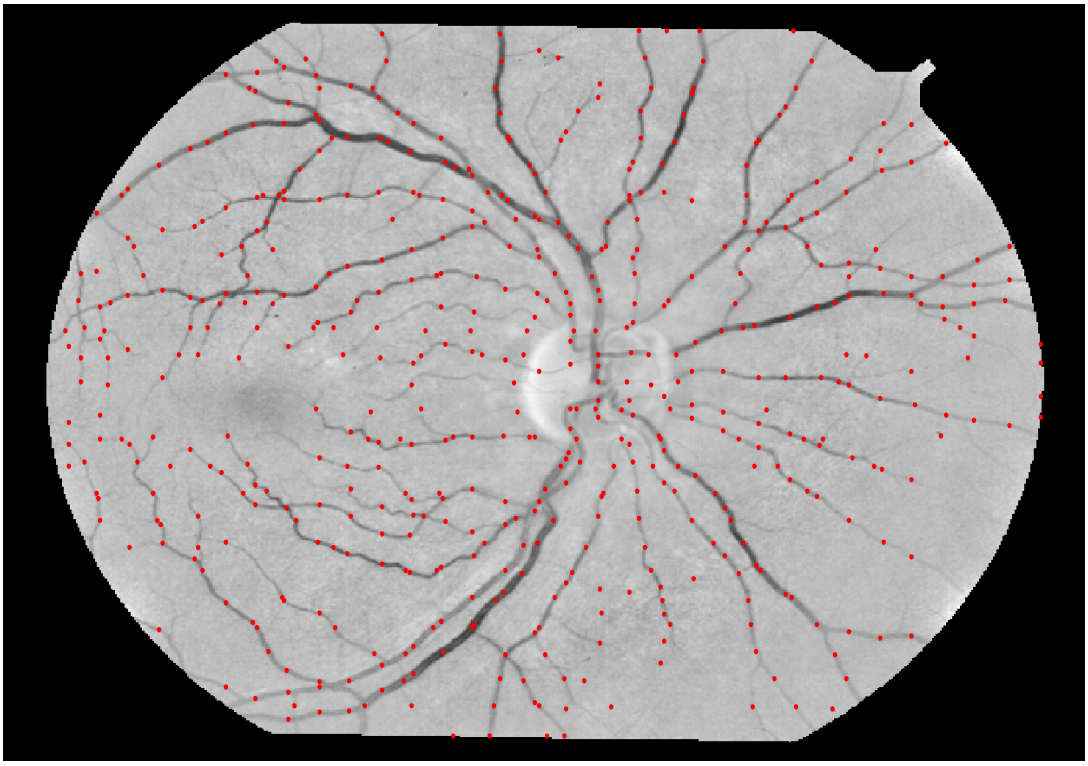

(b)

Figure 4.3 (a) regular grid of equally spaced rows and columns and (b) the corresponding seeds found.

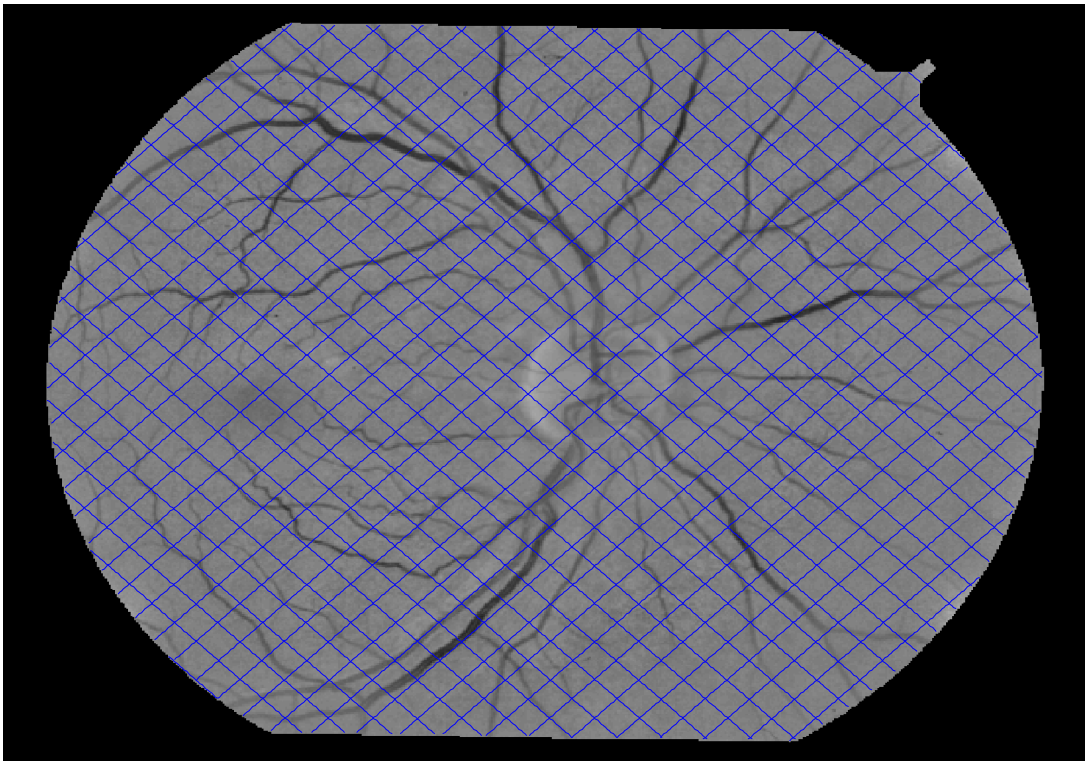

(a)

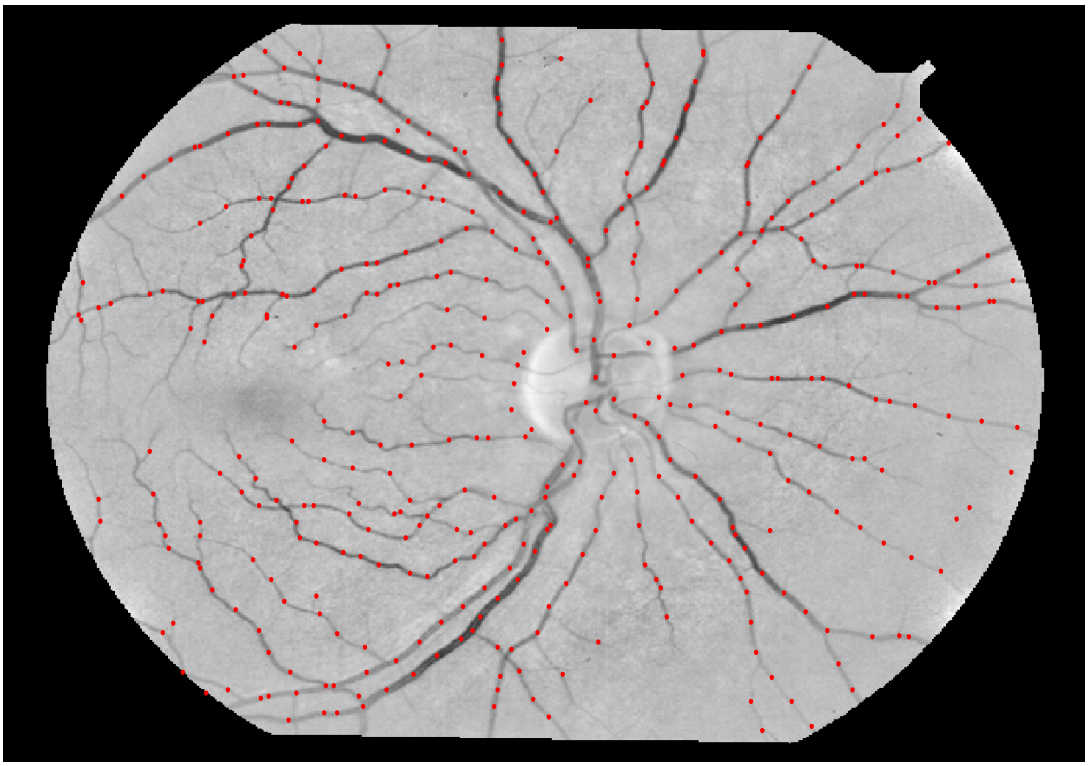

(b)

Figure 4.4 (a) regular grid of equally spaced perpendicular lines, at an angle of 45° with the image coordinates; (b) the corresponding seeds found.

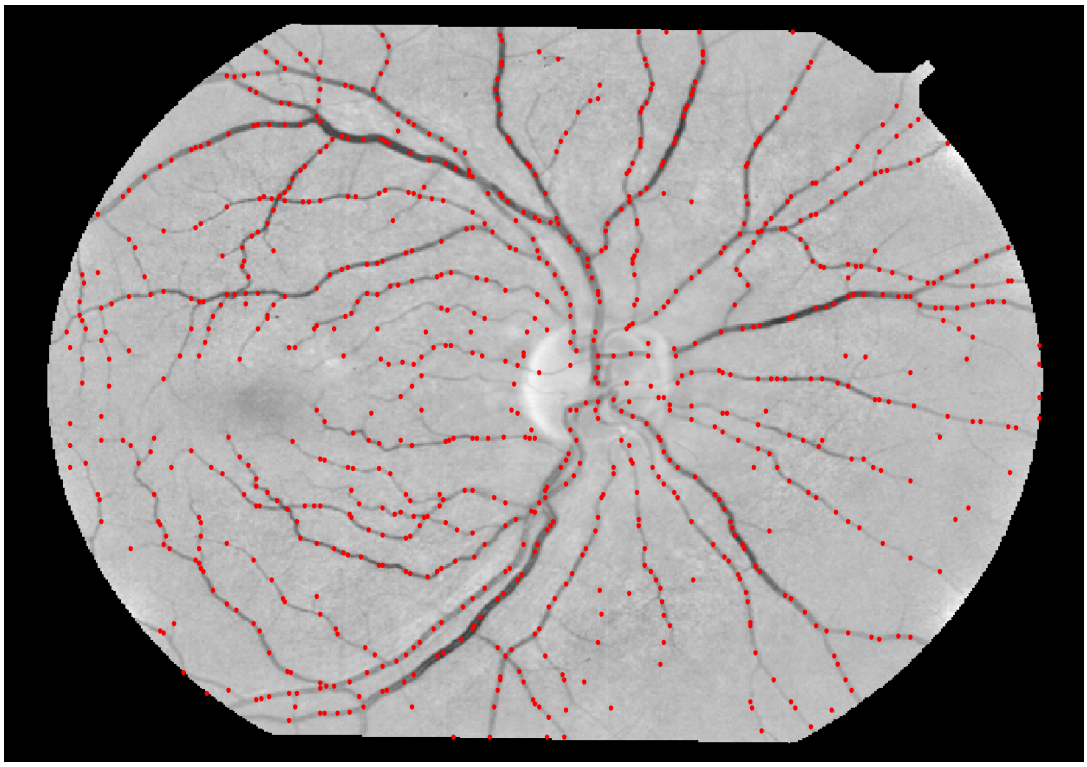

Figure 4.5 The total set of seeds found by employing both the horizontal and the inclined grids.

The 0-mean discrete filter used is described by the following equation:

$$f_{sc}(x) = \begin{cases} -1, & 1 < x \leq sc \\ 2, & sc + 1 < x \leq 2sc \\ -1, & 2sc + 1 < x \leq 3sc \end{cases} \tag{4.5}$$

where x and the scale sc are discrete values. Given the profile $p(x)$, the family of filters $f_{sc}(x)$, and a set of scales SC, the final filter response is given by:

$$res(x) = max\{\, p(x) \otimes f_{sc}(x) \mid sc \in SC \,\} \tag{4.6}$$

where $\otimes$ is the operation of convolution. Looking at the most prominent local minima of $res(x)$, we derive a set $K = \{k_i,\ i = 1{:}\,N_k\}$ of points on the profile suggesting the possible presence of vessels in the corresponding points of the image. From now on, $S = \bigcup_{\infty} K$ is the entire set of detected seed points.

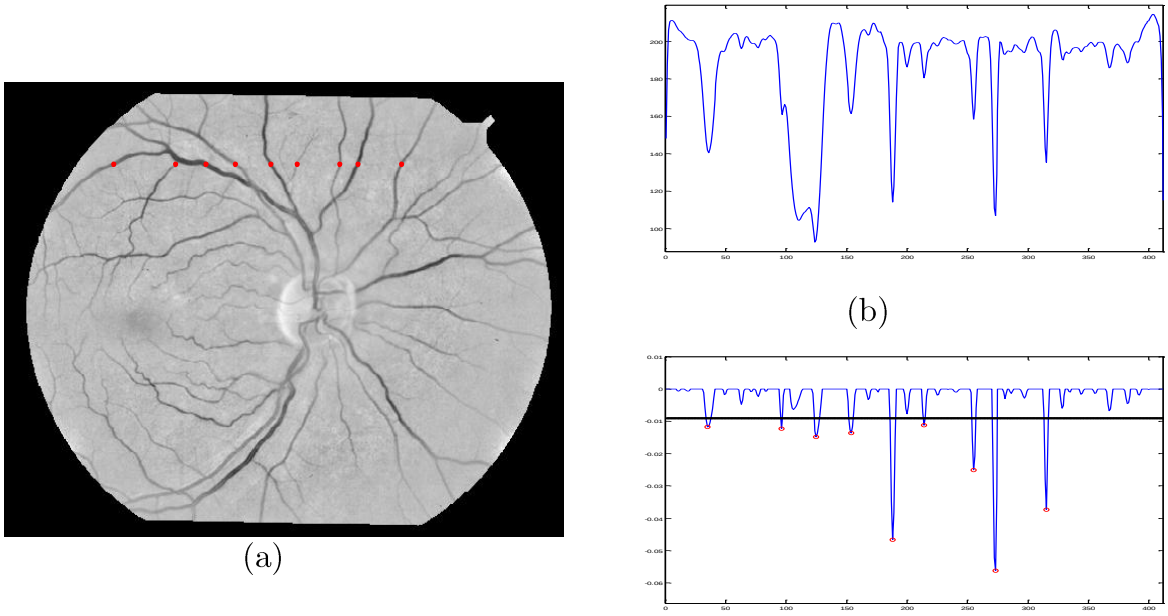

(a) (b) (c)

Figure 4.6 (a) seeds found in the image by analyzing the profile (b); (c) the profile resulting from the matched filtering is compared with a threshold.

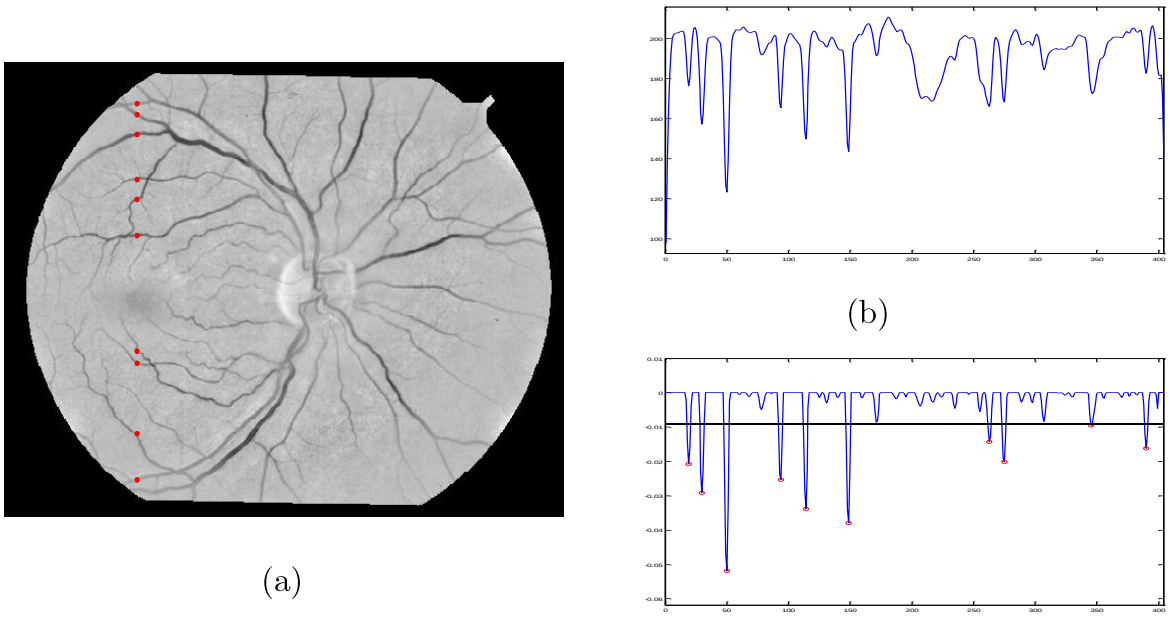

(a) (b) (c)

Figure 4.7 (a) seeds found in the image by analyzing the profile (b); (c) the profile resulting from the matched filtering is compared with a threshold.

It is worth noting that we gave more importance to the sensitivity of the seed finding procedure (detected vessels over true vessels) than to its specificity (not detected vessels over "non-vessel"). As explained in Sec. 4.2.4, the efficacy of our algorithm is not undermined by the presence of wrong seed points but rather by their lack in critical regions of the image.

4.2.3 Multi-directional Shortest Path Search Idea

The image I is a 2-dimensional array of R rows and C columns; an undirected graph $G = (N, E)$ can be derived from it. Let each node $i \in N$ be associated to the pixel $I\big(r(i), c(i)\big)$ having gray level $g(i)$. The edge $(i, j) \in E$ exists if $|r(j) - r(i)| \leq 1$ and $|c(j) - c(i)| \leq 1$. To each edge $(i, j) \in E$, a cost is associated by a real-value function $f: E \to \mathbb{R}^+$ which will be defined in Sec. 4.2.4.4. A path P in G is a sequence of nodes that are sequentially connected by edges in E. A path P connecting the nodes $a, b \in N$ is the shortest one if $\sum_{(i,j)\in P} f(i, j)$ is minimal among all paths connecting a to b.

Given a graph G and a node s, the shortest path tree problem consists in finding a spanning directed tree T^* rooted at s such that the cost of all paths in T^* from s to all other nodes is minimal in G. Algorithms that compute T^*have a common scheme: starting from an initial tree $T(0) \subseteq T^*$, they iteratively update it until, at the iteration n, $T(n) = T^*$ is found. The problem can be solved by the Dijkstra algorithm [59], which can also be used for finding the shortest path from two single vertices by early stopping the algorithm at the iteration n in which $T(n)$ meets the target vertex (without computing the entire T^*). This latter problem can be solved by a bidirectional search approach [60], which, for a running time profit, runs two simultaneous searches: one from the initial state and one from the goal, and stops when the two $T(n)$ meet.

The specific problem we are dealing with, however, requires the connection of several nodes. The scheme of the proposed algorithm is to run multiple shortest path searches, each starting from the seeds found according to the procedure described in Sec. 4.2.2. When two trees meet, they provide the shortest path connecting their roots, but differently from the bidirectional approach, the algorithm does not stop. Instead, the two trees merge into a single new tree, from which the search goes on in successive iterations.

4.2.4 The Algorithm

4.2.4.1 Initialization

Every $s \in S$ is considered as the root of a tree T_s. A different identification tag is assigned to each tree, so that for every explored node it is possible to trace which tree it belongs to. Also, every node $i \in T_s$ carries two additional pieces of information: the distance d_i providing the total cost of the path from i to s, and the reference p_i indi-

cating the predecessor of i in $T_s(n)$. At the first iteration ($n = 0$), every $T_s(0)$ coincides with its root s and d is equal to zero for all $s \in S$, whereas for all other nodes of the graph d is assumed to be ∞.

Algorithm 1 Initialization

```
1: function INITIALIZE(S, G)
2:     for all s ∈ S do                          ▷ for all seeds
3:         d_s ← 0                               ▷ distance from the source
4:         tag_s ← s                             ▷ tree to which the node belongs
5:         p_s ← ∅                               ▷ predecessor in the tree
6:         state_s ← leaf                        ▷ exploration starts from leaves
7:     end for
8:     for all n ∈ N(G)\S do                     ▷ for all other nodes
9:         d_n ← ∞
10:    end for
11: end function
```

4.2.4.2 Search

At each iteration n, the leaf node i with the minimum distance, i.e. such that

$$i(n) = \text{argmin}_i\{d_i \mid i \in \bigcup \textit{ leaves of all } T(n)\} \tag{4.7}$$

is selected. The set $J(n)$ of the nodes reached by the outgoing edges of $i(n)$ is considered. If there is a node $j \in J$ that belongs to another search tree, then the two trees are merged (See 4.2.4.3). Otherwise, all $j \in J$ are explored to expand the current T: the cost function f, defined below, is computed and for each j such that $f(i,j) < d_j$, then d_j and p_j are respectively updated to $f(i,j)$ and i.

Algorithm 2 Multidirectional Graph Search

```
1: function MULTISEARCH(S, G)
2: INITIALIZE(S,G)
3:     P ← ∅
4:     repeat
5:         i ← arg min_i {d_i | state_i = leaf, i ∈ N(G)}
6:         state_i ← explored
7:         for all j | (i, j) ∈ A(G) do
8:             if tag_j ≠ tag_i, state_j = explored then
9:                 P ← P ∪ MERGE(i, j, G)
10:            else
11:                state_j ← leaf
12:                tag_j ← tag_i
13:                newdistance ← COSTFUNCTION(i, j)
14:                if newdistance < d_j then
15:                    d_j ← newdistance
16:                    p_j ← i
17:                end if
18:            end if
19:        end for
20:        ec ← EVALUATEENDCONDITION(P, G)
21:    until ec
22: return P
23: end function
```

4.2.4.3 Merging

The merging operation consists of two steps. First, the minimum path is reconstructed by exploiting the references p, i.e. step by step backward from the node i and from the node j along their respective tree, until a seed point $s \in S$ is reached or until a node belonging to a previously found path is reached. Second, the two exploration trees are merged: all nodes belonging to the two touching trees have their identification tag equaled. This operation allows the resulting merged tree to coherently interact with the others in succeeding iterations.

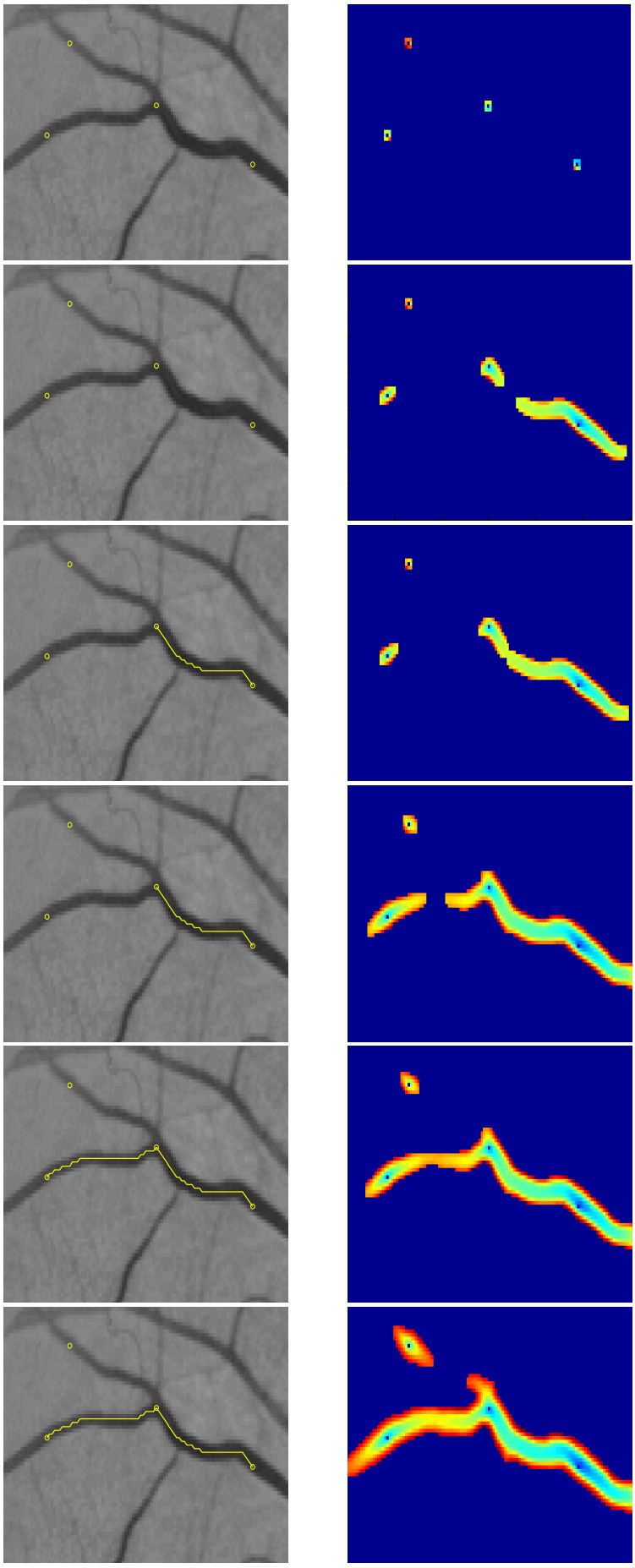

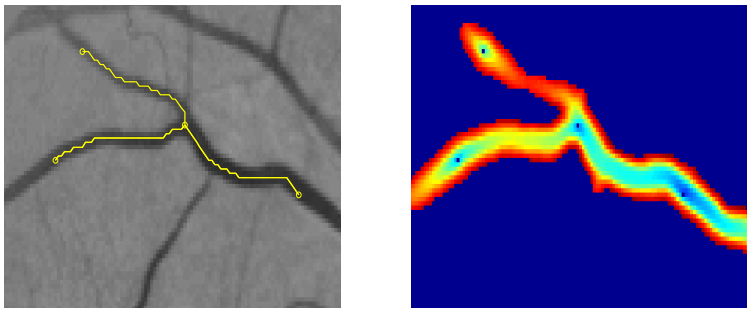

Figure 4.8 Example of exploration of four manually deployed seeds. On the left column the original image with the superimposed seeds and the identified paths. On the right column, the images of the matrix where for each pixel i the distance value d_i is stored.

4.2.4.4 Cost Function

We defined the cost function associated to the edge (i,j) as described by eq. (4.8) and (4.9), where $g(i)$, recalling from Sec. 4.2.3, is the gray level of the pixel represented by the node i.

$$f(i,j) = d_i + k_{i,j}w_{i,j} \tag{4.8}$$

$$k_{i,j} = g(i)^{p_1} + |g(i) - g(j)|^{p_2} \tag{4.9}$$

where the weight $w_{i,j}$ has the role of penalizing the exploration of the d-adjacent pixels of i: $w_{i,j} = 1$ if i and j represent 4-adjacent pixels, otherwise $w_{i,j} = \sqrt{2}$ (Figure 4.9).

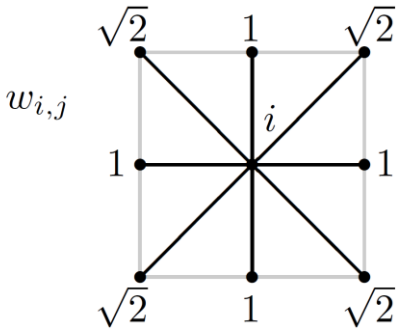

Figure 4.9 Starting from i, the weight $w_{i,j}$ has the role of penalizing the exploration of the d-adjacent pixel as their distance is $\sqrt{2}$ times the distance of the 4-adjacent pixels.

The first term of the sum (4.9), $g(i)^{p_1}$, penalizes the exploration of brighter pixels, while the second term, $|g(i) - g(j)|^{p_2}$, penalizes the transition from the inside to the outside of the vessels and *vice versa*. p_1 and p_2 are empirically chosen: however, we noted that if both p_1 and p_2 are ≥ 3, the performances provided by the algorithm tend to be good and are qualitatively similar for every arbitrary chosen value.

4.2.4.5 End Condition

It is worth noticing that, according to the defined f and the appearance of the regions around the false positive seeds, the exploration starting from the latter tends to be done at a later time than the one from the true positive seeds. Indeed, in the last iterations only false positive seeds remain to be connected. An end condition has been defined in order to exploit this feature, minimizing the occurrence of false vessels detection.

In order to provide a more solid end condition, we defined it as a sequence of two checks: when the first check is verified the second one is performed.

The rationale of the first check is to consider the degree of connectivity of the estimated vessel network after a cyclic number of iterations. We considered the estimated vessel network as a set of trees in which the edges are the vessel segments, the nodes correspond to the bifurcations among vessel segments, and the leaves of the trees are the ends of the vessel segments. It is worth noticing that the trees mentioned in this circumstance have no relations with the search trees described in the previous sub-sections, since they are defined at different conceptual levels and have different purposes.

A perfect binary tree of height h has a number of nodes $n = 2^{h+1} - 1$ and a number of leaf nodes $l = 2^h$. It can be easily seen that the l/n ratio tends to ½ as h tends to infinite, and $l/n^* = ½$ is the lower bound of each possible binary tree. The behavior of the search algorithm can be qualitatively described as follows: in a first stage seed points are connected in pairs, and only after a number of iterations the other non-connected seed points are connected to the segments already found. In other words, in the first stage of the processing the number of leaves (i.e. ends) is far larger than the number of total nodes (i.e. ends plus bifurcations). However, the more the iterations of the algorithm, the more the network becomes connected, approaching towards the l/n^* ratio. Of course we cannot expect that a retinal vessel network geometry behaves like a perfect binary tree, but we empirically noticed that as the best compromise between false vessel detection and true vessel network covering was reached, $log\left(\frac{l}{n}\right) \cong 1$. This last threshold defines one of the two checks constituting the end condition of the tracking algorithm. Since in the earliest iterations of the algorithm the l/n ratio value could be very unstable, the check starts to be performed after a short delay "of confidence". The limit of such approach is that it can work on-

ly under the assumption that the processed image is a processable image (in the other case the whole proposed framework would not be able to provide the desired results).

The second check becomes active only when the first one is verified, i.e. when $log\left(\frac{l}{n}\right)$ reaches the threshold value. From now on, every new path found is accepted only if the average gray level of its pixels significantly differs from the local average value of the preprocessed image. When three paths are consecutively discarded in this way, the algorithm ends, since it is assumed that the remaining paths cannot be better than those already found. It is worth noting that this step is effective only if it is applied to images whose luminance and contrast drifts have been removed as previously mentioned [26].

4.2.5 Post-Processing

A fault of the proposed algorithm is that it allows to connect N given seed points with at most only N-1 paths. Another drawback is the algorithm intrinsic inability to find circular paths [61]. To overcome these limitations, we have developed a fixing procedure that aims at finding possible missing branches in the vessel network reconstructed up to this point.

The rationale is to consider every end-point of the current vessel network and try to find an additional path that starts from it and proceeds beyond it to arrive at another point of the network. The segment of the current network ending at the end-point is smoothed, so as to provide a robust estimate of the perpendicular line at the end-point, which identifies the "forward" region to be explored by the fixing procedure.

The algorithm presented in Sec. 4.2.4 is then run once more, using all the end-points as seeds and having the constraint to explore the "forward" region only, without being allowed to backtrack along the vessel already traced. In this new instance of the algorithm, the threshold value of the first check of the end condition is updated to $log(l/n) = 0.3$.

4.3 False Vessel Detection

The tracking of false vessels, i.e. to consider something that is not vessel as vessel, depends mainly on the position of false seed points located in darker regions of the fundus image (such as in the fovea) or in hemorrhages.

In order to develop a false vessel detector that is able to perform well on the errors of the tracking algorithm, we have to describe vessels with features as different as possible if compared to the ones used in the tracking process. In this section we present a binary classification method based on a measure of "vesselness" determined

by the analysis of the eigenvectors of the Hessian matrix computed on the vessel axes [62].

All vessels share the same feature: in their inside, along the axis, they show gray scale uniformity, with only exceptions of in the case of a small gradient due to the slow change of luminosity through the image and the possible appearance of central reflexes. The rationale is to employ the information on the direction of the gray level gradient along the estimated axis: if this proves constant and coherent with the axis direction, we can assume that the estimation was correct. On the contrary, a fast and casual variability in the gradient direction is characteristic of the background region.

The computation of the direction of the gray level gradient is easily obtainable from the analysis of the eigenvalues and eigenvectors of the Hessian matrix

$$H_{x,y} = \begin{bmatrix} \frac{\partial^2 L}{\partial x^2} & \frac{\partial^2 L}{\partial x \partial y} \\ \frac{\partial^2 L}{\partial y \partial x} & \frac{\partial^2 L}{\partial y} \end{bmatrix} \tag{4.10}$$

whose elements are determined by the convolution of the image with the second-order partial-derivatives of a two-dimensional Gaussian distribution G. In order to keep the computational load low, the convolution is calculated only in correspondence of the pixels covered by the estimated axes.

Once the convolutions have been performed, it is possible, for every pixel, to determine the Hessian matrix. Since it is symmetric, its eigenvectors are orthogonal and represent the main directions in which the local two-order structure is decomposed. The two eigenvectors ν^+ and ν^-, associated with the eigenvalues λ^+ and λ^-, indicates respectively the direction of faster change (ν^+) and lower change in intensity.

For each pixel of the estimated axis, the difference d between the angles of the vessel axis direction and the direction of ν^- is computed. We can notice that as the estimated axis leaves a vessel, entering the background region, d becomes unstable.

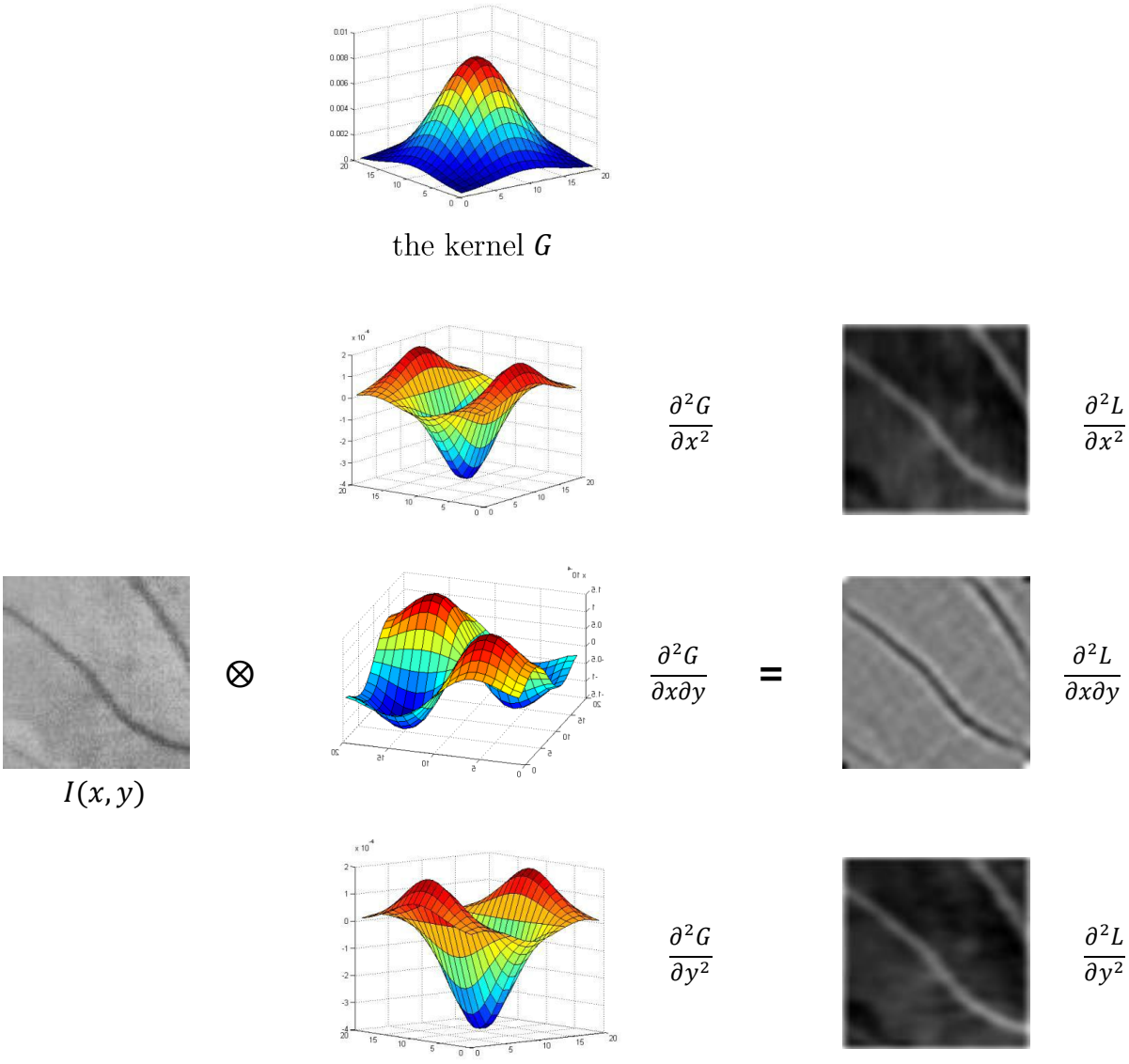

Figure 4.10 Simple scheme that highlights the usefulness of the second derivative of the kernel G and the three obtained components.

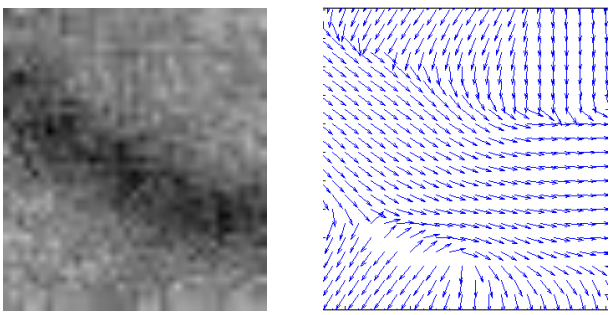

(a) (b)

Figure 4.11 (a) Detail of a vessel and (b) the ν^- corresponding to each pixel.

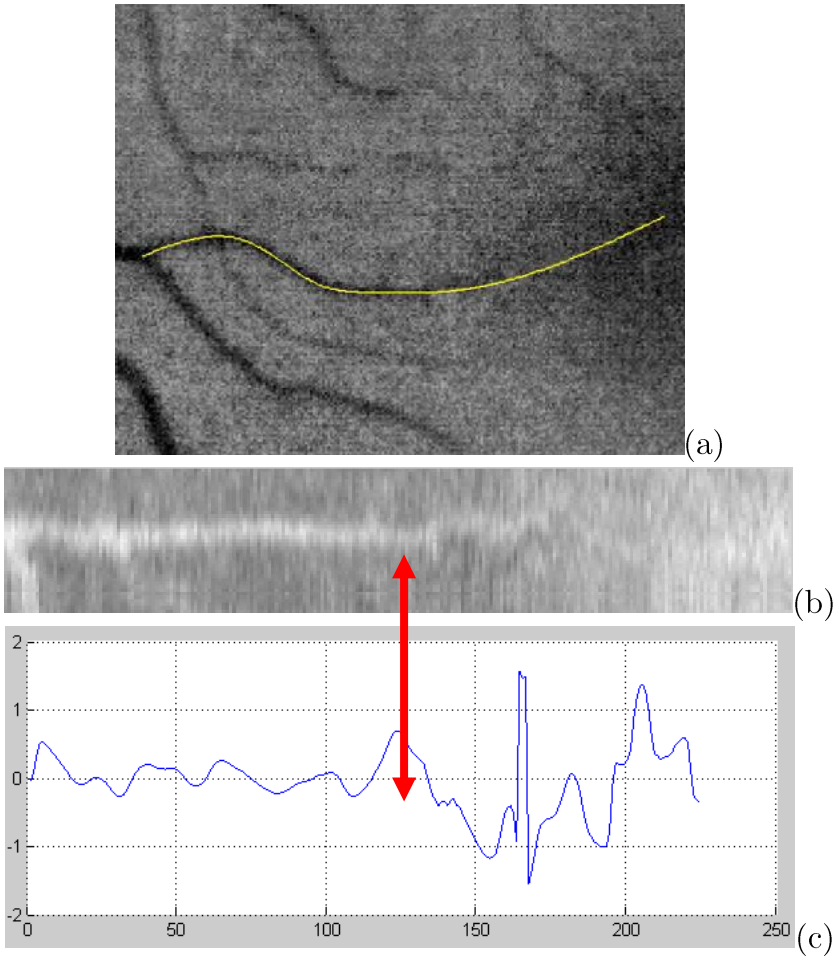

Figure 4.12 (a) Partially false tracked vessel: the second half has been detected because of false seeds laying in the fovea; (b) image of the vessel composed by taking into consideration the longitudinal profiles of the axis (displayed to provide a straightforward view); (c) difference between the angles (in radians) of the vessel axis directions and the directions of ν^{-}, along the estimated axis.

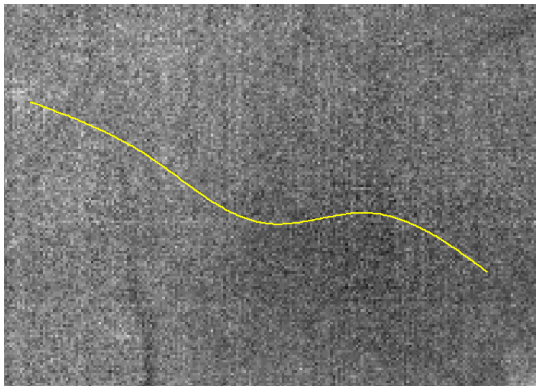

(a)

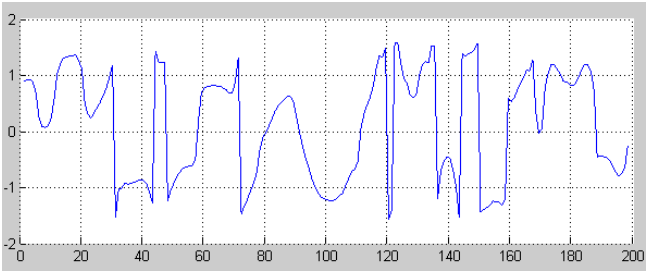

(b)

Figure 4.13 (a) vessel axis manually drawn on the background; (b) difference between the angles (in radians) of the vessel axis directions and the directions of ν^{-}, along the estimated axis.

The rationale is to classify the pixel of the axis as false vessel pixel when the corresponding d goes outside an interval of confidence, which has been empirically set to $\pm 0.2\pi$. Since the value of d computed on a background region is casual, it could happen that, for a number of false vessel pixels, d falls in the confidence region. This is the reason why after the pixel-wise classification provided by the thresholds we introduced a further verification, which tests the "choppedness" of the true-classified pixel along the axis. Simply put, a segment of axis is considered true vessel if it is composed of more than 20 consecutive pixels whose d falls in the interval of confidence.

This described implementation for the false vessel detection reached an average sensitivity of 63.8%, an average specificity of 91.9%, and a total average accuracy of 88.5 % on the DB60 dataset.

4.4 Results

The performance of the algorithm is compared with the human-labeled segmented version of the 60 images of our DB60 dataset, of the 20 test images of the DRIVE dataset, and of the 20 images of the STARE dataset, all of them assumed as ground-

truth reference. Those segments of the computer-estimated network that do not exist in the ground-truth images (i.e., that exit from the vessel mask) are considered as false vessels. *Sensitivity* has been evaluated as the percent fraction of the length of correctly tracked vessels over the total length of the ground-truth vessels (skeletonization of the ground-truth vessel mask). *False vessel detection* has been evaluated as the percent fraction of the length of the false vessels over the length of all estimated vessels (not to be confused with the *false detection rate*). Results are summarized in Table 4.1, Table 4.2, and Table 4.3 in terms of mean, standard deviation, maximum and minimum of both sensitivity and false vessel detection over the whole data sets.

DB60	mean	sd	max	min
sensitivity	85.86	4.72	98.31	76.58
false detection	5.18	2.11	10.71	0.98

Table 4.1 Results of the vessel estimation in the 60 images of the DB60 dataset (%).

DRIVE	mean	sd	max	min
sensitivity	71.37	6.09	86.29	55.83
false detection	4.82	2.36	8.04	1.47

Table 4.2 Results of the vessel estimation in the 20 test images of the DRIVE dataset (%).

STARE	mean	sd	max	min
sensitivity	66.34	5.3	82.04	55.25
false detection	3.07	2.21	8.30	0.92

Table 4.3 Results of the vessel estimation in the 20 images of the STARE dataset (%).

The average run time of the MatLab® prototype of the whole algorithm on a Intel Pentium-M PC (1.8 GHz, 1 GB of RAM) is 60 seconds, while on a Intel Duo Core 2 PC (2.2 GHz, 4 GB of RAM) is 25 seconds.

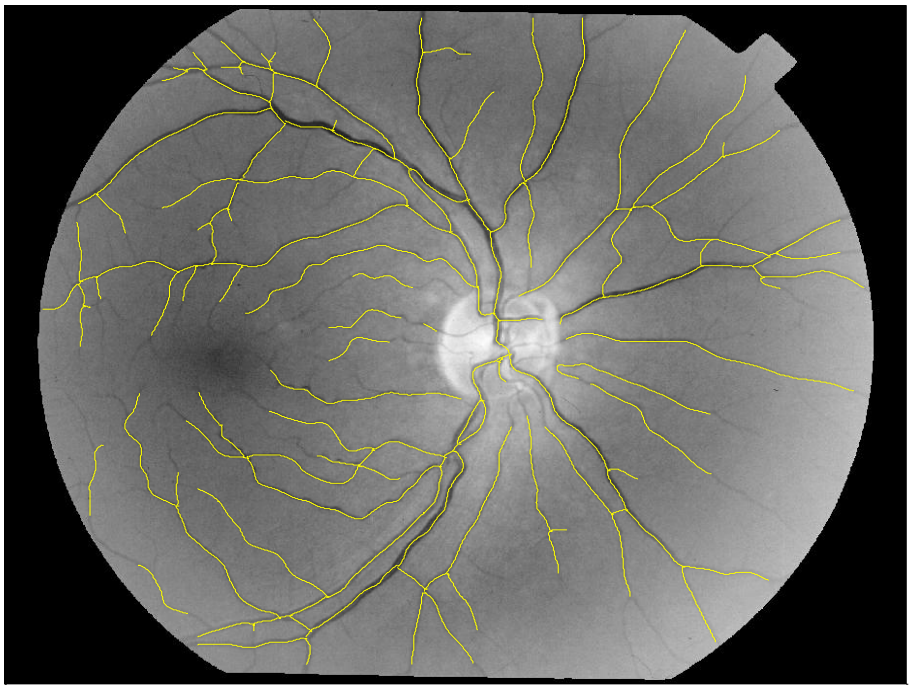

Figure 4.14 Example of vessel axis tracking results (DB60 dataset).

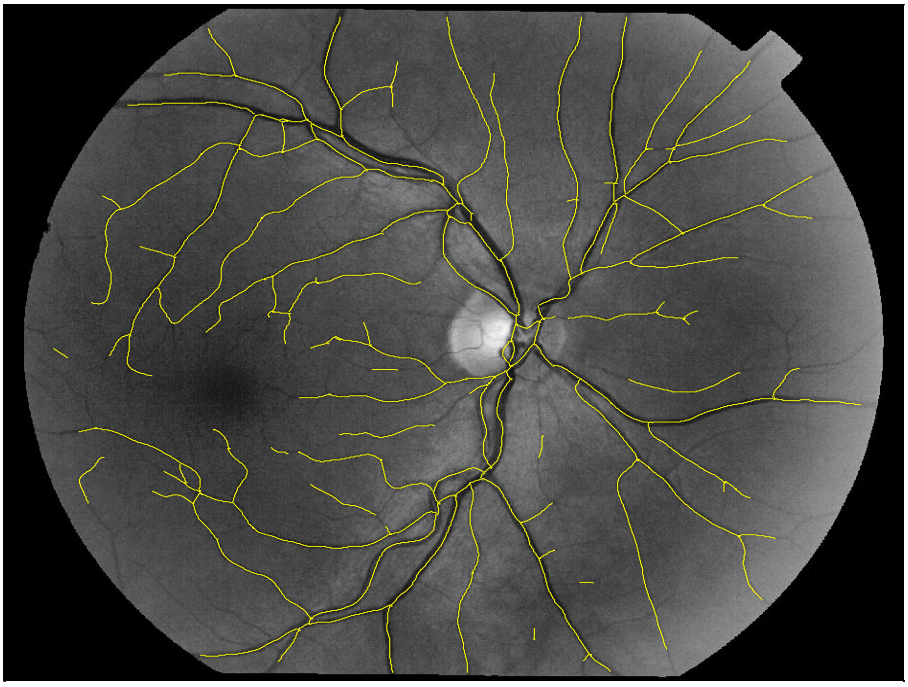

Figure 4.15 Example of vessel axis tracking results (DB60 dataset).

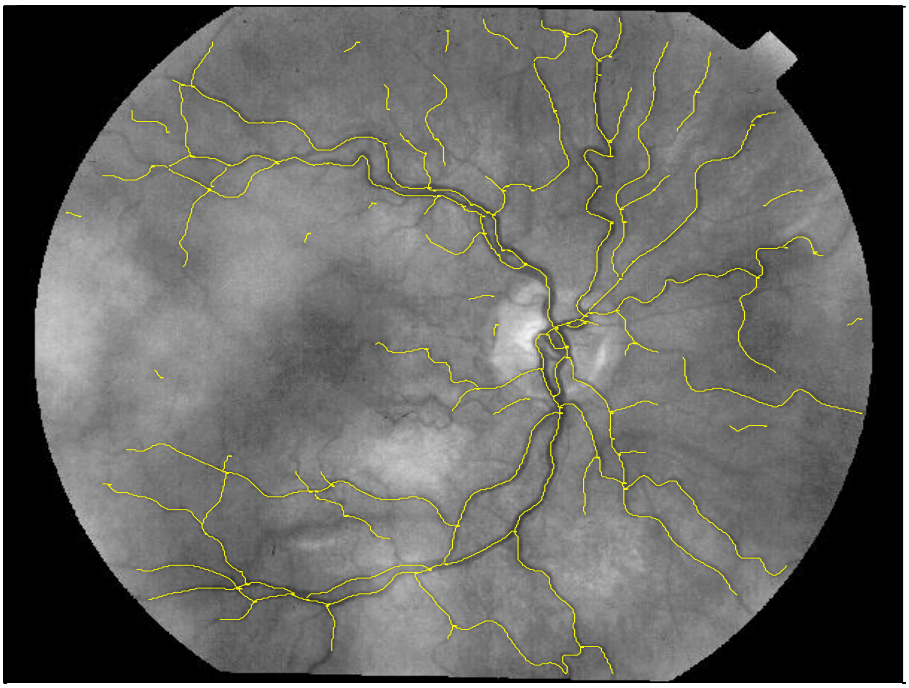

Figure 4.16 Example of vessel axis tracking results on a pathologic image (DB60 dataset).

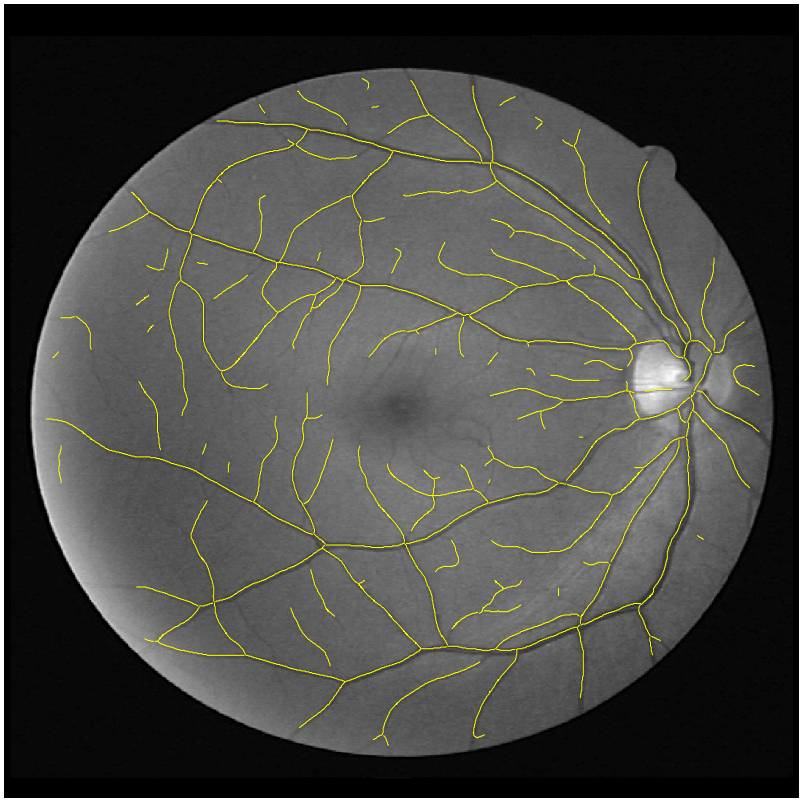

Figure 4.17 Example of vessel axis tracking results (DRIVE dataset).

Figure 4.18 Example of vessel axis tracking results (STARE dataset).

How it can be seen in Table 4.1, Table 4.2, and Table 4.3 the mean sensitivities of the method are quite different in the three datasets. This different behavior can be explained in term of the image features and the ground-truth manual labeling.

The images from different datasets have different field of view and resolution: DB60- 50°, 1400x1200 pixels; DRIVE- 45°, 768x584 pixels; STARE: 35°, 605x700 pixels. In these last two datasets, the smallest capillaries manually segmented by human observers are 1-2 pixels wide, while in DB60 the smaller capillaries manually segmented are about 3-4 pixel wide. The proposed method has not proved to be able to detect these very small vessels mainly because the seed finding procedure is not able to detect them.

Still, the DB60 dataset is the one on which the algorithm presents the highest false vessel detection, i.e. 5.18%, versus 4.82% and 3.07%. Even this behavior can be explained by the same considerations reported above. In fact, as we made the algorithm more sensible towards the small vessel of the DRIVE and STARE images, small capillaries and spurious grains not present in the ground-truth mask of DB60 were found. The false vessel detection step described in Sec. 4.3 has proved to be particularly helpful in the post-processing of the DB60 images, while its contribution has been minimal with the other two datasets.

An additional consideration can be made about the capillaries. The evaluated results are computed by comparing the length of the estimated vessel axes with the length of the ground-truth vessel mask skeletonization. Therefore, wide and narrow vessels are equivalent in the computation of the performance of the algorithm and the missed detection of a large vein produces the same error as the missed detection of a

narrow capillary with the same length. This is true of course also for the false vessel detection.

4.5 Conclusion

This chapter describes a new automatic system to extract the vessel structure in retinal images acquired from adult subjects, based on a multi-directional graph search algorithm. In its present form the method has proved robust with respect to initial false positive seeds and efficient in the tracking process. Its main drawbacks are the difficulty of detecting small capillaries of 1-2 pixel diameter and the different behavior with different datasets.

Our objective was to develop a vessel segmentation method able to find the central axis of the retina vessels, leaving the detection of the vessel border to a successive step. The partition of the segmentation process in two sequential and independent tasks provides some advantages. Two considerations can be made on this issue.

First, we could use a tracking method that does not require to identify the longitudinal cross-section of the vessel and thus to detect the vessel diameters, allowing us to choose a technique that analyzes fewer pixels. The method proposed here uses the Dijkstra's algorithm, revised and expanded in order to connect multiple source points. The Dijkstra's algorithm has been widely studied, is well known, and its implementation can be highly optimized for both computational cost and memory occupancy. Since it is at the core of the tracking algorithm, the whole system benefits from its efficiency. The average run time of our MatLab® implementation of the sole multi-directional graph searching algorithm, ran on a single image is 30 seconds, using an Intel Pentium-M PC (1.8 GHz, 1 GB of RAM), and 15 seconds using an Intel Duo Core 2 PC (2.2 GHz, 4 GB of RAM).

The second consideration concerns the implementation of the edge detection algorithm, which will be described in details in the forthcoming Chapter 5. The rationale consists in employing an edge detection approach and using the vessel axis features as prior information. As will be described in Sec. 5.2.2 and Sec. 5.2.3, each point of the vessel axis is analyzed with a matched-filter technique, which exploits the information of the vessel local direction and a roughly estimated scale to reduce the dimension of the problem. Again, this approach allows sizable computational gain.

In conclusion, the satisfactory results obtained with this algorithm suggest the possibility of using it to identify the retinal vascular structures for clinical purposes.

Chapter 5

Vessel Diameter Estimation Starting from Axes in Adult Images

Ocular fundus images provide important information about retinal degeneration, which may be related to acute pathologies or to early signs of systemic diseases. An automatic and quantitative assessment of vessel morphological features, such as diameters and tortuosity, can improve the clinical diagnosis and evaluation of retinopathy.

This chapter provides the description of a method to accurately evaluate vessel diameters and centerline starting from the estimated network of vessel axes. The algorithm extracts points laying on the vessel borders by means of an efficient monodimensional matched filtering approach. The orientation of the filter kernel is chosen according to the information provided by the network and the appropriate scale is computed by means of an initial diameter estimation performed on the vessels cross section profiles before the filtering process.

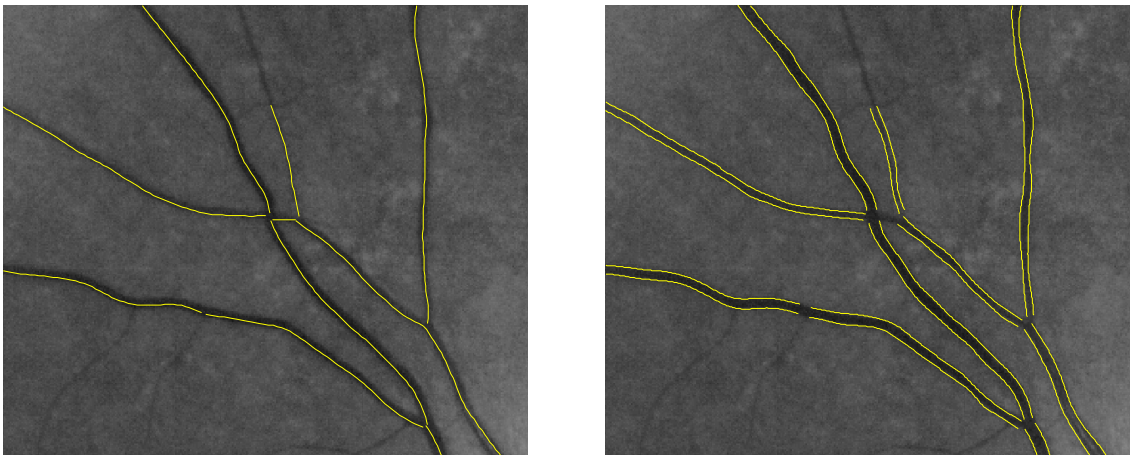

(a) (b)

Figure 5.1 (a) Starting network of vessel axes; (b) estimated calibers.

An adaptive correction step is then run to fix non consistent diameters, in order to obtain a regular and continuous vessel morphology. Vessel border refinement finally yields an accurate representation of the vascular structure.

Average calibers were evaluated, for a set of vessel segments, both manually by an expert and automatically by the proposed method. Comparative results show high correlation. In addition, starting from the structures assessed by the algorithm, for each processed image a binary mask has been drawn and compared with the manual segmentations available for the DB60, DRIVE, and STARE datasets.

5.1 Introduction

The morphology of the vascular structure can be affected by different abnormalities caused by acute pathologies or by early signs of certain systemic disease, such as diabetes and hypertension. Ocular fundus images can provide important information about these signs and their accurate analysis is necessary to improve clinical diagnosis of diseases. An automatic and quantitative assessment of vessel morphological features, such as diameters and tortuosity, can reveal important information on the abovementioned diseases. To this aim, the exact layout of all relevant vessels in the image must be extracted. A significant issue in fundus images is the contrast between vessel and background, which is often very poor, especially for capillaries. Digital noise represents another critical aspect and, in addition, wider vessels often present a bright reflex laying at the center (the central reflex), causing their profile to be indistinguishable from the one belonging to two narrow parallel vessels.

Matched filters have been widely used, both in their two-dimensional or monodimensional variant, to detect signals in presence of noise, because of the very high signal-to-noise ratio (SNR) they provide [63]. However, when applied to retinal image analysis, matched filtering requires precise knowledge of the blood vessel morphological parameters, such as thickness, orientation and shape profile, which substantially vary across the image. To circumvent this problem, multi-orientation and multi-scale approaches have been proposed: the vessel image is convolved with a set of variously oriented and scaled kernels, to get the best response.

The biggest drawback of this method is the computational time required to process the image with a high number of filters [64]. An approach proposed in literature to speed up the search for filter orientation is the use of steerable filters, such as Hessian filters [65], which exhibits as a major drawback the possible overfitting of noise and of nonvascular structures. A simple solution to the unknown thickness problem may be that of choosing some effective scale that works sufficiently well for most of the vessel widths. In this case however, small-scale filters might erroneously split a wide vessel into two narrower structures. On the other hand, large-scale filters perform poorly on narrow tubular structures and might merge narrow near vessels [62].

This chapter proposes a method to accurately evaluate vessel diameters and centerline starting from an even roughly estimated vessel axis network. Each segment of the network provides the approximate direction of a corresponding vessel axis. Starting from the assumption that cross section vessel profiles can be approximated by a

Gaussian shape [37], the algorithm extracts points laying on the vessel borders by means of an efficient matched filtering approach, using a discretized Laplacian of Gaussian (LOG) function as kernel. Appropriate kernel orientation and scale are preventively evaluated, in order to improve the filter precision and efficiency. A self-correcting step follows, where non-reliable border points are automatically fixed. To evaluate the performance of the method, we considered 739 vessel segments. For every segment, we compared the average caliber calculated by manual segmentation and by our algorithm.

5.2 Methods

The system that evaluates vessel diameters and centerline is composed of several modules. The first is the preprocessing-and-profile-extraction module (Sec. 5.2.1), which initially performs image enhancement [26]. Cross section vessel profiles P are then extracted along every branch of the vessel network orthogonally to the approximate axis direction.

They are then preprocessed with a mono-dimensional shift-invariant Gaussian filter, to reduce noise.

For each profile P, the edge-point-detection module (Sec. 5.2.2) carries out two tasks: a preliminary vessel width estimation is performed, which is used to set the kernel scale for the second step, consisting in a mono-dimensional matched filtering.

When a couple of candidate border points is detected for each profile, the adaptive-correction module (Sec. 5.2.3) checks their reliability. To this aim, a statistic index M is computed on the whole set of diameters of the considered vessel. Calibers that appear to be non-consistent with M are fixed by changing the matched filter scale, or forced to a trustworthy value when a reliable diameter cannot be found.

The border-refinement module (Sec. 5.2.4) is finally aimed to extract from the set of border points some regular curves delineating the final vessel edges.

In Figure 5.7 the output of the last three modules is displayed for a vessel segment where a significant central reflex is present, along with a crossing.

5.2.1 Preprocessing and Profile Extraction

The green component is extracted from the images, since it allows the best contrast for retinal vessels. An initial enhancement process is then applied to the whole image [26] with the aim of removing luminance and contrast drifts, to allow uniform intra- and inter-image contrast and luminosity. The intensities of the image are finally inverted so that the intensity of vessel pixels is higher, compared to the background.

In order to perform vessel segmentation we start from the previously estimated vessel network, whose branches approximate the axis direction for every vessel segment. Every segment s of the network can be expressed in curvilinear coordinates as a curve $C_s(i),\ i \in [1, \ldots, N_s]$. At every i in $[2, N_s - 1]$ we extract a profile P_i^s orthogonal to the direction of s and centered in $C_s(i)$. In order to limit digital noise, we build P_i^s as the mean of three adjacent profiles p_{i-1}^s, p_i^s and p_{i+1}^s orthogonal to s and centered respectively in $C_s(i-1)$, $C_s(i)$ and $C_s(i+1)$. The length of every profile p_k^s and hence of P_k^s, is fixed to a value large enough to contain the widest vessel cross section. Finally, to improve the profile SNR ratio, a mono-dimensional version of the shift-invariant Gaussian filter proposed in [66] is used. This version is a combination of domain and range filtering techniques for edge-preserving smoothing. From now on we will call PF_i^s the profile P_i^s after this shift-invariant Gaussian filtering.

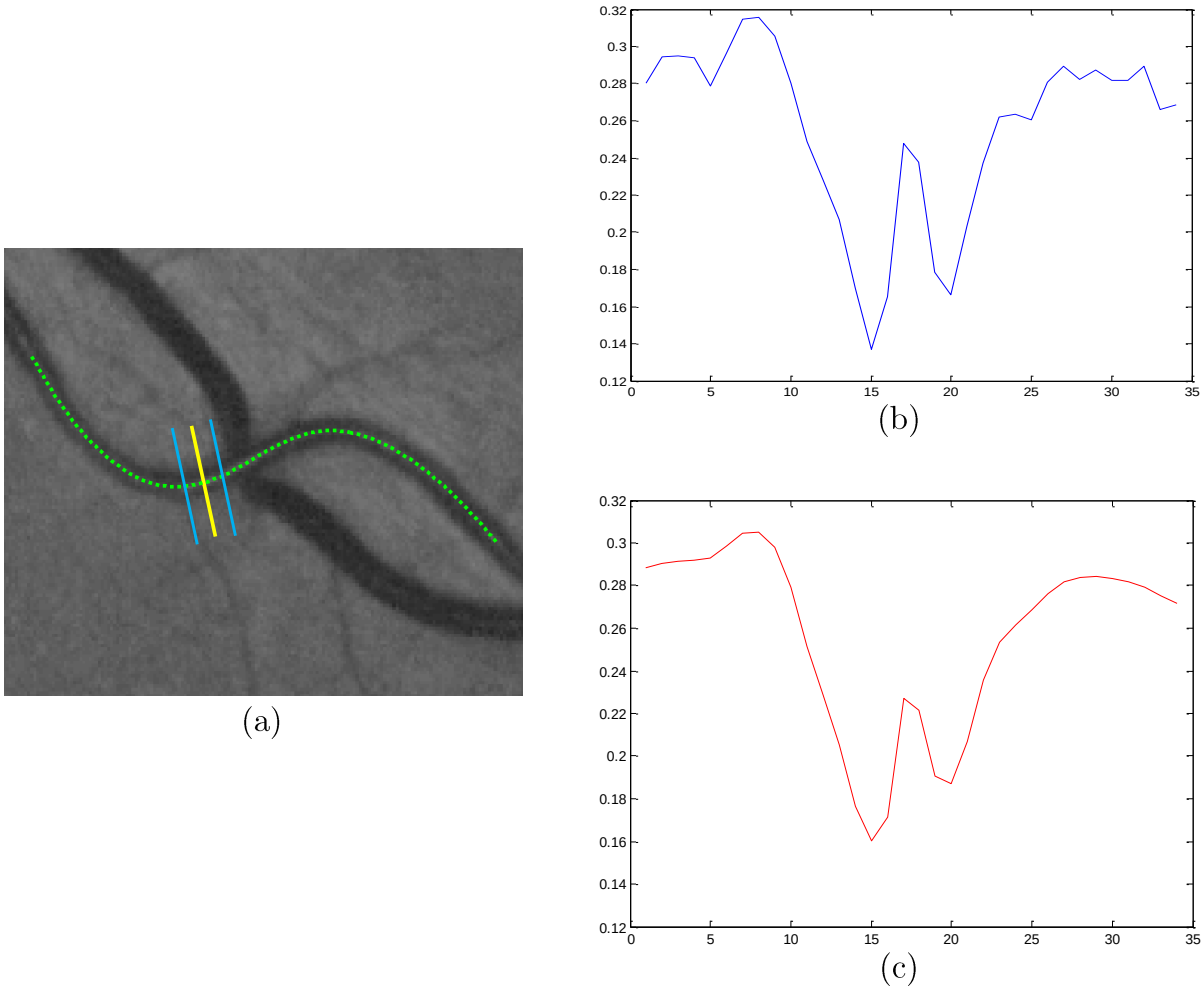

Figure 5.2 (a) Detail of an original image with the given vessel axis (green dots), the profile p_i^s of the current axis point $C_s(i)$ (yellow line), the two adjacent profiles p_{i-1}^s and p_{i+1}^s (blue lines); (b) mean P_i^s of the three profiles p_{i-1}^s, p_i^s and p_{i+1}^s; (c) The shift invariant Gaussian filtered profile PF_i^s.

5.2.2 Edge Point Detection

The task is aimed at extracting a couple of candidate border points for every profile PF_i^s obtained as described in Sec. 5.2.1.

The first step consists in estimating (even roughly) the caliber of the analyzed vessel. To this aim, the profile is initially processed with a high-pass filter to remove possible drifts at low frequencies. The diameter is then estimated starting from the maximum peak related to the center of the vessel and descending toward right and left valleys. At each iteration two points move away from the peak; the left point index li_k^s and a right one ri_k^s are determined where the slope markedly decreases with respect to its online average value.

If a central reflex is present, the vessel profile usually shows two peaks: one to the left and one to the right of the vessel centerline. In this case li_k^s and ri_k^s may stop on a valley related to the central reflex; therefore, the caliber estimation would not be correct. To overcome this problem, if the heights of li_k^s and ri_k^s are too different from each other, the highest point is moved toward the corresponding left or right terminal point of the profile, in order to reach a deeper valley.

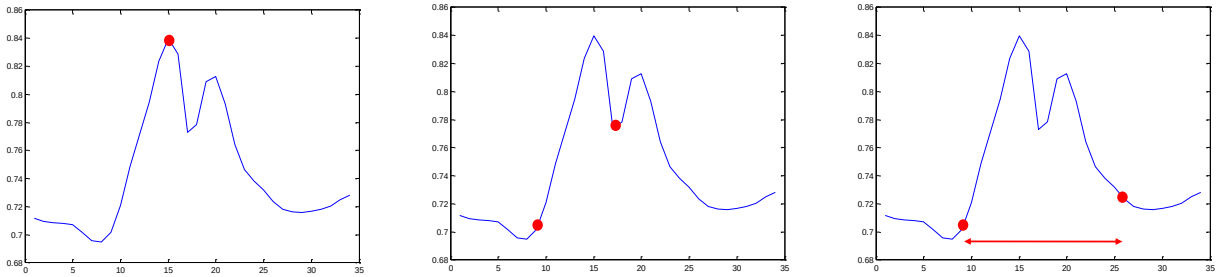

(a) (b) (c)

Figure 5.3 A profile PF_i^s processed for the diameter estimation. (a) The red dot indicates the maximum peak related to the center; (b) the two dots indicates where the slope markedly decreases by descending toward right and left valleys; (c) the rightmost point is moved to a deeper valley, whose height is comparable to the leftmost one.

Finally, the estimated caliber EC_k^s, centered on the k-th point of the s vessel segment, is given by the distance between li_k^s and ri_k^s.

Starting from this result, candidate border points are computed by filtering the profiles PF_k^s, with a mono-dimensional matched filter. The caliber estimated as described above is used to set the kernel scale. The matched filtering consists in the convolution between PF_k^s, and a kernel function $k_{EC_k^s}(x)$. We chose a discretized LOG function defined as:

$$k_{EC_k^s c}(x) = \begin{cases} -1, & 1 < x \leq EC_k^s \\ 2, & EC_k^s + 1 < x \leq 2EC_k^s \\ -1, & 2EC_k^s + 1 < x \leq 3EC_k^s \end{cases} \tag{5.1}$$

where EC_k^s is the previously estimated scale. The final filter response is given by:

$$PFM_k^s(x) = PF_k^s(x) \otimes k_{EC_k^s}(x) \tag{5.2}$$

where $\otimes$ is the operation of convolution. Since direction and scale are adaptively computed for every single analyzed profile, we increased the matched filter efficiency. We detect possible border points for the analyzed vessel by thresholding the filtered profile PFM_k^s. Taking cue from [39], we decided to determine the threshold with a fuzzy 2-means clustering method, which has been preferred to the Otsu's method because the first provided a more regular segmentation involving a smaller number of subsequent correction and forcing operations (see Sec. 5.2.3).

Fuzzy c-means (FCM) is a method of clustering which allows one piece of data to belong to two or more clusters [67]. This method is based on minimization of the following objective function:

$$J_m = \sum_{i=1}^{N} \sum_{j=1}^{C} u_{ij}^m \left\| x_i - c_j \right\|^2, \qquad 1 \leq m < \infty \tag{5.3}$$

where m is any real number greater than 1 (2 in our implementation), u_{ij} is the degree of membership of x_i in the cluster j (see Figure 5.4), x_i is the ith of d-dimensional measured data, c_j is the d-dimension center of the cluster, and $\|*\|$ is any norm expressing the similarity between any measured data and the center. Fuzzy partitioning is carried out through an iterative optimization of the objective function 5.3, with the update of membership u_{ij} and the cluster centers c_j by:

$$u_{ij} = \frac{1}{\sum_{k=1}^{C} \left(\frac{\|x_i - c_i\|}{\|x_i - c_k\|} \right)^{\frac{2}{m-1}}} \quad , \quad c_j = \frac{\sum_{i=1}^{N} u_{ij}^m x_i}{\sum_{i=1}^{N} u_{ij}^m} \tag{5.4}$$

This iteration will stop when $\max_{ij} \left\{ \left| u_{ij}^{(k+1)} - u_{ij}^{(k)} \right| \right\} < \varepsilon$, where ε is a termination criterion between 0 and 1, whereas k are the iteration steps. This procedure converges to a local minimum or a saddle point of J_m.

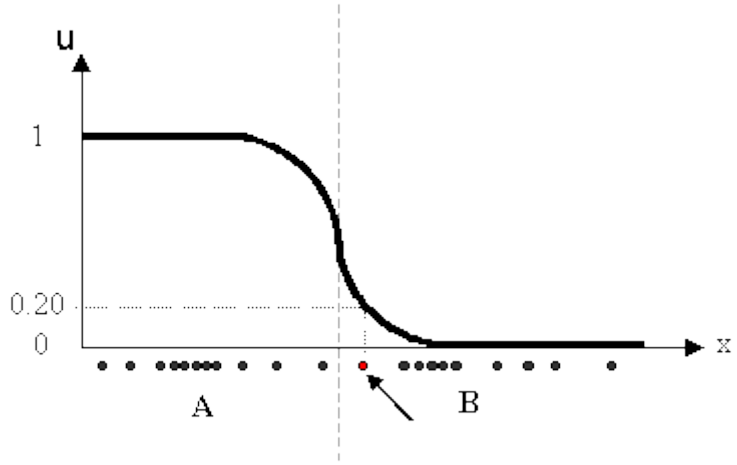

Figure 5.4 Given a certain mono-dimensional data set, suppose to represent it as distributed on an axis. Two clusters (A and B) may be identified in proximity of the two data concentrations. The datum shown as a red marked spot belongs more to the B cluster rather than the A cluster. The value 0.2 of u indicates the degree of membership to A for such datum.

In our implementation we defined two clusters, namely "vessel" and "non-vessel". The threshold value is the minimum x belonging to the "vessel" cluster. The value of m was set to 2, as it is usual in the literature. Using values closer to 1 would result in crisper (i.e. non-fuzzy) partitions, while values greater than 2 would increase the fuzziness of the membership. In order to speed the convergence of FCM, we initialized it with initial cluster centers at the first and at the third quartiles of the profile. Typically, one to three iterations of FCM were adequate.

When the thresholding operation provides multiple disjoint "vessel" segments (typical when two parallel vessels with similar caliber are close - less probable but possible when a vessel with strong central reflex is filtered with an underestimated scale) the edges are extracted by evaluating, among all "vessel" segments, the nearest to the center of the profile.

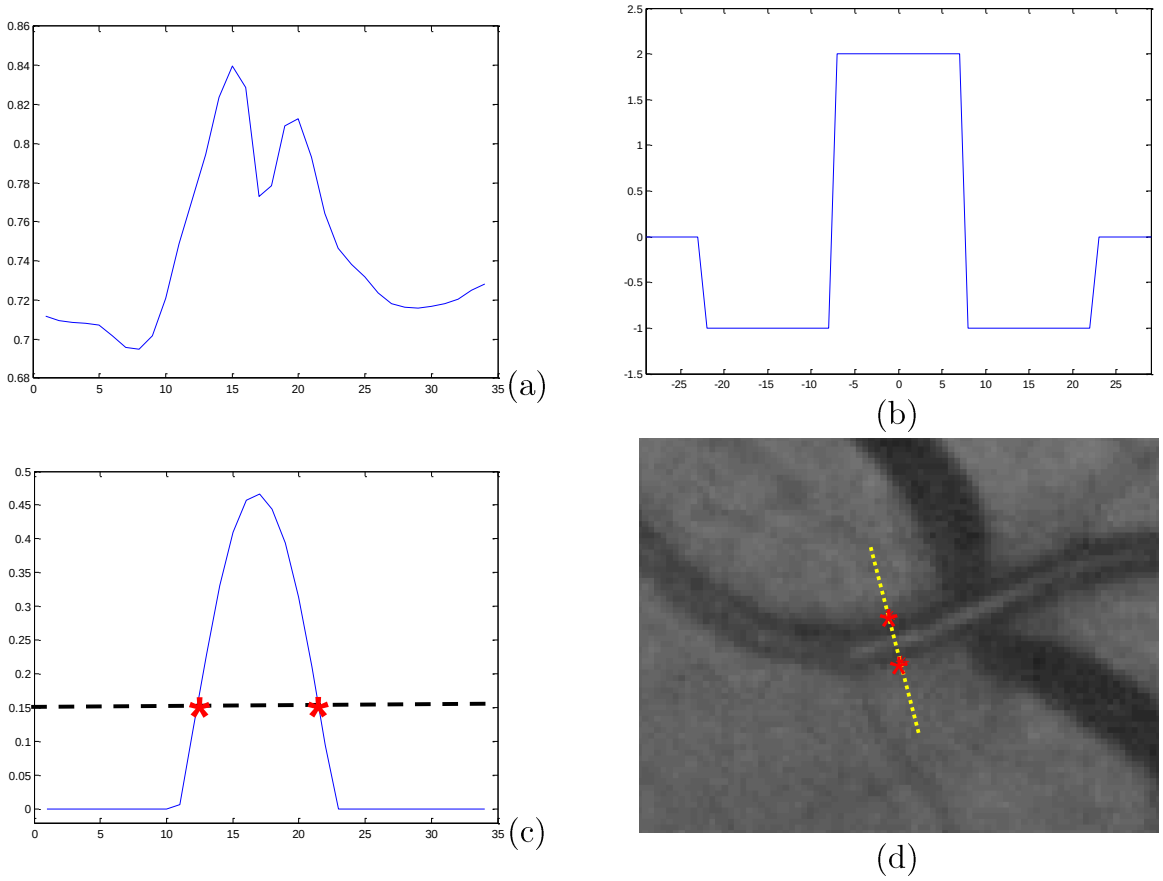

Figure 5.5 (a) The starting PF_i^s profile, (b) the kernel function $k_{EC_k^s}(x)$ centered in x=0 and with $EC_k^s = 15$ as estimated scale, and (c) the output of the matched filter, with the threshold (dashed black) chosen by using a fuzzy 2-mean clustering. The red stars represent the estimated caliber edges (c).

5.2.3 Adaptive Correction

As described in the previous sections, we processed vessel profiles averaged over three consecutive cross sections (Sec. 5.2.1), hence the analysis performed on vessels was almost local. The major drawback of this kind of approach is that it might fail in regions where vessels are not clearly detectable with respect to the background. For example, in fundus images there might be low-contrast regions, or areas where two vessels cross or run one very near the other (or are even partially overlapped) at some intervals. Also the presence of lesions, such as hemorrhages, could partially hide vessels. In these situations, the local caliber estimation might be imprecise, causing the matched filter to use an inaccurate scale, hence potentially yielding inexact vessel border locations.

To overcome this issue, every vessel segment s is now considered at a higher level as a tubular structure, whose calibers have to satisfy some continuity and regularity constraints. The adaptive correction module checks every pair of border points (ex-

tracted as described in Sec. 5.2.2) and compares their distance to a statistic index M_s computed on the whole set of diameters evaluated for s. If the checked diameter is considerably narrower than M_s the profile is reanalyzed with a matched filter using a larger scale (2 pixels larger); likewise, if the diameter is significantly wider than M_s the filtering is performed at a smaller scale (2 pixels smaller – the minimum and maximum scales taken into consideration are respectively of 1 and 25 pixels). We therefore use for every profile the most suitable single-scale filter, while using a multiple-scale filter only for critical profiles. In this way, we improve both the matched filtering precision and efficiency. One more case is taken into account in this module, when a reliable diameter cannot be found, even after scale adjustment. If the adjusted diameter is still considerably different from the statistic index M_s, border points are forced so that their distance match M_s itself. It should be noticed that this latter approach is taken for very critical situations only, when the transition pixels from the vessel to the background cannot be locally distinguished, even after scale adjustment.

The use of the median as M_s allowed us to achieve accurate results and, at the same time, to minimize the number of forced diameters.

The rationale of the adaptive correction module is represented in Figure 5.6.

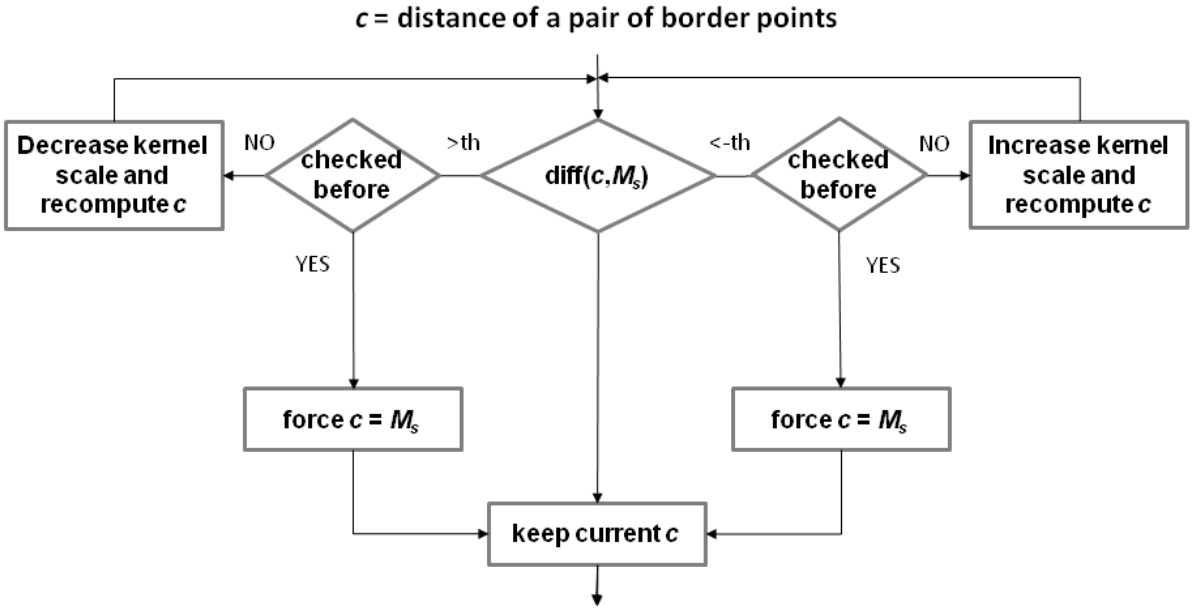

Figure 5.6 Schematic of the adaptive correction module applied to a pair of border points having distance c.

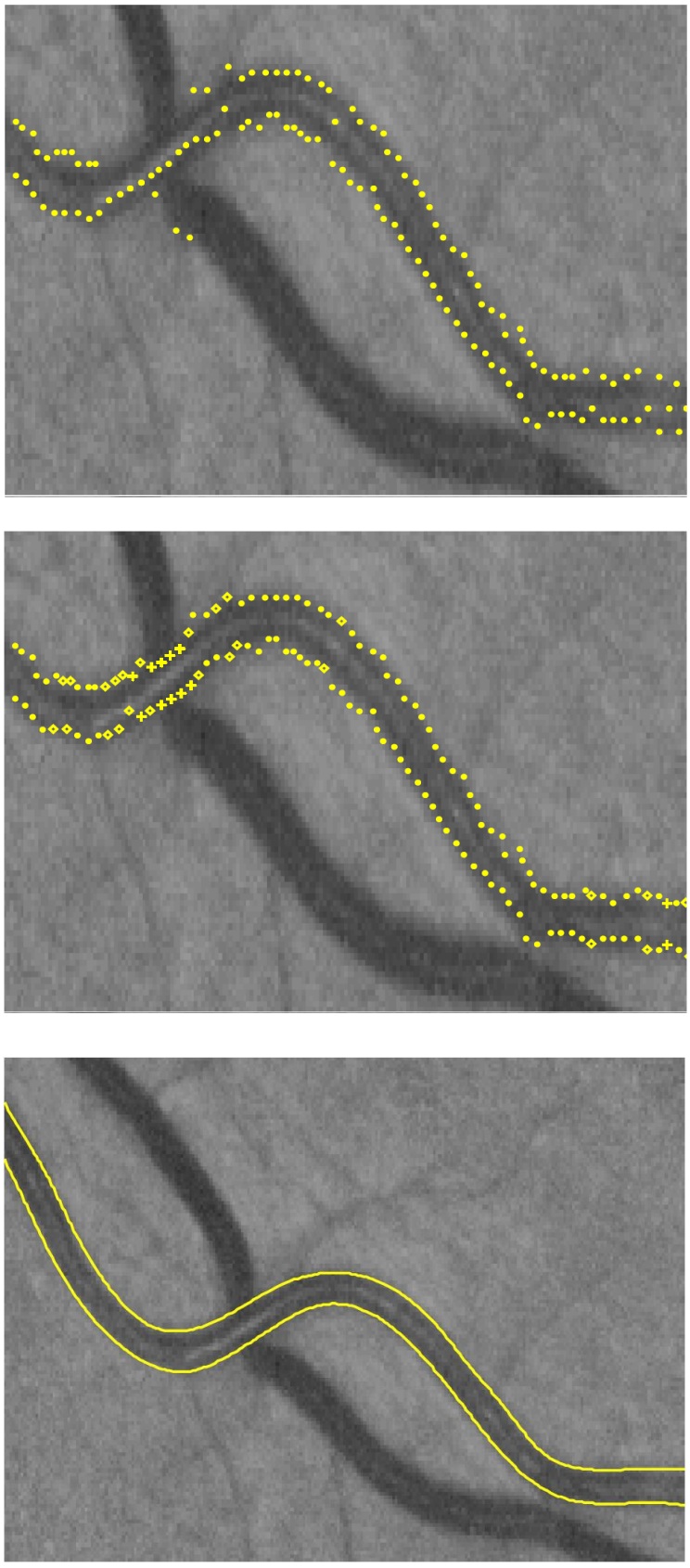

Figure 5.7 Border points evaluated before (top) and after (middle) diameter correction, along with the final vessel segmentation (bottom). In the middle image rhombus points were successfully corrected, while crosses were forced to the median caliber of the analyzed vessel segment.

5.2.4 Border Refinement

For each vessel segment s, the modules described in the previous sections provide two sets of points $B1^s = \{b1_i^s,\ i = 1{:}N_{b1}^s\}$ and $B2^s = \{B2_i^s, i = 1{:}N_{b2}^s\}$ sampling the two borders of the vessel. In some regions samples might be noisy or sparse, leading to an irregular border description.

Regularity of vessel borders was achieved by means of an interpolation function. The fact that vessels are continuous structures at least with their first derivative led us to use a cubic smoothing spline interpolation. Hence two final curves $C1^s(x)$ and $C2^s(x)$ laying on the vessel borders were computed. The vessel centerline $VC^s(x)$ is the curve computed by averaging $C1^s(x)$ and $C2^s(x)$ coordinates.

5.3 Results

5.3.1 Caliber Correlation

A set of 739 vessel segments, extracted from 3 color fundus images randomly chosen from the DB60 dataset was analyzed to test the method. Every segment considered is a portion of vessel whose extrema belong to two of the following regions: a natural vessel end point, a bifurcation, a branching, a cross. The considered vessels were also manually segmented by an expert ophthalmologist, and the chosen segments span a wide range of structures: from the very wide vessels departing from the optic disc to the thin peripheral capillaries.

Starting from the segments we obtained a vessel axis network by applying skeletonization to the binary image resulting from manual segmentation. We then ran the proposed method, to evaluate vessel diameters and centerline. The algorithm performance was assessed by computing the correlation between automatic and manual evaluation of the average caliber of the vessel segments. For the set of 739 vessel segments we obtained a correlation $\rho = 0.97$. In Figure 5.8 the scatter plot of the average caliber values, from manual vs. automatic evaluation, is shown.

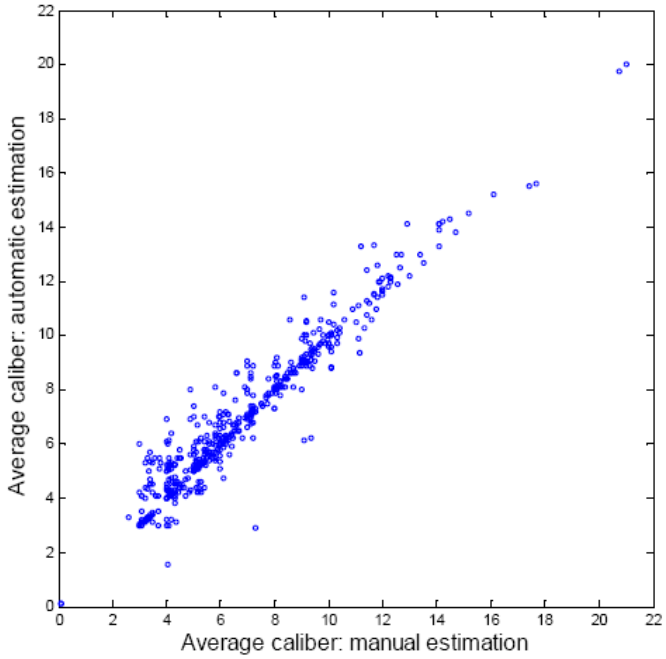

Figure 5.8 Average caliber: scatter plot of manual vs. automatic estimations.

The whole evaluation required a total of 17,032 profile analyses; 4,758 of them (27.9%) needed to be processed by the adaptive correction module, in order to find a reliable diameter after the first iteration. 2,653 diameters were effectively recovered (55.8% of the profiles processed by the adaptive correction module), while the remaining 2,105 were forced to the median caliber evaluated on the corresponding vessel segment.

5.3.2 Mask Comparison

The proposed system for the automatic tracking of the retinal vessel network was evaluated on DB60 dataset as well as the DRIVE and STARE databases. To perform the comparison with other retinal vessel segmentation algorithms, specificity, sensitivity and accuracy have been taken into consideration. Those three statistical measures assess the performance of a binary classification test. Sensitivity measures the proportion of vessel pixels that have been correctly identified as such, while specificity measures the proportion of background pixels that have been correctly identified. Accuracy is computed as the ratio of the number of correctly classified pixels (both vessel and non-vessel) over the total number of image pixels. The ground truth references for computing the performance measures was the manual segmentation result provided together with each database image. Table 5.1, 5.2, and 5.3 present the average accuracy, sensitivity and specificity calculated DB60 dataset, the DRIVE dataset, and the STARE dataset, respectively. In Table 5.2 and 5.3, performance of our method are also compared with the ones obtained by the authors who proposed the da-

tasets [17], [18] and with the performances obtained by a second human observer (the first human observer segmentation is the ground truth reference).

	Accuracy	Sensitivity	Specificity
Our method	96.18(0.54)	82.58	97.49

Table 5.1 Performance results of the proposed method on DB60 dataset

Method	Accuracy	Sensitivity	Specificity
2^{nd} human observer [17]	94.73(0.48)	77.61	97.25
Staal et al. [16]	94.42(0.65)	71.94	97.73
Niemeijer et al. [17]	94.17(0.65)	68.98	97.96
Our method	93.56(0.69)	73.04	96.62

Table 5.2 Performance results on the DRIVE dataset.

Method	Accuracy	Sensitivity	Specificity
2^{nd} human observer	93.54(1.71)	89.49	93.90
Hoover et al. [18]	92.67(0.99)	67.51	95.67
Staal et al. [16]	95.16(n.a.)	69.70	98.10
Our Method	94.01(1.60)	69.23	97.34

Table 5.3 Performance results on the STARE dataset.

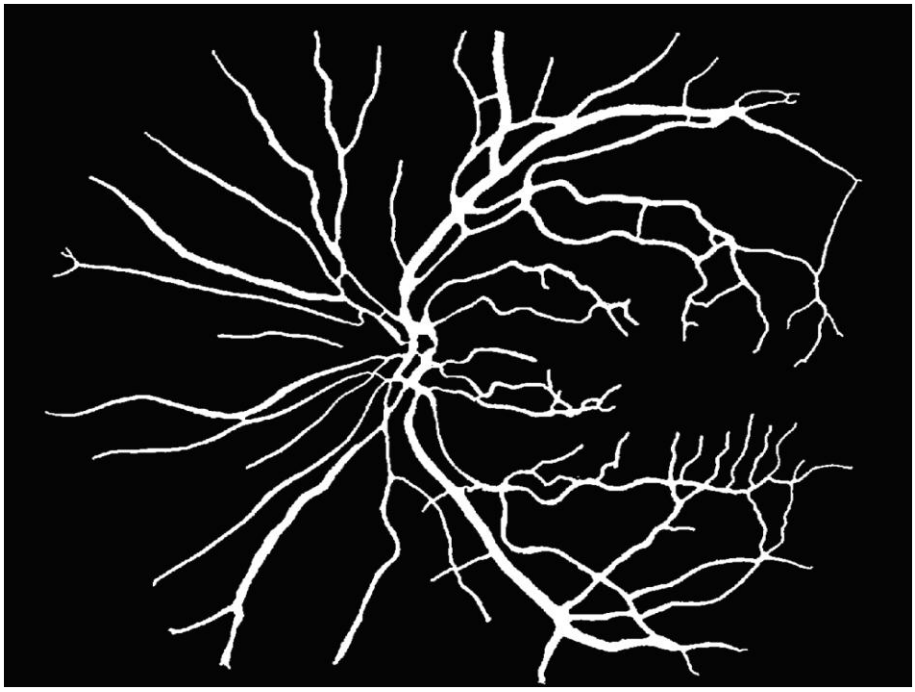

(a)

(b)

Figure 5.9 Example of segmentation result (DB60 dataset).

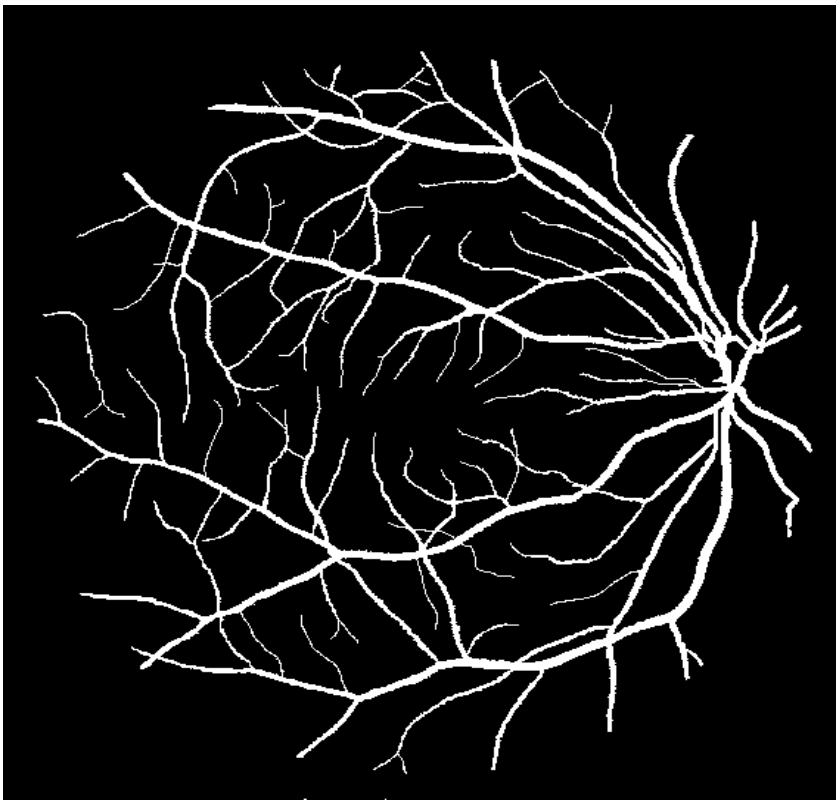

(a)

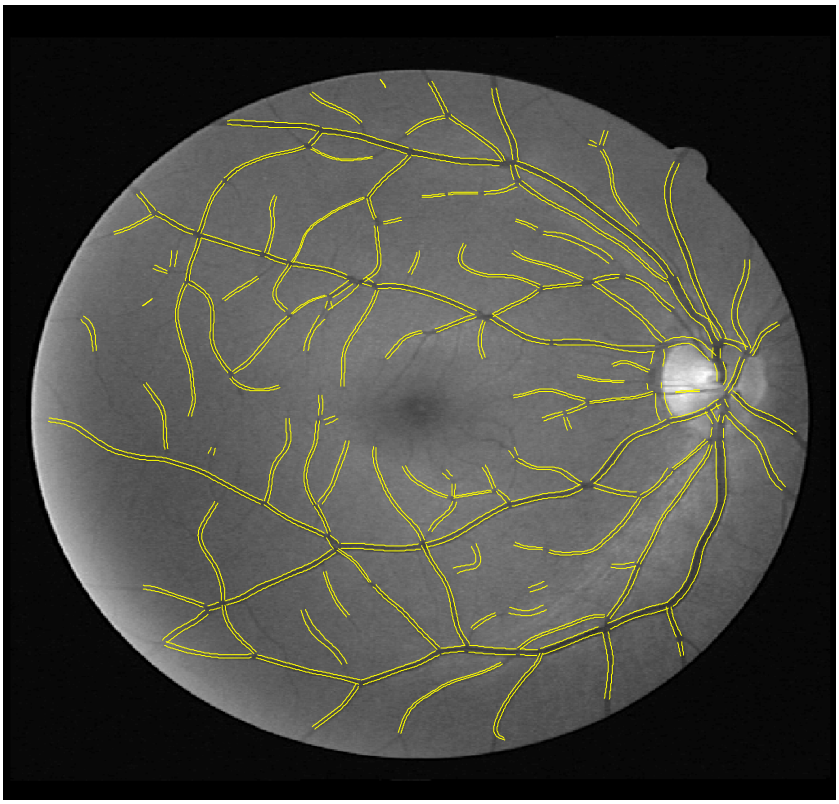

(b)

Figure 5.10 Example of segmentation result (DRIVE dataset).

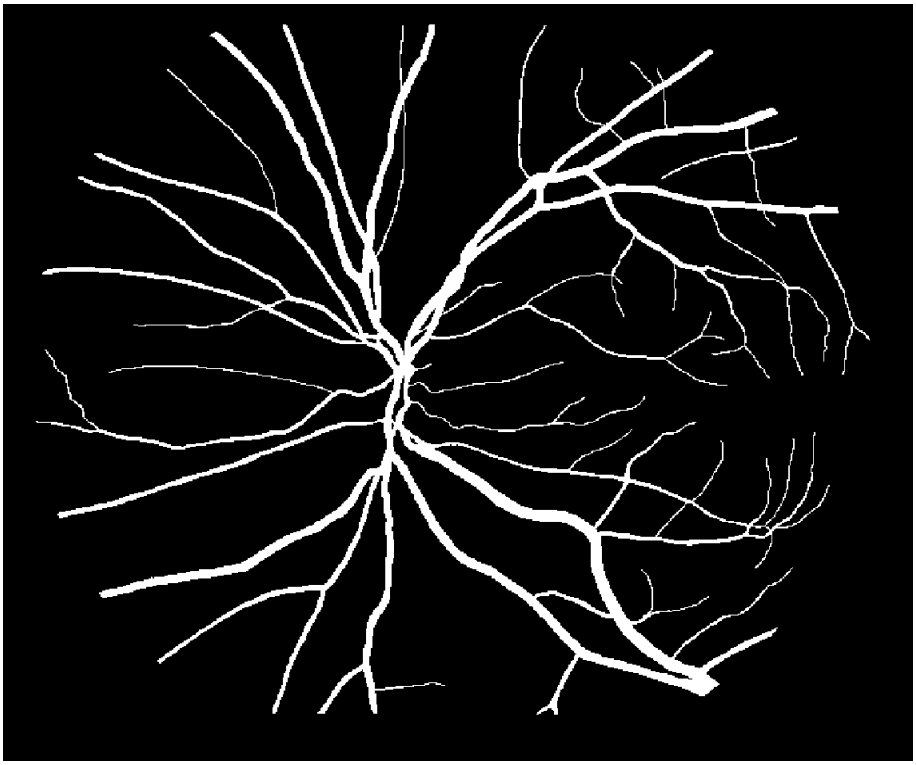

(a)

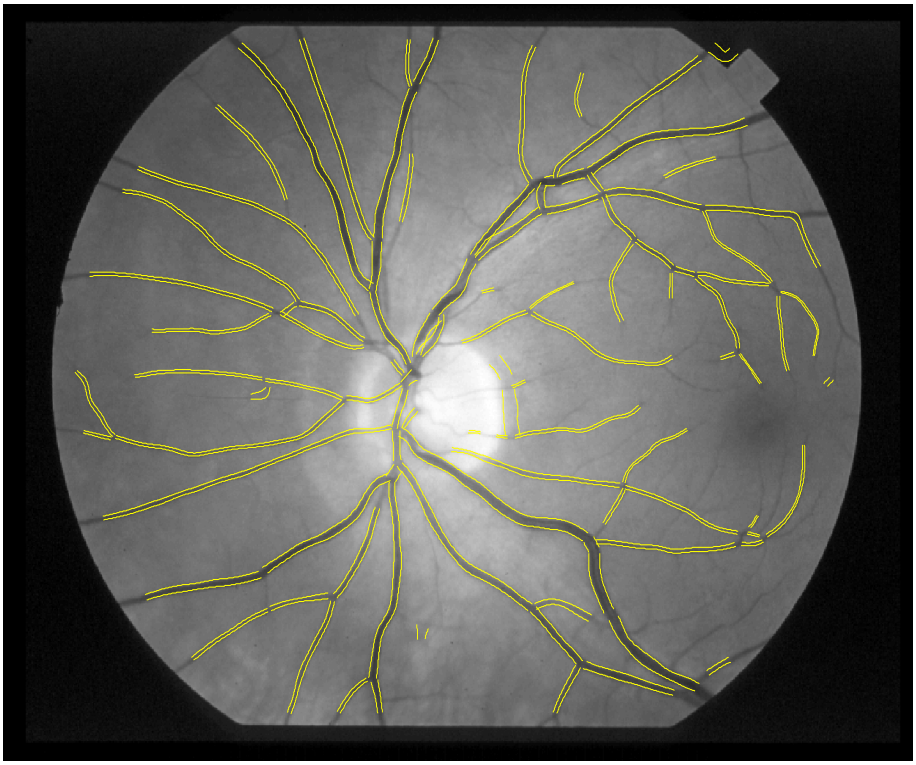

(b)

Figure 5.11 Example of segmentation result (STARE dataset).

As shown in tables, the mean accuracies of the method are different in the three datasets. As already mentioned in Sec. 4.4, this behavior depends on the different image features and the differences in the ground-truth manual labeling. Since the diameter detection step operates on the vessel axis network provided by the algorithm

described in Chapter 4, the results are somehow correlated with the sensitivity and the specificity of the latter. However, the comparison between manual and automatic masks takes into account the actual width of the tracked vessels, and not only the detection of their presence (axis). As a direct consequence, the results are affected more by the wider vessels than by the smaller ones. As far as the DB60 dataset is concerned, the vessel axis detection shows a sensitivity of 85.86, while in the mask comparison the sensitivity is 82.58. This could suggest that in such database the algorithm missed more wide vessels than capillaries. In the other two datasets, the results are opposite: we have 71.37 and 66.34 of axis detection sensitivity and 73.04 and 69.23 of vessel classification sensitivity, respectively, for the DRIVE and STARE dataset.

The comparison between the automatic binary classification and the manual labeling may not be the best method to evaluate the performance of the diameter estimation step (and that is why we assessed also the diameter correlation in Sec. 5.3.1). However, it enables the performance comparison among gold standard, second human references and the performance of other algorithms (Table 5.2 and Table 5.3). In the DRIVE dataset, our algorithm shows the worst accuracy and specificity (93.56 and 96.62), even if these measures are just ∼1% lower than the others. The sensitivity is ∼1-4% better than the other automated methods, while it is however lower than the 2nd human observer by ∼3.5%. In the STARE dataset, the performance of our algorithm is right in the middle of the other automatic method results; both accuracy and specificity, however, are slightly better than the ones obtained by the 2nd human observer.

5.4 Conclusion

This chapter describes the automatic system to extract vessel diameters from retinal images, by means of an efficient matched filtering approach. The rationale of the method consists in employing an edge detection approach that exploits the features provided by the vessel axis as prior information. Indeed, the subdivision of the segmentation process in two sequential and independent tasks has provided some saving in terms of computational load. Each point of the vessel axis is analyzed by coupling a matched technique both with the information of the vessel local direction and with a roughly estimated scale of the vessel diameter. Then, an adaptive correction step allows managing critical situations (presence of noise, lack of contrast, *etc...*) in which the algorithm may fail to detect the correct diameters.

It is worth noting that the method proposed in this chapter strongly depends on the quality of the initial axis network: if on one hand the vessel axis information provides a prior useful to fix the filter direction and keep low the number of used scales, on the other hand a fragmented network will lead to a fragmented segmentation of vessel segments. In this case, a linking procedure would be needed to reconstruct the

complete vascular tree. A module for false vessel detection that takes into account diameter information would be useful as well to discard possible recognized segments that do not represent real vessels.

In order to assess the performance of the method, we provided two different analyses: in the first one we computed the correlation between true diameters and estimated diameters in a set of highly accurate manual segmented vessels. 739 vessel segments were analyzed to test the system, and the results were compared to the labeling provided by a human expert. Calibers estimated with the proposed method are highly correlated with those measured on the manually segmented images ($\rho = 0.97$). In the second analysis we assessed accuracy, sensitivity, and specificity of the binary classification task by comparing the automatic segmentations of the vessel network with the ground truth ones, from three different datasets. Although performances slightly differ among the different datasets, overall the method provided accuracy, sensitivity, and specificity that are comparable to the ones obtained by the 2^{nd} human observers, as well as the ones obtained by other algorithms.

Chapter 6

AVRnet, a Software System for the AVR Estimation

The Arteriolar-to-Venular diameter Ratio (AVR), a parameter derived from vessel caliber measurements in a specific region of retinal images, is used as a descriptor of generalized arteriolar narrowing, an eye fundus sign often seen in patients affected by hypertensive or diabetic retinopathies.

The manual computation of the AVR is a tedious process, involving repeated measurements of the diameters of all arterioles and venules in the region by human graders. To facilitate large-scale clinical use, an accurate, rapid and efficient system to compute AVR is required. To this aim a web-based system, named AVRnet, was implemented. It is composed by a module for automatic vascular tracking, an interactive editing interface to correct errors and set the required parameters of analysis, and a module for the computation of clinical indexes. The system is based on the procedure developed by Tramontan et al. [21]: at first the vessel network has to be traced and their calibers estimated; then, in the region of interest for the estimation of the AVR, vessels are classified as either arteries or veins and the CRAE, CRVE, AVR parameters are computed.

AVRnet was organized as a client-server structure to allow clinicians and researchers from all over the world to work remotely with the system.

In order to assess the capability of our vessel tracking algorithm to provide useful information for the estimation of the mentioned clinical parameters just mentioned, we integrated it with the procedure described in [21].

The system has shown good performances in the 38 images of the UoW dataset (DCCT and ETDRS). The provided results have been compared with the measures obtained by the trained and proved personnel who have worked on the subject, resulting in a good correlation.

6.1 Introduction

An early detection of serious cardiovascular diseases can be provided by the analysis of microvasculature health status. The capillary network in the retina, an important example of such microvasculature, can be readily imaged and assessed using a normal fundus camera.

In retinal images, a sign that has proved to be related to cardiovascular diseases is the generalized arteriolar narrowing, usually expressed by the Arteriolar-to-Venular diameter Ratio (AVR). The AVR is computed from the CRAE (Central Retinal Artery Equivalent) and CRVE (Central Retinal Venular Equivalent) values. These in turn are derived from the individual arteriolar and venular calibers, which are measured in a standard area (ROI) centered on the optic disc (OD) and from half-disc to one disc diameter from the OD margin [23]. The Knudtson formulas to calculate the AVR parameter take into account only the six largest arteries and the six largest veins inside the described ROI [68]. The manual procedure requires the long and cumbersome measurement of the required vessel calibers (more than 15 minutes per image on average). For this reason the AVR parameter is not commonly utilized in a clinical context and difficulties are present also in a research context, because of the lack of a fast, precise and accurate tool. To overcome this problem, computer-assisted procedures have been proposed ([69], [70]), which require some degree of user assistance. IVAN is the most popular software used for this purpose, but the time for the analysis of a single image is about 20 minutes, too long to allows its use it in screening studies or to become a standard in clinical practice [23]. Moreover, IVAN needs well trained graders, because some operations have to be manually performed: correcting vessel traced profiles and classifying vessels in arteries and veins. In addition, this tool has not been conceived to be used in a telemedicine context.

In this chapter we present a fast and accurate semi-automatic system that requires minimal manual intervention. An additional benefit of the proposed system is that it is designed as a client-server application: a client program interacts with a centralized server application allowing to choose images, perform vascular tracking, manually set parameters, and compute clinical indexes (AVR, CRAE, CRVE). In particular, clinicians and researchers interested in the measurement or validation of clinical indexes will be able to work remotely with the system through an internet connection. Additional advantages are the possibility of exploiting multiple processors for parallel operations, the availability in any operating system, and the centralized software upgrade.

6.2 Methods

The procedure to derive the AVR index requires several steps to be performed. The network of retinal vessel is traced using the method described in Chapter 4 and Chapter 5, while the OD position and diameter have been manually identified. With this information, the specific area in which caliber measurements have to be done is identified. Inside this area, vessels are labeled as either arteries or veins and their calibers are measured. In order to ensure the highest reproducibility for the assessment of the parameters of interest [68], the six arteries and the six veins with highest caliber among all the tracked vessels are selected and considered along their length until

a bifurcation occurs. Finally, caliber measurements are used to compute AVR, according to the formula proposed in [68]. Other than the algorithm for the vascular tracking, the proposed system is composed by three modules:

1) a main application interface that acts as external wrapper for the whole system. This allows the user to choose the images to be analyzed, to launch the automatic vessel tracking module, to activate the interactive editing interface (see point 2) and to set up the results saving.
2) an interactive editing interface, which allows the user to set the required parameters of analysis, highlights critical situations, and, when necessary, helps in the correction process;
3) the analysis algorithm, which takes into account the settings entered by the user and, according to the vascular tracking information, computes the clinical parameters.

The system was organized as a client-server structure.

6.2.1 Main Application Interface

When the application is launched the main interface, divided in two panels, is shown. The leftmost panel includes commands to choose images from the file system and add them to (or remove them from) the list that will be processed with the vascular tracking algorithm. The rightmost panel includes a list of files relative to images that were previously processed with the tracking algorithm. The user can choose a file from the list and launch the interactive editing interface in order to set up the analysis and extract the clinical parameters. The main interface is represented in Figure 6.1.

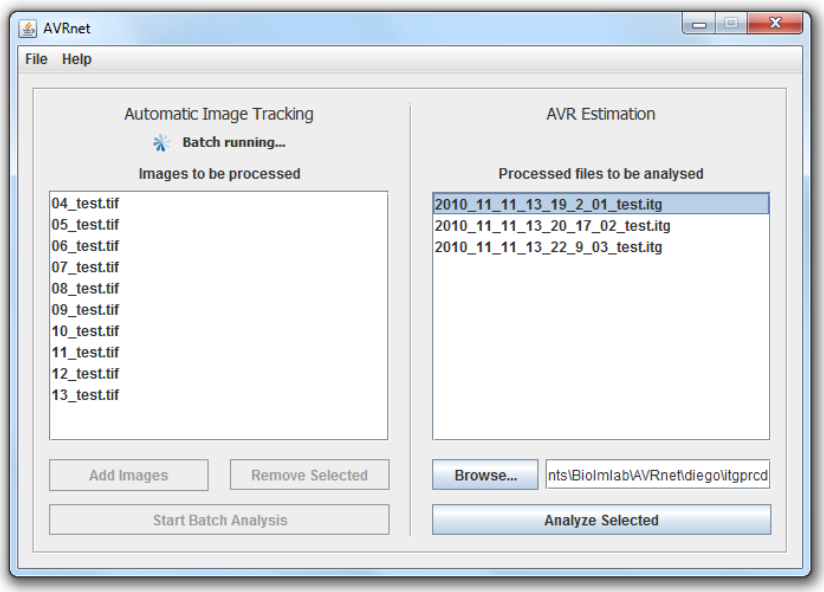

Figure 6.1 The AVRnet main application interface.

6.2.2 Interactive Editing Interface

The proposed system interacts with the user by means of the interface shown in Figure 6.2 and Figure 6.3. It is composed by two panels. The first contains editing commands and a display where useful information is shown (e.g. solutions proposed by the system, helping information, results). The second shows the entire image or zoomed parts of it.

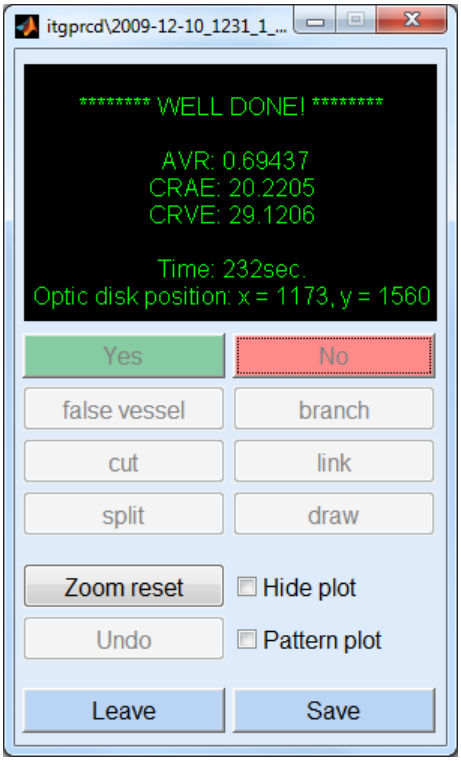

Figure 6.2 The first panel of the interactive editing interface. This includes editing commands and a display where useful information is shown.

The interface was designed according to the following rationale:

1) to highlight critical situations (e.g. tracking errors);
2) to propose possible solutions;
3) to limit the number of user operations;
4) to allow fast and easy operation;
5) to allow editing any result.

The image display panel shows only vessels that do not cross completely the ROI widthways, i.e. short vessels either not connected to other ones (and therefore probable false vessels) or vessels with tracking errors. Short vessels could also be branches at a bifurcation: this situation is recognized and proposed to the user, who may confirm it or not. To correct tracking errors, the user can edit the results just by clicking on the appropriate command: to eliminate a false vessel, to cut an erroneously

tracked part of vessel, to split a vessel in two, or to link one vessel to another. Eventually, the user can even trace, with the aid of a custom tool, the vessel borders themselves.

After the guided correction step, the entire image is displayed and the user can select the erroneously tracked vessels that have not been corrected yet, simply by clicking on them. In the final step the user can add those vessels that were not tracked at all by the automatic procedure.

In the final step, the artery/vein classification is performed. The technique used for the classification is described in the next paragraph. The classification result is shown on the display panel, where arteries are shown in green and veins in yellow. If necessary, the user can modify the class of a vessel by simply clicking on it.

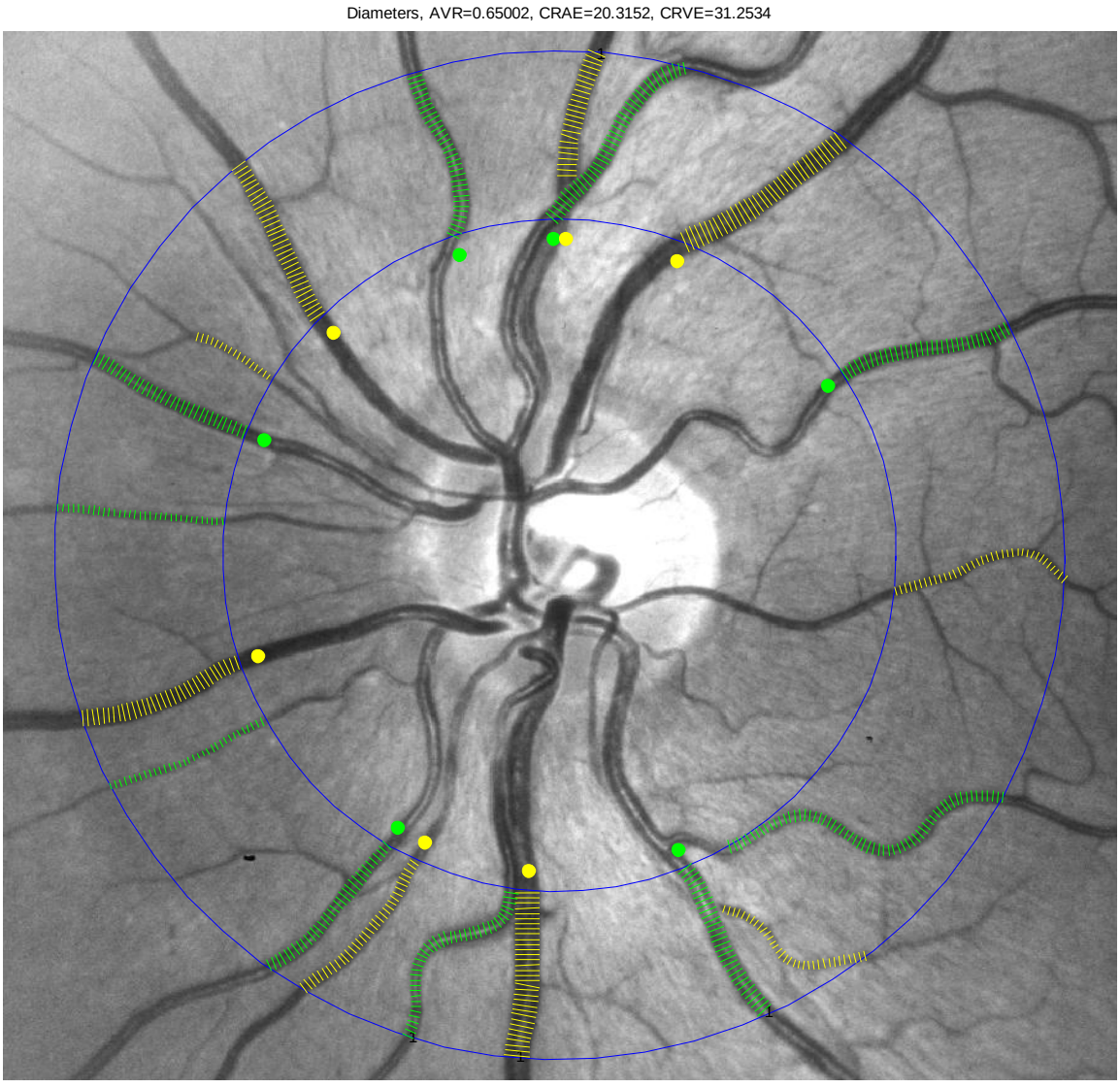

Figure 6.3 The image panel shows the estimated vessel diameters for all the tracked vessels in the area of interest. The 6+6 vessels used for the actual computation of parameters are labeled with small circles (green or yellow to identify arteries or veins).

6.2.3 Artery/Vein Discrimination

As arteriolar and venular calibers need to be separately measured to derive the AVR, each tracked vessel inside the ROI must be correctly labeled as being either an artery or a vein. For this classification the red contrast is used, a parameter related to the central reflex, which is more evident in arteries than in veins, and from it the probability of the vessel to belong to the "vein" class is derived (the probability of belonging to the "artery" class is one minus the probability of belonging to the "vein" class).

All the vessels whose probability of belonging to one of the two classes is less than 0.8 (and then more than 0.2 for the opposite class), and that have a diameter greater than 45 μm, are considered "uncertain" and are consequently submitted to the user, who confirms or rejects the proposed classification.

6.2.4 AVR Estimation

From the caliber estimated by our algorithm (Chapter 5) and the classification provided by the method described above, the Central Retinal Artery Equivalent (CRAE) and the Central Retinal Vein Equivalent (CRVE) parameters can be computed, together with the AVR parameter

$$AVR = \frac{CRAE}{CRVE} \tag{10.1}$$

which provides a useful clinical measure as an indicator of generalized arteriolar narrowing [23], [68].

The system displays results and the final image (with colored veins and arteries) on the screen. At the same time the computed clinical indexes are automatically saved in an text file and images are stored in a local folder.

6.2.5 Client-Server System Architecture

The system was implemented as a client-server application (Figure 6.4). The encrypted communication between the client-side programs and the server-side software is obtained by interfacing JAVA and PHP technologies. When the application starts, the user is required to authenticate, in order to enable a connection with a server (located at the Department of Information Engineering, at the University of Padova) and to setup data storage. For every user authenticated, a PHP session is created on the server, with unique identification number for each visitor and the storage of va-

riables is based on this ID. This allows to safely managing multiple simultaneous accesses. The user can select one or more retinal images from the local drivers, by means of a JAVA graphical user interface that navigates the local file system: no constrain on image resolution, format or acquisition source is present. Images are sequentially sent to the server, where they are stored and analyzed by a fully automatic vascular tracking procedure. After the vessel tracking on each image is completed, the server sends a message to the client, including a secure link to the address where tracking results were stored and the client program automatically proceeds to download the files to the user machine.

A second intuitive interface is installed on the client machine, which allows the user to manually check and correct the vessel tracking results (see Sec. 6.2.2), in order to obtain final clinical parameters estimation. This process does not need interaction with the server.

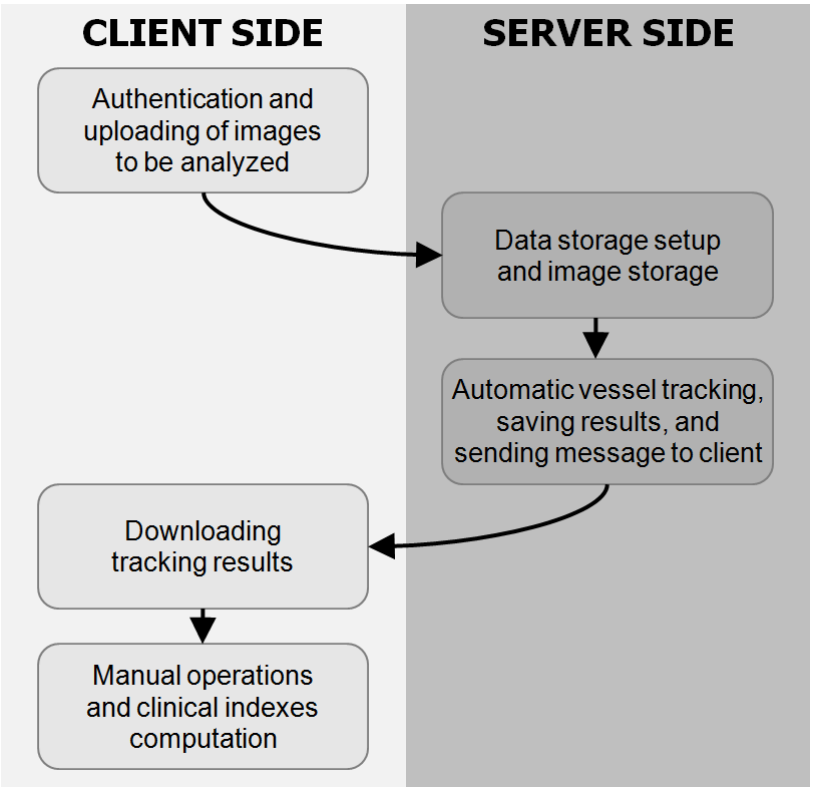

Figure 6.4 The client-server architecture of the software application for the AVR estimation.

6.3 Results

The methodologies described in this chapter have been tested in two stages: the first focused on the reliability of the tracking results while the second focused on the efficiency of the whole process to assess the AVR parameters.

In the first analysis (Sec. 6.3.1), in order to attain the best assessment as regards the usability of the tracking algorithm, the graders were asked to edit the tracking results only if major vessels were not identified. The user interaction session had to focus on speed and the tracking imperfections (such as diameter under- or over-estimations) were ignored. As far as artery/vein classification correction is concerned, no correction limitation was enforced. The results have been compared with the measures obtained by the trained personnel from the University of Wisconsin (UoW).

In a second analysis (Sec. 6.3.2), the graders were allowed to edit the tracking results at their will: in this case the human interaction session focused on providing the best vessel segmentation, resulting in a more time-consuming process than the previous above mentioned. The correlations among UoW grading and the results obtained by three graders who used our proposed framework have been computed, in order to assess the measure repeatability of the whole system. Moreover, the inter- and intra-grader analysis agreement was evaluated on the King's College dataset.

6.3.1 Limited Intervention Setup

The reference values against which the computer estimations have been compared were performed by the experts at the Department of Ophthalmology & Visual Sciences, University of Wisconsin-Madison. As regards the ETDRS images, they supplied us with the ARV parameters, while the DCCT set was accompanied with the AVR, CRAE, and CRVE evaluations.

Table 6.1 reports the reference and the estimated CRAE, CRVE and AVR values, for the 20 images composing the DCCT set. Their scatter plot with the corresponding correlation is shown in Figure 6.5, Figure 6.6, and Figure 6.7.

Table 6.2 reports the reference and the estimated AVR values, for the 18 images of the ETDRS set. Their scatter plot with the corresponding correlation is shown in Figure 6.8.

DCCT Image	ground truth CRAE	estimated CRAE	ground truth CRVE	estimated CRVE	ground truth AVR	estimated AVR
1	158.16	145.76	238.23	235.69	0.66	0.62
2	144.23	142.34	248.19	241.22	0.58	0.59
3	146.59	147.64	248.83	242.09	0.59	0.60
4	136.41	128.16	250.87	251.02	0.54	0.51
5	161.00	148.01	243.81	236.01	0.66	0.63
6	161.35	147.38	217.40	208.91	0.74	0.71
7	156.03	139.00	202.00	195.05	0.77	0.71
8	156.03	151.42	216.86	223.36	0.72	0.68
9	145.20	143.44	197.64	197.96	0.73	0.72
10	124.58	126.79	176.45	177.86	0.71	0.71
11	151.32	141.67	199.98	198.03	0.76	0.71
12	171.73	156.38	226.80	228.69	0.76	0.68
13	164.98	169.99	256.76	248.28	0.64	0.68
14	160.37	157.37	218.49	228.51	0.73	0.69
15	137.19	134.41	208.64	204.42	0.66	0.66
16	179.24	170.54	241.75	229.25	0.74	0.74
17	176.88	170.19	254.35	256.55	0.70	0.66
18	156.88	152.23	238.43	227.04	0.66	0.67
19	155.48	154.69	189.28	184.55	0.82	0.84
20	147.48	144.58	246.64	248.50	0.60	0.58

Table 6.1 For each of the 20 DCCT images, both the reference and the estimated CRAE, CRVE, and AVR values are listed.

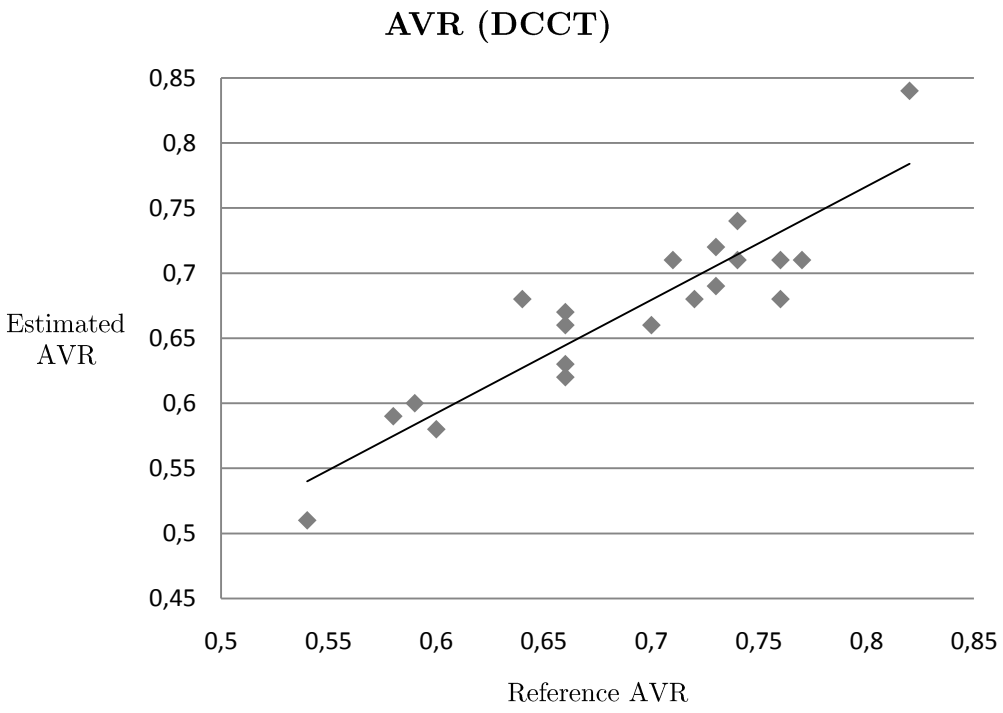

Figure 6.5 Scatter plot of the reference and estimated AVR values.

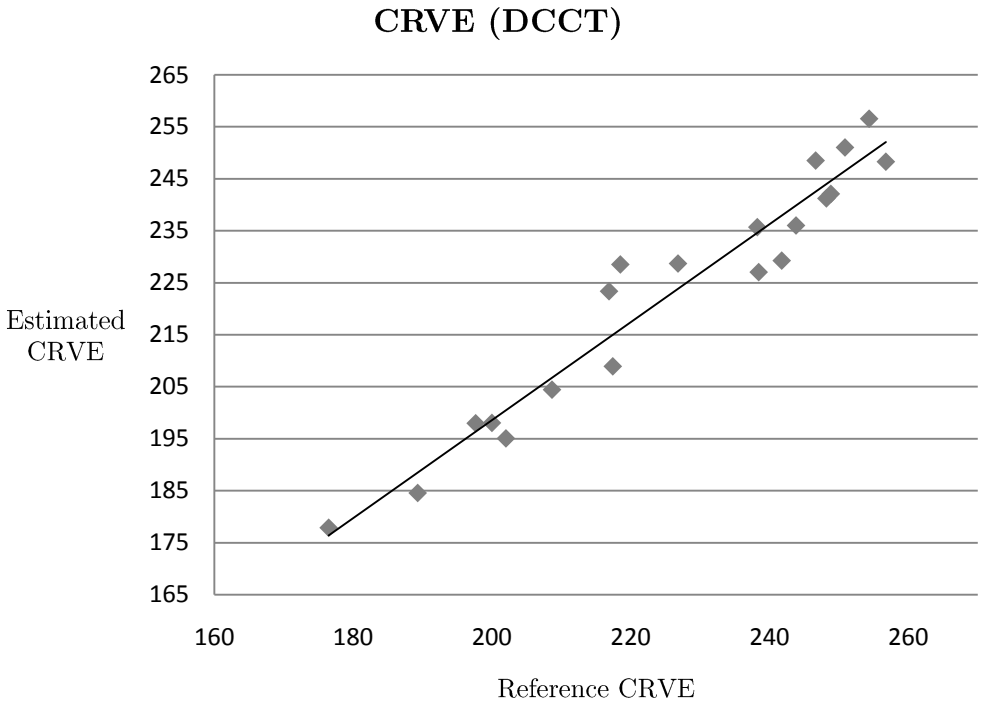

Figure 6.6 Scatter plot of the reference and estimated CRVE values.

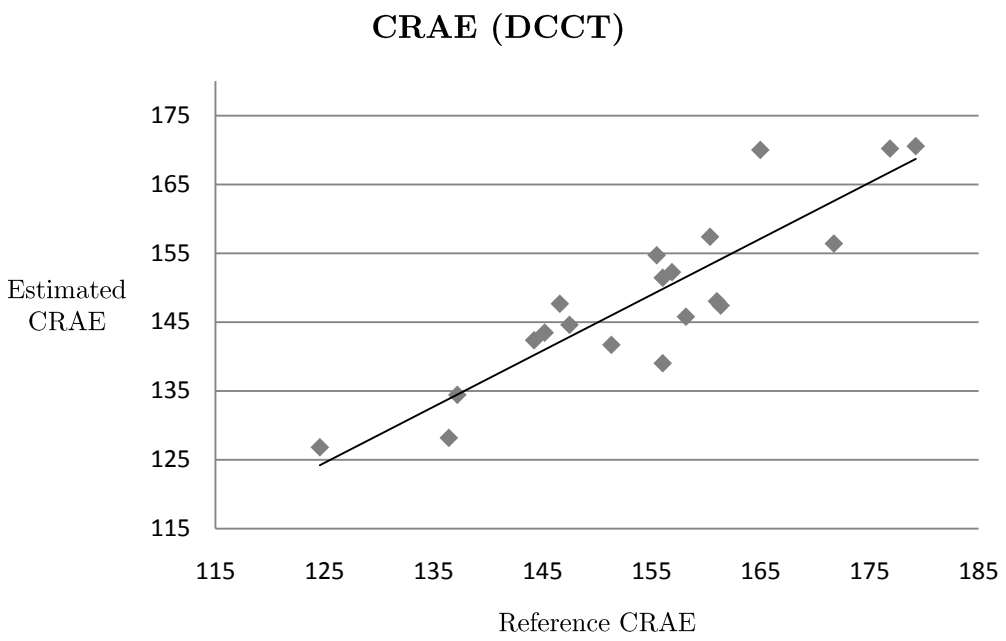

Figure 6.7 Scatter plot of the reference and estimated CRAE values.

Image	ground truth AVR	estimated AVR
1	0.64	0.67
2	0.51	0.55
3	0.68	0.65
4	0.71	0.72
5	0.82	0.85
6	0.71	0.71
7	0.69	0.71
8	0.53	0.52
9	0.60	0.62
10	0.66	0.64
11	0.71	0.72
12	0.55	0.58
13	0.74	0.67
14	0.45	0.52
15	0.60	0.61
16	0.64	0.65
17	0.54	0.53
18	0.75	0.76

Table 6.2 For each of the 18 ETDRS images, both the reference and the estimated AVR value are listed.

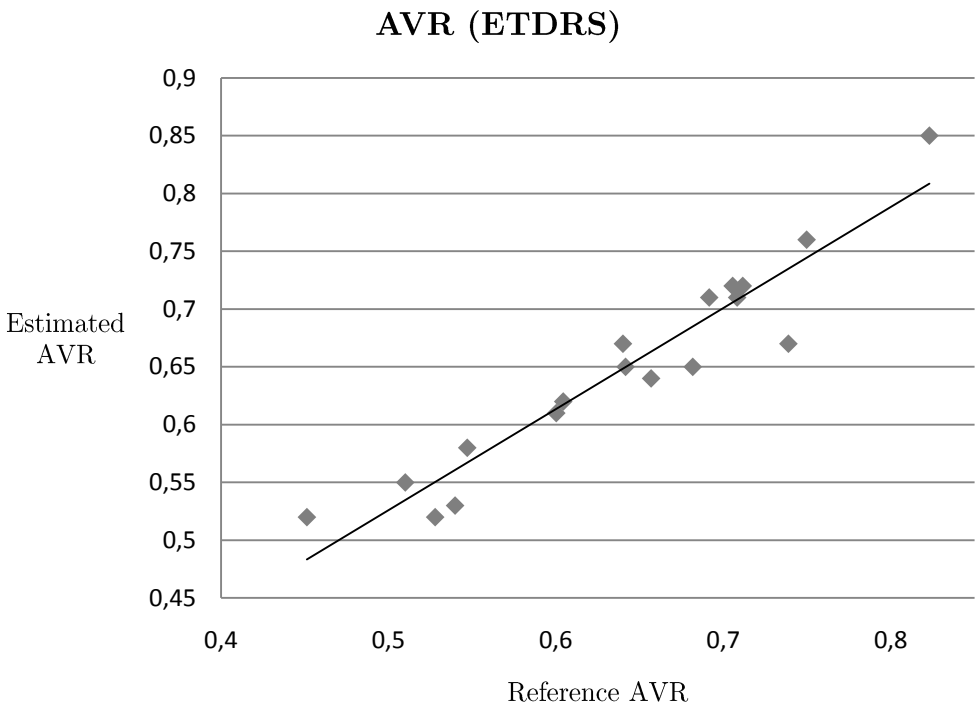

Figure 6.8 Scatter plot of the reference and estimated AVR values.

The AVR values estimated by the computer procedure are quite close to the ones provided by the manual one.

The average running time of the Matlab® prototype on a Pentium-M PC (1.8 GHz, 1 GB of RAM) was about 60 seconds for the vessel tracking procedure and 90 seconds for the whole procedure of ROI selection, tracking correction, artery/vein classification, and AVR estimation. The time is about six times shorter than the average time needed for a manual estimation of the AVR (roughly 15 minutes vs. 150 seconds).

This achievement, combined to good correlation attained, suggests the possible application of the system to the AVR parameter estimation for clinical diagnostic purposes.

6.3.2 Full Intervention Setup

In this second analysis, we have relaxed the tracking correction constraints, so that the three graders (A, B, and C) could freely edit the vessel tracking mistakes, with the aim of providing the best possible vessel segmentation.

We compared the correlation among the UoW grading and the results obtained by the three graders on the DCCT dataset.

Table 6.3 reports the CRAE, CRVE and AVR values assessed by the UoW grader as well as the three graders A, B, and C, for the 20 images of the DCCT dataset. At the bottom of Table 6.3, the correlations among the four graders are provided.

DCCT image	CRAE				CRVE				AVR			
	UoW	**Grader A**	**Grader B**	**Grader C**	**UoW**	**Grader A**	**Grader B**	**Grader C**	**UoW**	**Grader A**	**Grader B**	**Grader C**
1	158.16	137.96	143.91	145.36	238.23	230.06	230.6	236.59	0.66	0.60	0.62	0.61
2	144.23	138.86	138.30	137.3	248.19	240.29	230.58	248.96	0.58	0.58	0.59	0.55
3	146.59	142.69	149.91	146.66	248.83	244.65	245.89	253.8	0.59	0.58	0.59	0.57
4	136.41	122.32	123.49	130.45	250.87	243.38	241.42	250.18	0.54	0.50	0.51	0.52
5	161.00	148.04	142.38	149.44	243.81	234.68	229.72	240.78	0.66	0.63	0.62	0.62
6	161.35	149.54	151.03	150.73	217.40	208.76	218.27	216.58	0.74	0.72	0.69	0.7
7	156.03	138.49	135.43	137.51	202.00	198.46	194.78	195.56	0.77	0.70	0.69	0.7
8	156.03	153.11	156.36	151.08	216.86	214.46	215.63	213.43	0.72	0.71	0.72	0.71
9	145.20	143.15	145.27	142.88	197.64	198.61	198.54	198.21	0.73	0.72	0.73	0.72
10	124.58	128.12	125.80	128.58	176.45	179.45	178.79	179.45	0.71	0.71	0.70	0.72
11	151.32	143.00	137.52	138.25	199.98	200.91	198.68	201.32	0.76	0.71	0.69	0.69
12	171.73	144.26	149.34	158.18	226.80	221.63	221.52	236.57	0.76	0.65	0.67	0.67
13	164.98	158.06	161.84	165.14	256.76	242.82	254.76	258.79	0.64	0.65	0.64	0.64
14	160.37	156.09	154.70	153.90	218.49	218.63	226.60	219.50	0.73	0.71	0.68	0.70
15	137.19	133.70	128.13	127.47	207.00	205.22	206.31	206.89	0.66	0.65	0.62	0.62
16	179.24	162.87	163.43	163.95	241.75	241.29	239.54	243.10	0.74	0.67	0.68	0.67
17	176.88	167.63	169.68	171.64	254.35	250.61	256.04	254.90	0.70	0.67	0.66	0.67
18	156.88	148.37	152.27	148.37	238.43	234.84	233.65	224.61	0.66	0.63	0.65	0.66
19	155.48	149.85	150.27	150.24	189.28	186.64	183.53	181.64	0.82	0.80	0.82	0.83
20	147.48	137.78	136.75	137.16	246.64	244.63	240.93	249.19	0.60	0.56	0.57	0.55

CORRELATIONS

	Grader A	**Grader B**	**Grader C**
UoW	0.85	0.84	0.91

	Grader A	**Grader B**	**Grader C**
UoW	0.99	0.97	0.98

	Grader A	**Grader B**	**Grader C**
UoW	0.92	0.91	0.92

	Grader A	**Grader B**	**Grader C**
Grader A	1.00	0.96	0.92
Grader B	0.96	1.00	0.96
Grader C	0.92	0.96	1.00

	Grader A	**Grader B**	**Grader C**
Grader A	1.00	0.97	0.98
Grader B	0.97	1.00	0.96
Grader C	0.98	0.96	1.00

	Grader A	**Grader B**	**Grader C**
Grader A	1.00	0.97	0.97
Grader B	0.97	1.00	0.98
Grader C	0.97	0.98	1.00

Table 6.3 CRAE, CRVE and AVR values assessed by the UoW, A, B, and C, graders for the DCCT dataset. At the bottom, the correlations among the four graders are provided.

The overall repeatability between users and with respect to the UoW grading was assessed by the correlation coefficients. The correlation ranges between UoW grading and the non-qualified users in our group are 0.85-0.91 for CRAE, 0.97-0.99 for CRVE, and 0.91-0.92 for AVR. The correlation ranges between the each pair of users are 0.92-0.96 for CRAE, 0.96-0.98 for CRVE, and 0.97-0.98 for AVR.

A second test was performed in order to assess the reproducibility of the measures provided by the system: three graders independently graded each of the 29 images of

the King's College dataset. On a subset of 10 images randomly chosen from the 29 each grader performed the analysis twice minding to avoid analyzing the same image consecutively (in order to prevent memory effects on the results). Pearson's correlation coefficient was computed between each pair of graders and for the grade and re-grade analysis of each grader in order to evaluate the inter- and intra-grader agreement respectively (Table 6.4).

CORRELATIONS

	CRAE			CRVE				AVR			
	Grader A	**Grader B**	**Grader C**		**Grader A**	**Grader B**	**Grader C**		**Grader A**	**Grader B**	**Grader C**
	grade	grade	grade		grade	grade	grade		grade	grade	grade
re-grade	0.97	0.95	0.98	re-grade	0.99	0.98	0.99	re-grade	0.96	0.96	0.99

	Grader A	**Grader B**	**Grader C**		**Grader A**	**Grader B**	**Grader C**		**Grader A**	**Grader B**	**Grader C**
Grader A	1.00	0.84	0.85	**Grader A**	1.00	0.85	0.83	**Grader A**	1.00	0.87	0.84
Grader B	0.84	1.00	0.80	**Grader B**	0.85	1.00	0.86	**Grader B**	0.87	1.00	0.86
Grader C	0.85	0.80	1.00	**Grader C**	0.83	0.86	1.00	**Grader C**	0.84	0.86	1.00

Table 6.4 CRAE, CRVE and AVR values assessed by the A, B, and C, graders for the King's College dataset. At the top the intra-grader correlations are provided, while at the bottom the inter-grader correlations for each pair of users are displayed.

The correlation ranges for the intra-grader agreement are 0.95-0.98 for CRAE, 0.98-0.99 for CRVE, and 0.96-0.99 for AVR. The correlation ranges between each pair of users (inter-grader agreement) are 0.80-0.85 for CRAE, 0.83-0.86 for CRVE, and 0.84-0.87 for AVR.

For all the tests, the total time required to analyze one image was on average 5 min (range: 2-8 minutes).

6.4 Conclusion

The results shown in Sec. 6.3.1 and 6.3.2 allow concluding that the proposed computerized system can be reliably used to quantitatively assess the vascular parameters in retinal images from normal, hypertensive or diabetic subjects. It will allow clinicians to recover the quantitative estimation of these parameters in an objective, fast and user-friendly way.

The first, totally automated phase performs image luminosity equalization and contrast enhancement, tracing of the vascular network with vessel caliber estimation, vessel classification as either arteries or veins. In the second phase, the user evaluates the results provided and confirms them or applies the necessary corrections via a user-friendly editing interface, which is capable of detecting the critical situations to be

presented to the user for expert assistance. The vascular parameters are eventually computed.

An additional benefit of the proposed system is the possibility of using it simply through an internet connection: clinicians and researchers interested in the measurement or validation of clinical indexes will be able to work remotely with the system, and assessments will be possible even without the presence of physicians at the care center unit. At present, a beta version of the system is hosted at the website http://bioimlab.dei.unipd.it; it is under beta testing and will be soon publicly available.

Accuracy and repeatability of the complete system were assessed by analyzing the images kindly provided by the Dept. of Ophthalmology and Visual Sciences, University of Wisconsin, USA, and by the Department of Twin Research & Genetic Epidemiology, of the King's College London Division of Genetics and Molecular Medicine, St Thomas' Hospital, UK.

Chapter 7

Vessel tracking for small FOV Infant Images

Many retinal diseases are characterized by changes to retinal vessels. A common condition associated with retinopathy of prematurity (ROP) is the increase of vascular dilation and tortuosity.

In 1949 Owens [71] reported that retinal venous dilatation and arteriolar tortuosity were indicators of ROP. Two decades later Baum [72] reported that "the earliest detectable ophthalmoscopic signs of oxygen toxicity to the retina are considered to be tortuosity and dilatation of the retinal vessels." Such vascular changes were included in several of the earlier classification schemes of acute phase ROP [73], [74], [75]. Saunders et al. [76] observed that if the posterior pole vasculature was normal (that is, no venous congestion or increased arteriolar tortuosity) then there was less than 3% probability of there being ROP stage 3 or above [77]. In 1995 Capowski et al [78] reported arterial tortuosity to be a useful measure of ROP disease state, while Wallace et al [79] and Freedman [80] demonstrated that vessel diameter and tortuosity could be used to indicate the risk that ROP would progress to requiring treatment. There is a need to identify and quantify signs of plus disease as early as possible before ROP has progressed to the point where outcome is compromised. The earliest signs of plus disease are venous engorgement and increased arteriolar tortuosity around the optic disc.

The growing use of digital imaging in ophthalmology has led to substantial developments in the field of computer assisted analysis of retinal vessel morphology. Computer algorithms have now the potential to achieve high levels of accuracy and objectivity in the quantitative measurement of retinal vascular parameters such as diameter, branching patterns, and tortuosity.

Images acquired from newborn babies usually differ in appearance from those of the adult in a number of aspects. Due to the lack of clarity of the eye media and the technical difficulty of obtaining images from a preterm baby, images taken from a baby's eye are low-contrast, noisy, and sometimes blurred. Moreover the relative absence of choroidal pigmentation leaves the choroidal circulation clearly visible. These aspects cause problems and are an obstacle to the identification of vessels. Algorithms that have been successfully applied for adult retinal images usually do not work effectively enough within these limitations.

A new semi-automatic vessel tracking system for Nidek NM200D infant images is proposed. The method requires the user to manually select the vessels to be analyzed

by placing some points on them. A cubic spline interpolates the points and approximately identifies the vessel centerlines. The algorithm performs a tracking of the vascular structure and computes its local and average width and the tortuosity.

7.1 Introduction

Retinopathy of Prematurity was already described in Sec. 2.6. In this chapter specific techniques for the analysis of images acquired with Nidek NM200D (Nidek Co., Gamagori, Japan) fundus camera from premature babies at risk of ROP are broaden.

7.1.1 Nidek NM200D Fundus Camera

The Nidek NM200D is a portable non-mydriatic and non-contact fundus camera (Figure 7.1) designed for retinal image acquisition on both adult and preterm born infants. It has a CCD sensor able to acquire 1.5 megapixels images at a 30 degrees field of view. The main features of the Nidek NM200D are the following:

- It has a compact lightweight body that makes it portable.
- It is a cheap solution with respect to other more complex fundus cameras.
- It provides a user friendly and comfortable usability, that makes it manageable from both ophthalmologists and non ophthalmologist trained operators.
- It provides a non-contact and non-mydriatic image acquisition and thus sedation is not required when scanning infants retina.
- The narrow field of view limits the acquisition of the premature infants retina to the vascularized area, excluding the periphery. The 30 degrees FOV coupled with the mid resolution sensor provides images where vessels appear as relatively large structures with respect to other common fundus cameras having larger FOV and higher resolution.

7.1.2 Existing Methods

Many systems for computer aided diagnosis (CAD) have been recently developed to accurately measure and quantify retinal vascular dilation and tortuosity in premature infant images. Analysis on the retinal images are usually based on

Figure 7.1 The Nidek NM200D portable fundus camera.

segmentation and tracking methods aimed at extracting the vascular network over the image background.

For example, Heneghan et al. [47] presented a segmentation method based on the analysis of the second derivative properties of vasculature, coupled with some pre- and post- morphological processing. In a more recent work, Sukkaew et al. [82] proposed a method to automatically extract the vessel structures based on a statistically optimized LOG filter followed by thresholding and morphological techniques.

Unfortunately, fully automated techniques used for analysis in adult retinal images show low efficiency when applied to images acquired from infants: the difficult illumination through small pupils, the cloudy media and the strong evidence of choroidal vessels are some of the several aspects limiting the quality of images analyzed for ROP. In response to these difficulties, a number of semi-automated methods have been proposed for the analysis of preterm retina. They all require the user to limit the region of interest (ROI) for the analysis around the optic disc and to manually edit, delete or add some vessel after the first automatic tracking step. After this manual intervention, some method is used to evaluate tortuosity and width of selected vascular structures.

Martinez-Perez et al. [83] developed a semi-automatic method for blood vessel segmentation based on the scale space analysis of the first and second derivative of the intensity image. Wilson et al. [84] proposed a semi-automatic ROP analysis technique that identifies the retinal vessels by using filtered detection measurements based on maximum likelihood estimation of vessel parameters from an image. A third system for the analysis of preterm retinas was developed by Wallace et al. [85]. It performs segmentation of the selected vessels by means of a bidirectional ridge/valley traversal technique.

All the methods proposed in literature for preterm retina images have provided interesting results, yet none has shown to be free of weak points and outperform all the others.

7.2 Methods

This section presents a semi-automatic technique to perform vessel tracking and to quantitatively assess vascular tortuosity and width. Vessels to be analyzed are selected by manually drawing an approximate centreline laying inside them. Starting from this *a priori* information, vessel axis and edges are detected using the constraint that vessels present a tubular structure delimited by two parallel borders. After image enhancement, all vessel edge points are extracted by means of a Canny filter. Refined axis and calibers along the vessel are then identified by appropriately linking pairs of points on opposite edges. From tracking results, vessel calibers and a tortuosity index are computed.

7.2.1 Image Preprocessing

As a first step, the green channel is extracted from the original RGB retinal image, since this provides the best quality and highest contrast for vessel structures over the background. A vessel segment is manually chosen by the user and some points are placed inside the segment. These points are automatically interpolated with a cubic spline approximating the course of the vessel axis, as shown in Figure 7.2 (a). A region of interest (ROI) is extracted around the selected vessel and all the subsequent processing will be limited to the ROI in order to reduce the computing time. Initially the image is filtered with a two dimensional bilateral filter [66], which is a combination of domain and range filtering technique for edge preserving smoothing. Given an image $I(\boldsymbol{x})$ the filter response $O(\boldsymbol{x})$ is given by

$$O(\boldsymbol{x}) = k^{-1}(\boldsymbol{x}) \int_{-\infty}^{\infty} \int_{-\infty}^{\infty} I(\boldsymbol{\xi}) c(\boldsymbol{\xi}, \boldsymbol{x}) r\big(I(\boldsymbol{\xi}), I(\boldsymbol{x})\big) d\boldsymbol{\xi} \tag{7.1}$$

where k is a normalization term defined as:

$$k(\boldsymbol{x}) = \int_{-\infty}^{\infty} \int_{-\infty}^{\infty} c(\boldsymbol{\xi}, \boldsymbol{x}) r(I(\boldsymbol{\xi}), I(\boldsymbol{x})) d\boldsymbol{\xi} \tag{7.2}$$

$c(\boldsymbol{\xi}, \boldsymbol{x})$ is a closeness function between pixels defined as:

$$c(\boldsymbol{\xi}, \boldsymbol{x}) = e^{-0.5\left(\frac{\xi - x}{\sigma_d}\right)^2}, \tag{7.3}$$

$r\big(I(\boldsymbol{\xi}), I(\boldsymbol{x})\big)$ is the similarity function between pixels value defined as:

$$r\big(I(\boldsymbol{\xi}), I(\boldsymbol{x})\big) = e^{-0.5\left(\frac{I(\xi) - I(x)}{\sigma_r}\right)^2}. \tag{7.4}$$

The geometric spread σ_d in the domain is chosen according to the desired amount of low-pass filtering. The larger σ_d the more the blurring effect, since values from more distant profile locations are combined. Similarly, the photometric spread σ_r in the profile range is set to achieve the desired amount of combination of pixel values. Pixels with values much closer to each other than σ_r are mixed together and values much more distant than σ_r are not. For this specific application, we empirically set $\sigma_d = 5$ and $\sigma_r = 0.05$.

The adopted edge preserving smoothing technique reduces the noise and the gray level artifacts inside the analyzed vessel and in the background, making the vessel border extraction method described in the following section more robust.

7.2.2 Vessel Border Extraction

A set C of candidate edge points is provided by an edge detector algorithm based on the Canny technique [86]. C usually includes points belonging to the borders of the selected vessel, plus points belonging to the borders of other vessels present in the ROI and points originating from noise or artefacts: the main purpose of the proposed method is to identify two subsets, $BPR \subset C$ and $BPL \subset C$, of points that lay on the two true edges of the selected vessel.

C is split into two subsets, L and R, including points that lay on opposite sides with respect to the vessel axis. An estimation ϱ_E of the average width for the selected vessel is computed by averaging the distance between points in L and R that are placed in a neighbourhood of the initial centerline.

The axis is divided into np parts along its length and the vessel is analyzed by processing them in parallel. By iterating along the np axis segments, couples of border points $bpl \in L$ and $bpr \in R$ are searched inside two opposite circular regions NHB_l and NHB_r respectively. The center of NHB_l and NHB_r is distant $0.5*\varrho_E$ from the centerline and their radius is initially set to a value of $0.3*\varrho_E$. When multiple points are present inside a circular region, the one showing the strongest response to the Canny filter is chosen.

After the generic j-th iteration, the average vessel width (ϱ_{AVG}) is updated by averaging the distance between the j pairs of border points bpl and bpr:

$$\rho_{AVG} = \frac{1}{j}\sum_{i=1}^{j} d(bpl_i, bpr_i) \tag{7.5}$$

where $d(a, b)$ represents the Euclidean distance between two points a and b.

After the first np iterations, the initial value ϱ_E used as distance for the centers of the circular regions NHB_l and NHB_r is replaced with ϱ_{AVG} and their radius is replaced with $0.3*\varrho_{AVG}$. This tends to favour a regular description of the vessel borders, penalizing the selection of anomalous calibers given by wrong pairs of border points. According to experimental results the parameter np was set to 4 because this value lim-

its the number of unreliable diameters estimated that need a fixing post processing step (see Sec. 7.2.2.1). An example of border points extracted is shown in Figure 7.2 (b-c).

7.2.2.1 Correction of Unreliable Diameters

In some critical region along the vessel (i.e. low contrast areas, or regions where two vessels cross), borders might not be visible and the selected *bpl* and *bpr* might not be placed over the vessel edges. The average width ϱ_{AVG} is used as basis of comparison to accept or reject border points: if

$$|d(bpl, bpr) - \rho_{AVG}| < t * \rho_{AVG} \tag{7.6}$$

then the points are accepted, otherwise two more reliable points are searched after widening the regions of search NHB_l and NHB_r. The parameter t was empirically set to 0.25. If borders are not visible and a reliable couple of border points cannot be found, two points *bpl* and *bpr* are created so that their distance matches exactly ϱ_{AVG} and the corresponding centerline position is estimated by averaging the centreline position of the adjacent reliable diameters. The border points after the diameter correction are shown in Figure 7.2 (d).

7.2.2.2 Vessel Border Regularization

For the selected vessel segment, the described steps provide two sets of points $BPR = \{bpr_i,\ i = 1{:}N_{bpr}\}$ and $BPL = \{bpl_i,\ i = 1{:}N_{bpl}\}$ sampling the two borders of the vessel. In some regions samples might be noisy or sparse, leading to an irregular border description. Regularity of vessel borders was achieved by means of an interpolation function. The fact that vessels are continuous structures at least with their first derivative led us to use a cubic smoothing spline interpolation. Hence two final curves *CR* and *CL* laying on the vessel borders were computed. The initial manually drawn vessel centerline is now updated with the curve VC computed by averaging *CR* and *CL* coordinates.

Local vessel width along the axis can be evaluated by measuring the distance between the curves *CR(l)* and *CL(l)* at a fixed curvilinear coordinate l (see Figure 7.2 (e-f)).

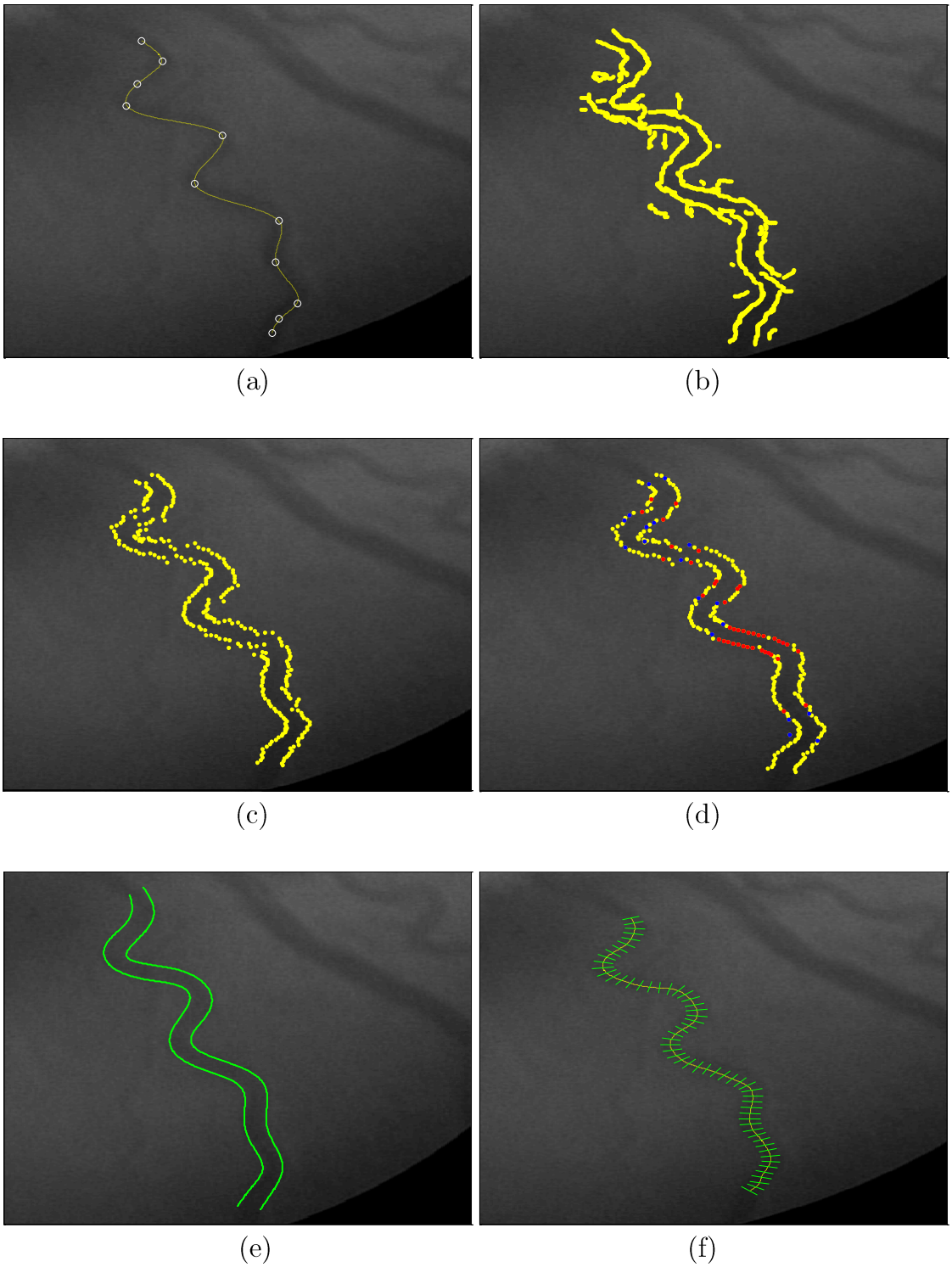

Figure 7.2 An example of vessel analysis with the proposed system: (a) the initial axis manually inserted; (b) the whole set of edge points extracted with the Canny filter; (c) the pairs of points extracted from the whole set; (d) the pairs of points after the correction step. Here the blue points were successfully corrected, while the red ones were forced to the average caliber of the analyzed vessel; (e) regularized borders; (f) vessel calibers locally evaluated along the axis.

7.3 Vessel Tortuosity

A tortuosity index is evaluated for the selected vessel, starting from the curve *VC*, by using an algorithm recently proposed by our group [87]. Some considerations on the traditional tortuosity measures, along with the main properties of the proposed tortuosity index, are presented in the following.

7.3.1 Tortuosity Properties

Vessel tortuosity measures do not have a formal clinical definition, but common practice has outlined an evaluation of the tortuosity with some well-defined properties. In order to obtain a clinically meaningful vessel tortuosity measure, i.e. a measure that is able to match the ophthalmologist's evaluation, it is necessary to make these properties explicit. Then, using a proper mathematical formulation of the tortuosity functional, the proposed measure must be shown to satisfy these properties.

7.3.1.1 Affine transformations

A sound approach to extract properties of a non-formally defined index consists in performing a preliminary study on the invariance properties of such index with respect to the most relevant transformation in the domain space. In particular, we will consider affine transformations of a vessel: translation, rotations and scaling. Translation and rotation transformations are not supposed to influence the perception of tortuosity. In fact, these transformation are related to the geographical position and orientation of the vessels in the retina, and do not alter in any way the clinical perception of tortuosity. Scaling of the single vessels does not seem to affect the clinical perception of tortuosity either. However, a warning flag must be raised in this context, since different clinicians may have different opinions about this issue. The scaling is particularly controversial when considering also the vessel caliber, but for the purpose of evaluating single vessel tortuosity, its perception can be safely considered invariant to scaling.

7.3.1.2 Composition

Composition properties deal with the behavior of tortuosity perception when two vessel curves are merged into a single curve, or when various segments of the same

vessel, in general with different tortuosity measures, build up to give the total vessel tortuosity.

Given two adjacent continuous curves s_1 and s_2, we define the combination of the two as:

$$s_3 = s_1 \oplus s_2 \tag{7.7}$$

Since the two composing curves are supposed to belong to the same vessel, we can assume the continuity of s_3 without loss of generality. In [67], an intuitive empirical principle was proposed:

$$\tau(s_1) \leq \tau(s_2) \Rightarrow \tau(s_1) \leq \tau(s_1 \oplus s_2) \leq \tau(s_2) \tag{7.8}$$

which means that, when composing two curves, the resulting tortuosity is between those of the composing curves. The counterexample shown in Figure 7.3, top panel, clearly shows that this statement cannot be accepted in conjunction with the principle of invariance with respect to rotation and scale: two curves (e.g., L_1 and L_2) perceived by themselves as almost non tortuous, when connected form an undoubtedly tortuous curve.

Therefore we propose a new composition property, such that a vessel s, combination of various segments s_i, will not have tortuosity measure less than any of its composing parts:

$$\tau(s_i) \leq \tau(s_1 \oplus s_2 \oplus \ldots \oplus s_n), \ \forall i = 1, \ldots, n \mid s_i \subseteq s \tag{7.9}$$

7.3.1.3 Modulation

It is useful now to express a monotonic relationship with respect to two other properties, which we will call 'frequency modulation' at constant amplitude and 'amplitude modulation' at constant frequency. It may be assumed that the greater the number of changes in the curvature sign (twist) is, the more tortuous the vessel can be considered. Similarly, the greater the amplitude (maximum distance of the curve from the underlying chord) of a twist is, the greater is the tortuosity associated with it. For two vessels having twists with the same amplitude, the difference in tortuosity varies with the number of twists φ:

$$\varphi(s_1) \leq \varphi(s_2) \Rightarrow \tau(s_1) \leq \tau(s_2) \tag{7.10}$$

and, conversely, for two vessels with the same number of twists (with the same frequency), the difference in tortuosity depends on the difference in amplitude α of the twists:

$$\alpha(s_1) \leq \alpha(s_2) \Rightarrow \tau(s_1) \leq \tau(s_2) \tag{7.11}$$

7.3.2 Available Tortuosity Measures

Various tortuosity measures have been proposed in the literature, but all fail in certain respects. In this section we will review the available methods for evaluating retinal vessel tortuosity, presenting some counterexamples in which these methods provide results that do not match with clinical perception.

7.3.2.1 Arc Length over Length Ratio

The simpler and most widely used measure of a vessel tortuosity is the ratio between its length and the length of the underlying chord [47], [67], [81], [83]. The idea of using this ratio is that the greater the value of the ratio, the more distant the vessel is from a straight line, i.e., the more tortuous it is. Unfortunately, being the surface of the retina close to a semi-sphere, the non-tortuous paradigm should be the circle arc. In fact, every vessel that has a constant and small curvature, regardless of the amplitude of the arc it describes (as for the main retinal vessels), will be regarded by an ophthalmologist as characterized by negligible tortuosity. Moreover, it is shown in Figure 7.3 that two vessels with very different tortuosity have the same arc length over length ratio measure.

7.3.2.2 Measure Involving Curvature

Hart [81] presented a number of tortuosity measures that involve the use of the integral of the absolute curvature or of the squared curvature. For a curve $(l) = [x(l), y(l)] : D \subset \mathbb{R} \to \mathbb{R}^2, s \in C^1(\mathbb{R})$, with l the curvilinear coordinate on it, the curvature $C_s(l)$ is:

$$C_s(l) = \frac{\dot{x}(l)\ddot{y}(l) - \ddot{x}(l)\dot{y}(l)}{\sqrt{\left(\dot{x}^2(l) + \dot{y}^2(l)\right)^3}} \tag{7.12}$$

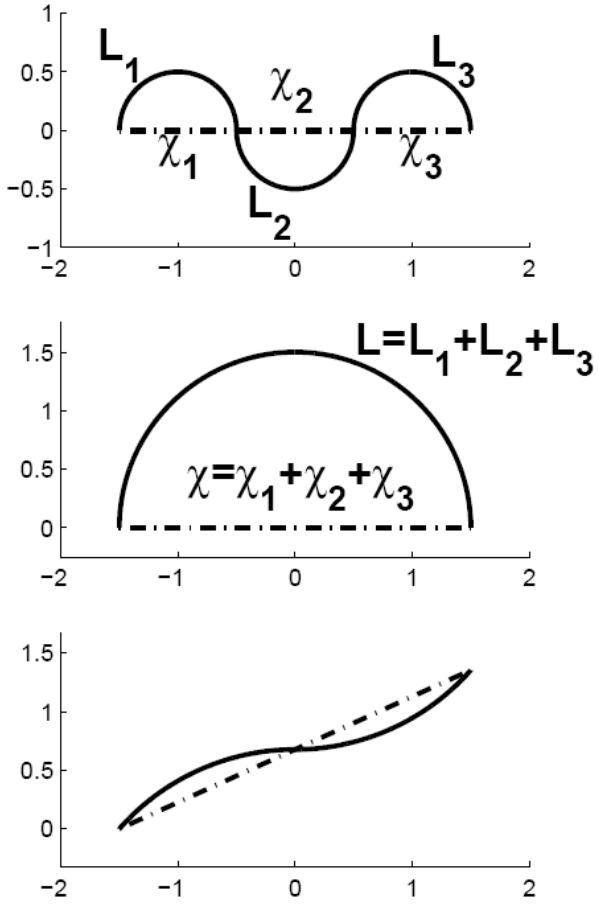

Figure 7.3 The first two curves (top and middle panel) have very different tortuosity but the same Length L and Chord Length χ. The second and last curves (middle and bottom panel) have the same average angular difference despite their different tortuosity. The curve in the bottom panel has a curvature integral of $\pi/2$ whereas the one in the middle panel has curvature integral π, even if that in the bottom panel is clearly perceived as more tortuous.

The idea behind this is that this integral should be a measure of the variability of vessel direction. However, the example presented in Figure 7.3 shows that a smaller curvature integral may correspond to a greater perceived tortuosity. In our opinion, there are three main reasons for this result. The first is that curvature is non zero only along arcs, while it is negligible along straight or almost straight segments; but straight segments together with arcs dramatically change the tortuosity appearance. The second is that changes in convexity (curvature sign) of the curve are not taken into account, while these are instead the features predominantly taken into account by expert graders to assess tortuosity. Finally, integrating along domain, possibly different in dimension, yields to measures depending on the aforesaid dimension. The ratios between the absolute curvature integral (or the squared curvature integral) and chord length (or vessel length) have been proposed to circumvent the latter point, but still the other two problems remain open with this definition of tortuosity.

7.3.2.3 Mean Direction Angle Change

More recently, a measure of tortuosity based on local directional changes of the vessel has been proposed [35]. It computes the average of the angles between sample points describing the vessel. For each point i of the vessel, it computes the unit vectors from the previous *step* point d_{i-step} and to the subsequent point d_{i-step}:

$$ad_s = \frac{1}{L_c - 2\,step} \sum_{i=1}^{n} arccos\left(d_{i-step} \cdot d_{i-step}\right) \tag{7.13}$$

In addition to the high sensitivity to noise, deriving from both from the digital quantization and the vessel extraction technique, this suffers from the problems mentioned above. Even the simple example of Figure 7.3 shows that a vessel with constant curvature, such as a semi-circumference, and a vessel formed by the juxtaposition of two arcs of circumference have the same average angle variation, despite their difference in tortuosity. Moreover, also herein this case vessel segments with no variation in direction do not affect the tortuosity.

7.3.3 Vessel Representation

The theoretical mathematical description of the vessel is a curve in a two-dimension space:

$$s(l) : D \subset \mathbb{R} \rightarrow \mathbb{R}^2 \tag{7.14}$$

The available description of the vessel is a sampled, quantized and noise corrupted version of the theoretical curve:

$$s(k) : s(l_k) \tag{7.15}$$

where l_k is a sequence of curvilinear coordinates that represent the sampling on the original vessel.

The sampling of a vessel may lead to a very sparse vessel description. Sparse description of the vessel further leads to a poor description of its dynamics, which may eventually fail to provide useful information on the vessel direction and on its derivatives. Sampling can be taken care of by means of an interpolation function, which describes the vessel between sampling points, where no data are present. Physiologically, vessels are structures continuous at least with their first derivative and this condition leads to the use of a cubic spline interpolation. Since the data are noisy, splines also offer the opportunity of filtering by using cubic smoothing splines.

The resulting spline curve is obtained from the available data by regularization:

$$\hat{s} = \operatorname{argmin}_{\hat{s}}\left[(1-\gamma)E_i(\hat{s}) + \gamma\left\|\hat{s} - s_q\right\|\right] \tag{7.16}$$

where $E_i(s)$ is what is called internal energy term, and represents the smoothness of the curve; γ is a weighting parameter, varying between 0 and 1, that sets the compromise between following the available data s_q and having a 'smooth' behavior. For $\gamma = 1$ $\hat{s}$ is the least square linear fit of the data, whereas for $\gamma = 0$ it is the variational cubic spline interpolant of the data. In this study we used $\gamma = 0.005$.

7.3.4 Tortuosity Calculation

When evaluating tortuosity, ophthalmologists integrate information about the number of vessel twists (changes in convexity, or curvature sign), and the size of the amplitude of each of the recognized twists. We would therefore decompose any curve into a set of consecutive segments of constant curvature sign. Having defined the curvature of a curve in (7.12), we define a subsegment s_i as a *turn curve* if:

$$\left[C_{s_i}(l) \geq 0,\ \forall l \in D\right] \vee \left[C_{s_i}(l) \leq 0,\ \forall l \in D\right] \tag{7.17}$$

In real images, it is common to find small oscillations (changes of convexity with very small amplitude) around the main vessel direction, due to the presence of noise. These oscillations might affect the correct decomposition of the vessel, since they would create a great number of artificial turn curves, which are not clinically significant.

An hysteretic threshold on curvature was thus used to deal with these small variations, as shown in Figure 7.4. To evaluate tortuosity, we also need the Chord Length L_χ of a curve, defined as the distance between the two extremes of the it:

$$L_s = \|s(\max(D)) - s(\min(D))\| \tag{7.18}$$

and the Curve Length L_c, defined as:

$$L_c = \int_{\min(D)}^{\max(D)} \left\|\frac{\partial s}{\partial l}\right\| dl \tag{7.19}$$

An hysteretic threshold of 0.03 has been set for arteries and one of 0.01 for veins. The two types of vessels have been kept separate, since ophthalmologists grade arteries and veins differently. Due to the possible presence of turn curves with zero curvature, the decomposition is not unique. Since the elimination of these turn curves might lead to the situation in which an increase in amplitude with straight segments

would not increase tortuosity, we chose to split the straight segments into two halves, assigning one to the preceding and one to the following turn curve.

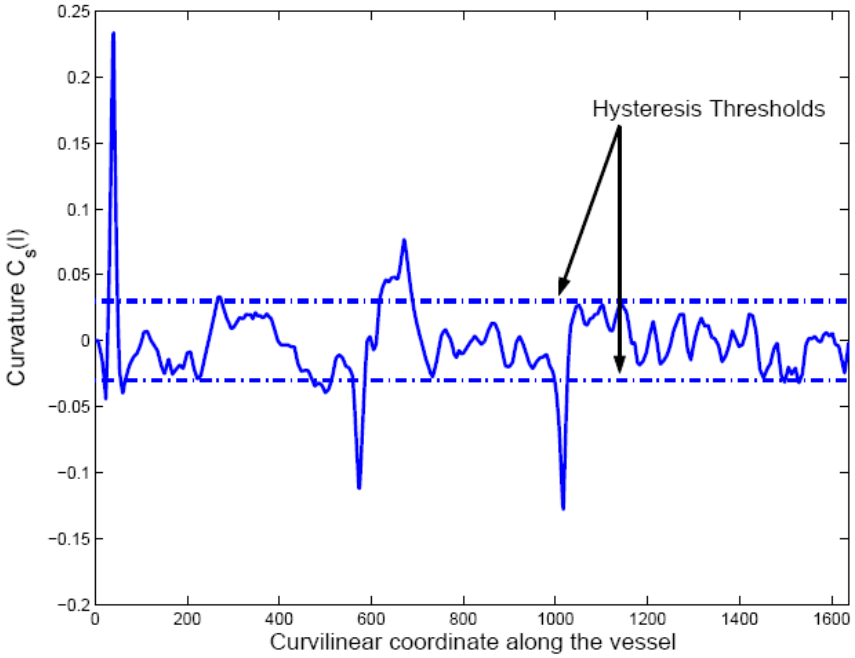

Figure 7.4 Curvature value along a vessel. The dashed lines indicate the hysteretic threshold for the convexity change.

7.3.4.1 Proposed Tortuosity Measure

Once a curve $s(l)$ is divided into n turn curves

$$s_i : s = s_1 \oplus s_2 \oplus \ldots \oplus s_n \tag{7.20}$$

a measure of vessel tortuosity can be proposed as:

$$\tau(s) = \frac{n-1}{n} \frac{1}{L_c} \sum_{i=1}^{n} \left[\frac{L_{c_{s_i}}}{L_{\chi_{s_i}}} - 1 \right] \tag{7.21}$$

This tortuosity measure has a dimension of $1/length$ and thus may be interpreted as a *tortuosity density*, allowing its comparison on vessels of different length. It is worth noting that when n is equal to 1 then τ is equal to 0 and thus vessels with a constant convexity have zero tortuosity. The proposed definition of tortuosity meets all the properties described in Sec. 7.3.1. In particular, the composition property is satisfied via the summation in (7.21), the amplitude modulation via the ratio of the length over the chord length for every turn curve, and the frequency modulation is

taken care of both implicitly by means of the curve splitting and explicitly through the multiplicative term *n-1* in (7.21).

A validation of the proposed tortuosity measure can be found in [65].

7.4 Results

To evaluate the reliability of vessel width estimation the set of 18 vessels belonging to the Scheie Eye ROP Width Dataset was analysed. The width of the vessels was computed with the proposed method and compared with the manual segmentation performed by a retinal imaging expert. For every vessel segment, a set of equally spaced calibers along the axis was measured and averaged in order to get the average vessel width. The performance of the algorithms was assessed by computing the correlation between the computer-aided and manual evaluations of the average caliber of the vessel segments. For the set of segments, we obtained a correlation $\rho = 0.96$. In Figure 7.5 the scatterplot of the average caliber values, from manual reference vs computer-aided evaluation, is shown.

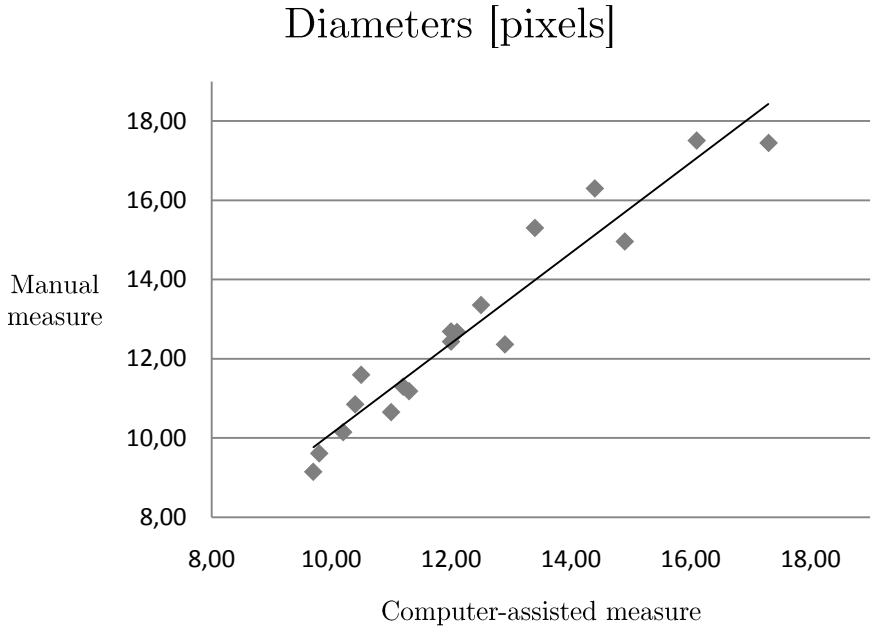

Figure 7.5 Scatter plot of the manual and computer-assisted diameters in pixels.

Similarly, the reliability of vessel tortuosity estimation was evaluated on the set of 20 vessels composing the CHOP ROP Tortuosity Dataset. Vessels were previously ordered by a retina specialist by increasing perceived tortuosity. The performance of the proposed method was assessed by computing the correlation between the computer-aided and manual ordering of the vessel tortuosity. Since we are considering correlations among rankings, the Spearman correlation ρ_s was used. For the set of 20

analyzed vessels we obtained $\rho_s = 0.93$. In Figure 7.6 the scatterplot of the tortuosity rankings, from manual reference vs computer-aided evaluation, is shown.

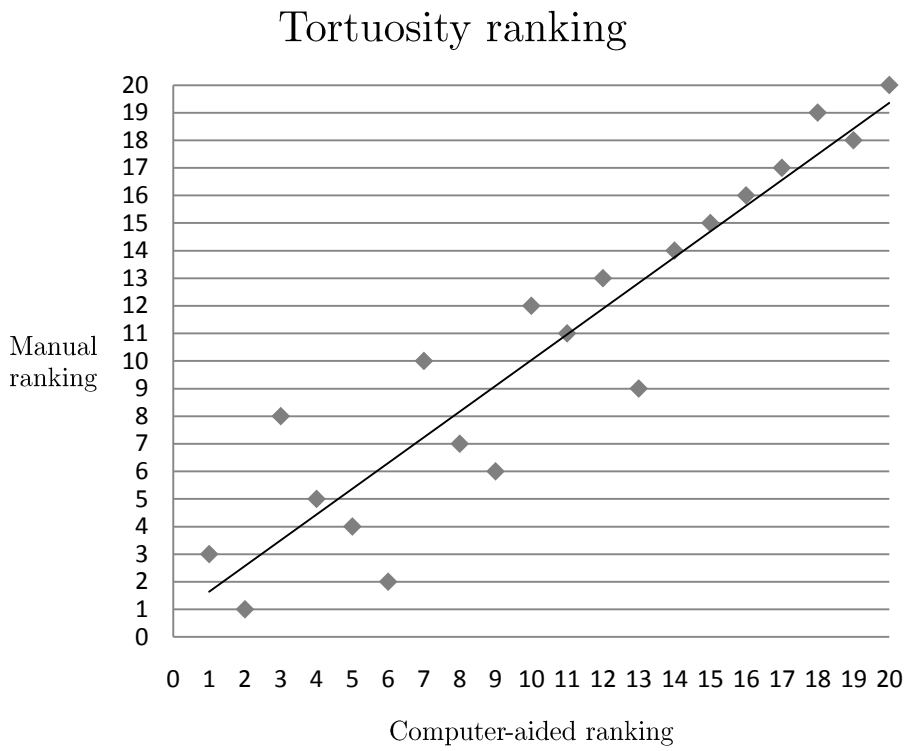

Figure 7.6 Scatter plot of the manual and computer-assisted tortuosity rankings.

7.5 Conclusion

Nidek NM200D is a portable non-mydryatic and non-contact fundus camera designed for retinal image acquisition on both adult and preterm born infants. Because of the anatomical characteristics of the infant retina and the peculiar technical features of the mentioned fundus camera, the images provided by Nidek NM200D are challenging to analyze and algorithms created for the analysis of adult images turn out to be unsuitable for the tracking of vessels in infant images. In this chapter an *ad-hoc* method was presented for the analysis of newborns images acquired with Nidek NM200D. Because of the large variability and the poor quality of such images we opted for a semi-automatic method to perform tracking on vessels and to quantitatively assess vascular tortuosity and width.

The most common semi-automatic methods in literature try an automatic tracking of the vascular network and then ask the user to manually correct the imperfections, by deleting or editing the extracted vessels, or by adding new segments that were not identified [83], [84]. For the proposed technique we adopted an alternative solution: the vessels to be analyzed are initially chosen by the user in an easy and fast

way, and the final results are not manually modified. This approach is particularly convenient with small FOV Nidek NM200D images, where few analyzable vessels are usually visible.

In order to assess the performance of the method, we performed two analyses: in the first one we computed the correlation between manually and computer-assisted estimated diameters in a set of 18 vessel segments. Calibers estimated with the proposed method were highly correlated with those measured manually ($\rho = 0.96$). In the second analysis we assessed the reliability of vessel tortuosity estimation by computing the correlation between the semi-automatic and the manual ranking of 20 vessels that were ordered by increasing perceived tortuosity by a ROP specialist. The two rankings showed high Spearman correlation ($\rho_s = 0.93$), and the scatter plot in Figure 7.6 shows that the rankings agreement is higher for more tortuous vessels (whose characteristics are usually related to a pathological condition), while it is slightly lower for less tortuous vessels (usually associated to a normal condition).

The method described has been used to implement ROPnet, a web based tool for the remote evaluation of vessel dilation and tortuosity in infant NM200D images (see Chapter 8).

Chapter 8

ROPnet, a web-system for Vessel Caliber and Tortuosity Estimation in ROP Retinal Images

In the perspective of the previous considerations, we propose a new web-based system to quantitatively assess vascular caliber and tortuosity from Nidek NM200D non-contact camera retinal images in ROP patients. The tool is based on the algorithm for semi-automatic vessel tracking described in Chapter 7 and it will allow clinicians to recover a quantitative estimation of these parameters in an objective, fast and user-friendly way.

8.1 Introduction

Retinopathy of prematurity (ROP) is a disease involving abnormal development of retinal vasculature in premature infants, which can lead to retinal detachment and visual loss [88]. Despite recent advances in management of disease and understanding of its underlying pathophysiology, ROP continues to be a leading cause of childhood blindness throughout the world.

The International Committee for the Classification of Retinopathy of Prematurity (ICROP) published in 1984 a classification system for ROP that was then revised in 2005 [15]. In this document ROP is described by means of several parameters. The most important are the retinal location involved, known as zone; the disease extent, expressed as clock hour; the stage of the disorder at the junction of the vascularized and avascular retina. The presence of plus disease is related to the severity of ROP: it presents abnormal dilation and tortuosity of the arterioles and venules and it is diagnosed by the comparison with a standard photography used in the CRYO-ROP study. The concept of pre-plus disease was introduced in 2005 to describe situations where there is mildly to moderately abnormal dilation and tortuosity of the central posterior retinal blood vessels (the case in between the normal condition and the plus disease). Pre-plus seems to be in most cases precursor to plus-disease.

Inter and intra-observer variability make very difficult, even for expert examiners, to evaluate in an objective way ROP severity. The first is related to the inaccuracies in qualitative evaluation based on the comparison with a standard photograph; while the second one is related to factors such as the type of ophthalmic lens used, clarity of the image, pigmentation of the retina, etc.

In order to reduce the risk for premature infants and to possibly provide a prompt therapy some regular checkups are needed in the first months after birth [89], [90], [91]. International guidelines have been established for screening: in general, the first examination takes place between 4 and 6 weeks of chronological age or between 31 and 33 weeks post-conceptional age. Subsequent examinations depend on the severity of any ROP detected. Subjects with no ROP may have only one further examination 6 weeks later, whereas subjects with significant disease may require weekly or even daily examinations, to assess if they have reached threshold disease [92], [93], [94]. At present this screening process is carried out by ophthalmologists skilled in the examination of infants' eyes, but the necessity of retina experts at the neonatal intensive care unit is conflicting with the decreasing number of ophthalmologists willing to perform ROP examinations [85]. Also, the number of infants requiring ROP examinations has increased thanks to improved survival of very low birth weight infants and even many developing countries are facing an increasing number of surviving premature infants without an adequate number of ophthalmologists trained to screen and treat ROP. Any system which can assist ophthalmologists in increasing the accuracy of their screening, or which could allow less highly trained individuals to carry out the screening (e.g., ophthalmic nurses) may be of clinical benefit. A possibility of providing some automated assistance in this screening process lies in accurate computer measurement of vessel width and tortuosity near the posterior pole of the retina.

Many systems for computer aided diagnosis (CAD) have been recently developed to accurately measure and quantify retinal vascular geometrical and morphological properties in premature infant images. The first is Retinal Image multiScale Analysis (RISA) developed by Martinez-Perez et al. [83]. It provides a semi-automatic tool for the labeling of the skeleton trees followed by an automatic procedure for measurement of vessel width, tortuosity and other geometrical indexes. Swanson et al. reported that tortuosity measurements were found to be occasionally inconsistent when compared to the vessel's actual bowing, because of RISA's insensitivity to the frequency at which a vessel bows [96]. Computer-Aided Image Analysis of the Retina (CAIAR), proposed by Wilson et al. [84] semi-automatically identifies the retinal vessels, with provision for human pixel editing if any vessels are inappropriately represented. It subsequently automatically measures the width and tortuosity of each vessel found. In [84] CAIAR readings, compared with five expert ophthalmologists' grading of 75 vessels on 10 retinal images, provided moderate correlation for both tortuosity (Spearman $\rho = 0.673$) and width ($\rho = 0.415$). ROPtool was developed by Wallace et al. [85], it semi-automatically traces retinal blood vessels and it only provides measures for the tortuosity of each vessel. VesselMap is a semi-automatic soft-

ware, developed by Imedos (Jena, Germany). It performs the tracking of principal vessels and it only provides information about the mean vessel diameter. Only one study was reported in literature, where retinal infant images were analyzed with such software [106]. Even if the mentioned programs have provided interesting results, none of them is easily accessible through the web and yet none has shown to be free of weak points and outperform all the others.

This chapter presents a novel web-based tool, named ROPnet, which offers a semi-automatic system to perform tracking on vessels and to extract a quantitative assessment of vascular tortuosity and width. Vessel analysis can be performed by using a web browser with a client-server setup: an image is uploaded to the server, an easy to use interface allows the client (i.e., user) to select a vessel to be analyzed. All the subsequent processing is performed server-side and the client will get the results, including the computed parameters, in few seconds. The segmentation strategy adopted is based on some edge extractor filter coupled with a module checking for regularity and smoothness typical of vascular structures (see Sec. 7.2). The tool was developed in particular for analysis of images acquired with Nidek NM200D (Nidek Co., Gamagori, Japan), which is a portable non-contact fundus camera presenting interesting features such as ease of use, portability, non-invasive diagnosis and low cost.

8.2 Methods

ROPnet was developed by taking into account two main purposes: the accessibility, at any time, by users from all over the world, and the user-friendliness of the system. The first goal was achieved by making the tool available through a web browser over internet connection. The second goal was met by developing a graphical user interface (GUI), to allow the client to intuitively interact with the server-based application that performs analysis on uploaded retinal images.

The web-based system was developed by using Html, Javascript and PHP scripting and it consists in several modules that involve exchange of data between client and server. The most important steps are client identification and image uploading, image storing and preprocessing, user friendly input setting, server-side vessel tracking and parameters computing, displaying interactive output.

The client-server system architecture will be described in detail in Sec. 8.2.1, while the vessel tracking methods along with tortuosity algorithm were described in the previous chapter. In Sec. 8.2.2 the tool functionality is illustrated.

8.2.1 Client-Server System Architecture

To enter the ROPnet analysis page, the user is required to login and access the tool member area. For every user logged in, a PHP session is created: sessions work by creating a unique identification number for each visitor and storing variables based on this ID. This allows to safely managing multiple simultaneous accesses preventing two users' data from getting confused with one another.

Once logged in, the client is automatically redirected to the upload page, where it is possible to browse the local drivers to choose a retinal image to be analyzed. The selected image is sent to the server, where it is temporarily stored until the analysis has not finished.

After image uploading and storing, a preprocessing algorithm aimed at enhancing the image contrast (described in Sec. 7.2.1) is launched server-side as a background process.

While preprocessing is running, the client is redirected to a web page displaying a JAVA applet, which is a graphical user interface that allows the user to choose vessels to be analyzed and to set important parameters needed for the subsequent analysis (the user interface functionality will be described in detail in Sec. 8.2.2). The applet sends the information acquired from the client to the server, where image analysis is launched. Analysis consists in vessel tracking and computation of clinical parameters and it was described in Sec. 7.2.2. After the analysis is finished, the server sends an answer to the quiescent applet, which redirects the user to a web page where results are displayed.

The estimated vessel centrelines and calibres, along with clinical indexes, are presented in an intuitive and user-friendly way with a new graphical interface realized as a second JAVA applet that allows the user to interact with the displayed information (see Sec. 8.2.2 for details). In the meanwhile, a text file storing a detailed report for the current analysis session is updated, saved on the server and available for download to the user, in order to keep track of the work done. A schematic diagram of the whole system architecture is shown in Figure 8.1.

8.2.2 ROPnet functionality

After logging in to the ROPnet member area, the user is redirected to the upload page where an image to be analyzed can be chosen from personal drivers and uploaded to the server. The only accepted format is jpeg, to reduce the downtime related to data transmission via the web connection. No constrain on image resolution is present. .It is recommended to use images as obtained from the Nidek NM200D fundus camera, without performing any digital preprocessing (i.e. geometrical or colour transformations) before the uploading. After image upload, a JAVA applet will

start, which allows the user to choose the vessel to be analyzed (one per time) and run the tracking algorithm (Figure 8.2). The graphical user interface allows the user to perform different actions: the image can be displayed in RGB color format or in green channel gray level; it is possible to manually outline the optic disc by clicking on its center and dragging to define its circular contour. Along with the optic disc, two lines dividing the image into four quadrants will be displayed. Lines can be rotated in order to manually define the position of the quadrants.

The area of vessel analysis may be restricted by defining the radius of an annular region centered in the optic disc. Zoom-in and zoom-out functions allow the user to enlarge the area displayed or go back to the original visualization. Once visualization has been set up, the user can select the vessel that will be analyzed. The vessel is chosen on the image simply by clicking on its end-points; a number of additional intermediate points can then be added, to outline more precisely the vessel layout and guide vessel tracking. An interpolating spline, connecting the inserted points, is drawn and displayed over the vessel and updated every time a new point is added by the user. Points can also be moved by dragging the mouse over them to correct the spline position, until the whole curve lays inside the vessel. Finally, the user can

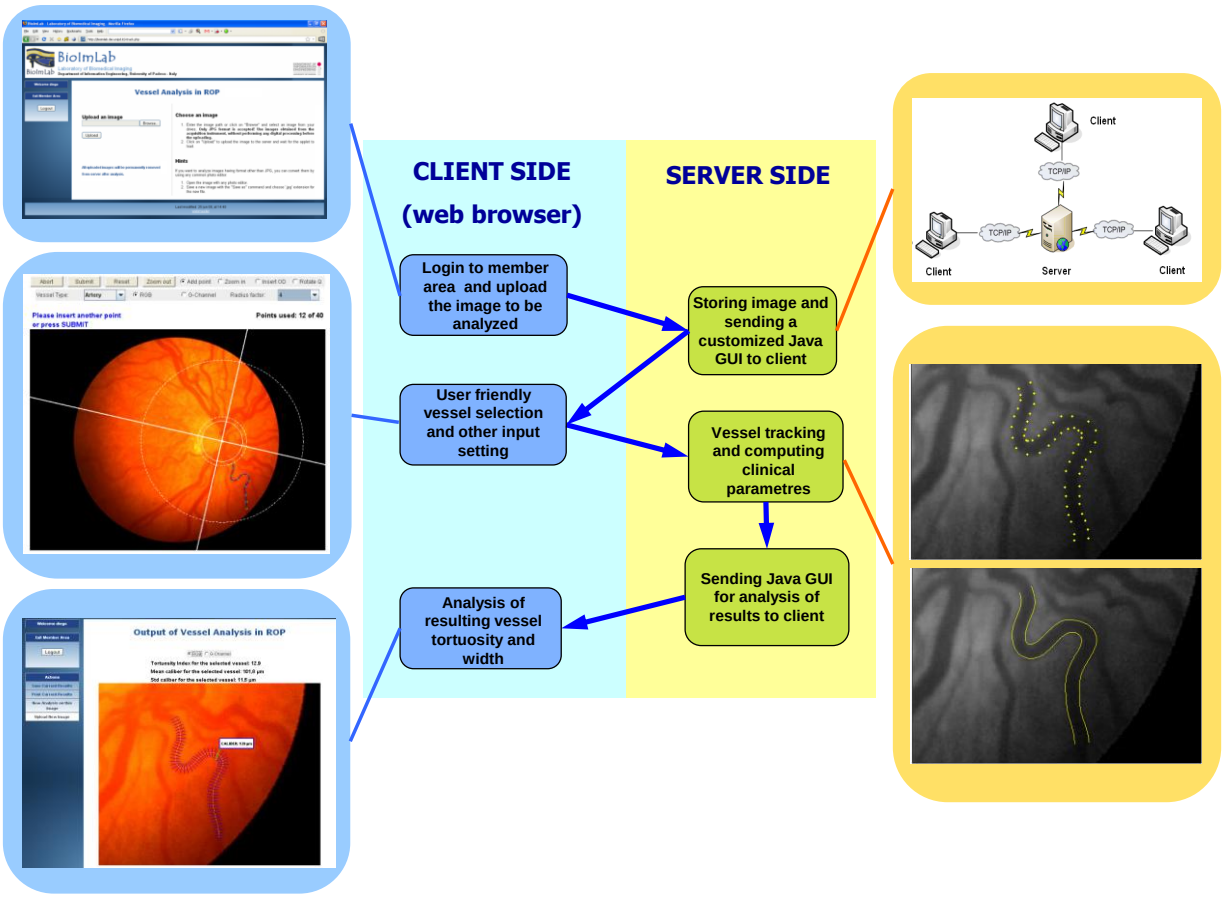

Figure 8.1 Scheme of the ROPnet client-server architecture.

define the vessel type by choosing between three possible options: artery, vein, or unknown. The vessel delineation procedure can be reset at any time before launching the processing algorithm and the analysis on the current image can be interrupted in order to change image or exit the tool.

Once the user is done with the input steps and the spline describes the approximate location of the vessel axis, automatic vessel tracking is performed over the selected segment. The processing step requires only few seconds (5 s on average), after which the client is automatically redirected to a new page, where results are displayed. A JAVA applet overlays the uploaded image with the tracking results, vessel axis and calibers and by moving the mouse cursor over the vessel it is possible to display the vessel widths at different locations. The quantitative clinical parameters returned are the vessel tortuosity index, the average caliber and its standard deviation along the segment. The latter two values are expressed in arbitrary units, defined as hundredths of length of the optic disc radius, or alternatively in pixels if the optic disc was not defined at the beginning of the analysis. From the current page it is possible to print results and to export them to a text file that can be downloaded on the client machine. The user can finally choose to analyze a new vessel on the same image, upload a new image, or log out from the ROPnet area (Figure 8.3).

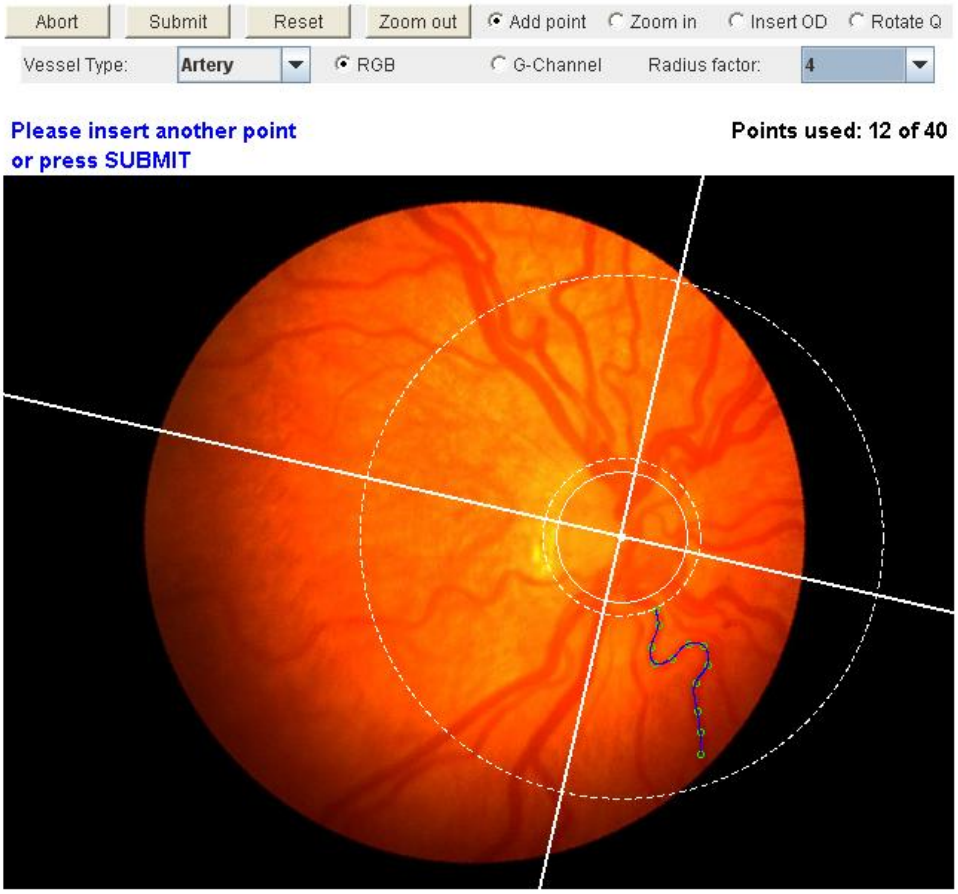

Figure 8.2 The ROPnet graphical user interface to select the vessel to be analyzed and to set up other parameters for the analysis.

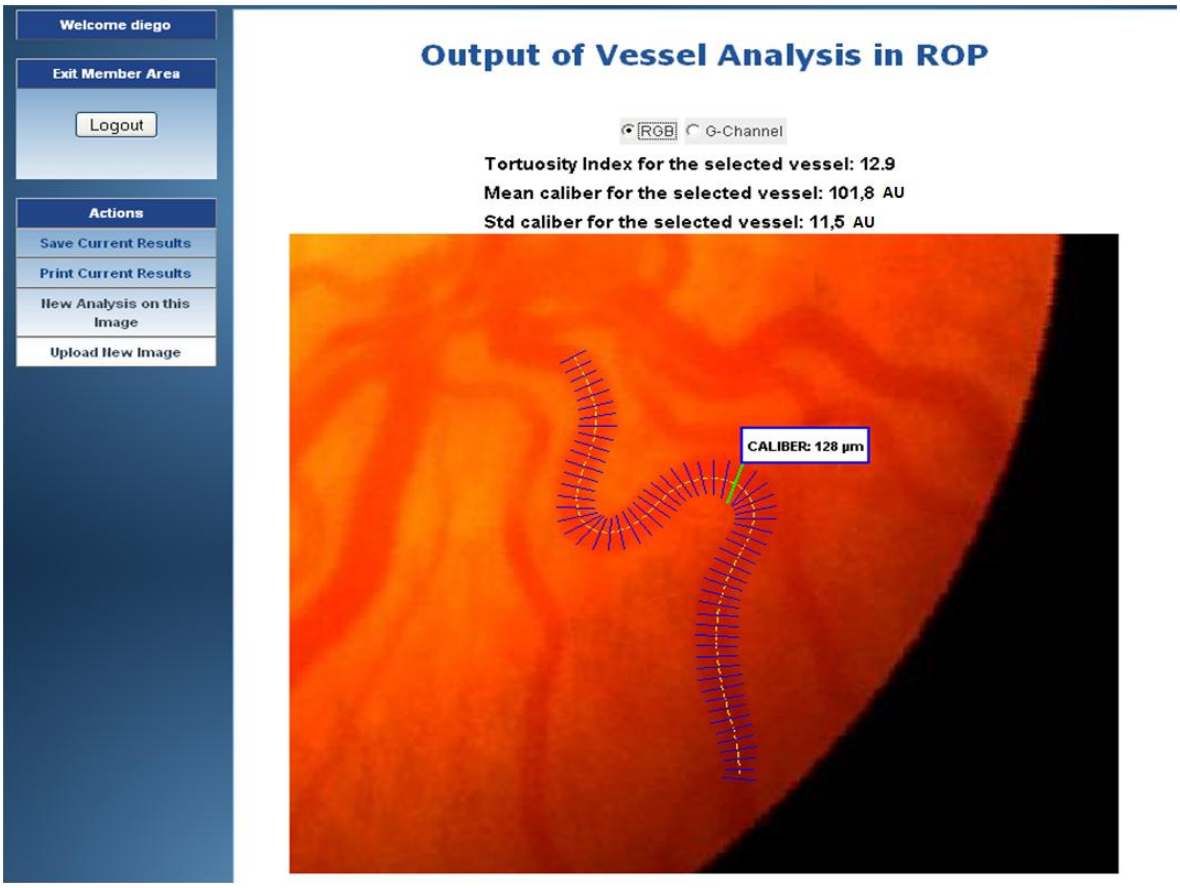

Figure 8.3 The ROPnet graphical user interface for the display of results.

8.2.2.1 Standardized Method for ROPnet

In collaboration with clinicians at the Children Hospital of Philadelphia a standardized protocol for image analysis with ROPnet was proposed. It describes in detail all the operations needed for the complete analysis of an image.

1. Upload image in JPG form
2. Draw the optic disc by choosing "Insert OD" radio button.
    a. Identify longest diameter of optic disc. This may be along any meridian and should not include the peripapillary area.
    b. Identify midpoint of above axis.
3. Demarcate the optic disc by dragging from midpoint (step 2b) to edge of optic disc along longest axis (step 2a).
    a. If the optic disc is oval, the solid circle that is drawn may enclose peripapillary area along axes shorter than the longest diameter of the optic disc.

4. Define the field of analysis by selecting "Radius factor" from pull-down menu so that the outer dotted line completely encompasses the entire image.
    a. If the study procedure requires standardization of length measurements, a radius factor of 3 is recommended.
5. Define quadrants by choosing "Rotate Q" radio button. Click and drag cross-hairs so that quadrants are appropriately divided.
    a. For each quadrant above, select the major artery and vein to analyze. Arteries can be distinguished from veins as follows: (i) arteries are lighter/more orange in color relative to darker/reddish color of veins; (ii) arteries generally have a smaller diameter than nearby veins; (iii) arteries tend to have more curvature (tortuosity) than nearby veins.
    b. For quadrants with multiple arteries and/or veins, select the largest and most tortuous vessel of each type.
    c. For a vessel that crosses multiple quadrants, the designated quadrant should enclose the longest segment of the vessel.
6. Visualize the desired vessel by choosing "Zoom In" radio button. Click and drag on the image so that the box includes the beginning and end of the desired vessel.
    a. Analysis should begin in the first quadrant on the first vessel starting clockwise from 12 o'clock.
7. Select "G-channel" radio button to better visualize vessel borders.
8. Track the vessel by selecting "Add point" radio button.
    a. Place initial point on the inner dotted circle at the center of the selected vessel. No points may be placed between the solid circle and the inner dotted circle.
    b. Place end point as far peripherally from the center of the optic disc that is visible. This point should also be placed at the center of the vessel. The end point must be within in the outermost dotted line.
    c. Place additional points along the center of the vessel. After dots are added, the solid blue line should appear centered within the vessel at all times. All turns (tortuosity) should have a minimum of 4 points. Spacing of the points depends on the total number of points desired, but in general, tortuous segments should receive more points (closer spacing) than straighter segments.
    d. Regarding branch points, the wider (main) branch should be selected for analysis. If branches have similar widths, select the vessel that comes off at less acute again.
9. Select appropriate "Vessel type" from the pull-down menu.
    a. Arteries can be distinguished from veins as described above (step 5).
    b. If one cannot distinguish the type of vessel, select "Unknown" for vessel type.

10. Click "Submit"
    a. After few seconds, the program will output an image showing measurement locations and 3 results: Tortuosity index, Average caliber, and Caliber standard deviation.
    b. It is recommended to save the vessel image by using the "Print current results" button on the left menu. As an alternative the image can be saved by pressing Ctrl-Print Screen and copying to another document for later identification of vessels.
11. Continue analysis on the next vessel by clicking "New Analysis on this Image." This allows analysis of the next vessel without changing the optic disc marker.
12. Repeat steps 6-10 for the largest and most tortuous artery and vein in each quadrant.
13. Save results after all vessels for the image have been analyzed, but clicking "Save Current Results."

8.3 Results

In Chapter 7 we assessed the accuracy for the vessel width and the tortuosity index estimations provided by the proposed algorithm. The tool described in this chapter includes a manual intervention by the user, therefore it was necessary to evaluate the robustness of the system in terms of inter- and intra-user results repeatability. To this aim, we used the Scheie Eye ROP Width Dataset (for the analysis of the vessel width) and the CHOP ROP Tortuosity Dataset (for the analysis of the vessel tortuosity).

In order to assess the inter-grader reproducibility of the measures, we had three graders use the system and independently grade each vessel of the two datasets. *Pearson's correlation coefficient* for each pair of graders and the *p-value* of a one-way ANOVA test for the three graders measures were computed. The first provides a measure of the linear association between each grader, while the latter checks that the results provided by each grader are not biased. Since the two tests are complementary, they provide a good evaluation of the measure reproducibility.

Table 8.1 shows that the correlation between the three graders is at least 0.86 and 0.99 for the width and the tortuosity measurements respectively, indicating that the three graders' assessments are coherently associated. The p-values were 0.57 and 0.99 for the width and the tortuosity measurements respectively, indicating that the mean of the distribution of the measures provided by the three graders are not significantly different.

Inter-grader Pearson's correlation coefficient							
Vessel Width				Vessel Tortuosity			
	Grader A	**Grader B**	**Grader C**		**Grader A**	**Grader B**	**Grader C**
Grader A	1.00	0.87	0.86	**Grader A**	1.00	0.99	0.99
Grader B	0.87	1.00	0.88	**Grader B**	0.99	1.00	0.99
Grader C	0.86	0.88	1.00	**Grader C**	0.99	0.99	1.00

Table 8.1 Inter-grader correlations for each pair of users for both vessel width and tortuosity measurements.

In order to assess the intra-grader repeatability, for both the datasets the analyses were repeated two times per vessel by the same user. Consecutive repetitions of vessels in the same image were avoided to prevent memory effects. *Pearson's correlation coefficient* and the *p-value* of a paired t-test were computed for every grade-regrade pair of measures.

	Intra-grader (grade-regrade) test					
	Vessel Width			Vessel Tortuosity		
	Grader A	**Grader B**	**Grader C**	**Grader A**	**Grader B**	**Grader C**
Correlation	0.96	0.93	0.97	0.99	0.99	0.99
p-value	0.84	0.9	0.82	0.95	0.92	0.98
ICC (95% CI)	0.94 (0.85-0.98)	0.93 (0.82-0.97)	0.96 (0.90-0.98)	0.997 (0.993-0.998)	0.995 (0.989-0.998)	0.999 (0.997-0.999)

Table 8.2 Intra-grader correlations, p-values and ICC (with 95% CI) for grade-regrade pair of measures, for both vessel width and tortuosity measurements.

Table 8.2 shows that the grade-regrade correlation is at least 0.93 and 0.99 for the width and the tortuosity measurements respectively, indicating that the grade-regrade graders' assessments are coherently associated. The p-values were at least 0.82 and 0.92 for the width and the tortuosity measurements respectively, indicating that the mean of the distribution of the grade-regrade measures provided by the three graders are not significantly different.

To have one more estimation of the measures reproducibility, the intra-class correlation coefficient (ICC) was computed among the three graders, (by using the average grade-regrade measure for each grader, to evaluate inter-grader repeatability), and between the grade-regrade measures of each grader (to evaluate intra-grader repeatability). The ICCs obtained among the three graders were 0.86 (with 0,71-0.94 as 95% CI) and 0.993 (with 0.985-0.997 as 95% CI) for the width and the tortuosity measurements respectively. Besides, as shown in Table 8.2 the ICC for the grade-regrade measures is at least 0.93 and 0.99 for the width and the tortuosity measurements respectively. The ICC analysis confirmed the good reproducibility (both inter- and intra-grader) of the system measures, as anticipated by the previously described tests.

8.4 Conclusion

The web based tool proposed for vessel analysis allows extracting important clinical parameters, such as vessel tortuosity and width, in a quantitative and reproducible way. These parameters are strongly related to the presence and severity of ROP.

An important initial step in validating a quantitative tool for assessing severity of vessel changes in ROP is to establish its accuracy and reproducibility. Later steps will examine whether the tool is accurate in its prediction of ROP in eyes at risk.

Several studies have examined quantitative measurement of retinal vessel width and tortuosity from digital images of eyes at risk for ROP [47], [78], [80], [84], [95], [96], [97], [98]. A few of these vessel analysis systems have examined the reliability of width measurements [99], [100], but to our knowledge none have addressed the reliability of tortuosity measurements.

In this work we evaluated both the accuracy of vessel width and tortuosity index estimation (see Chapter 7), along with the inter- and intra-user analysis repeatability. The system provides accurate measures of the clinical indexes, showing very high correlations with the manual ground truth.

While ROPnet may introduce some variability on results, since vessel selection is a manual choice, our results did not show any significant differences in the reproducibility. Wallace et al. addressed a similar problem, in which their ROPtool program was unable to consistently choose the most important vessels for each quadrant without operator input [95], [98]. Operator input, and thus less automation may improve the accuracy of quantifying vascular abnormalities, but it may also decrease reproducibility. A possible drawback of increased operator involvement is the lengthening of the analysis time. The user-friendly interface provided in ROPnet makes it possible to speed up the analysis, which usually takes less than one minute, therefore the practical usability of the tool in clinical situations is not reduced.

In the current version, the system allows the analysis of one vessel per time and we focused our attention on the reliability of the clinical indexes evaluated on the single vessel segments. Future work will investigate if the parameters provided by the system can actually be used to assess the state of the patients; to this aim, we will combine information estimated from the single vessels to obtain a global clinical index for the whole image.

The web-based solution and the user friendliness of the interface make the tool available to a wide range of users. In this way, we overcome important problems related to ROP diagnosis, such as the necessity of a retina expert at the neonatal intensive care unit. Moreover, the choice to run vessel analysis as a client-server application allows us to easily provide users with the latest developed version of the algorithms.

At present, a beta version of the system is hosted at the website http://bioimlab.dei.unipd.it; it is under beta testing and will be soon publicly available.

Chapter 9

Vessel Network Segmentation for wide FOV Infant Images

Regional shortages in the availability of ophthalmologists to provide ROP diagnostic examinations are an important barrier to ensuring appropriate ROP care. One potential solution is to decrease the number of indirect ophthalmoscopy examinations by first screening with some other method. Retinal photography to evaluate ROP can be considered an important alternative to indirect ophthalmology and different digital retinal cameras that can be used in the NICU are commercially available. In general, they can be categorized as wide-angle cameras (e.g., RetCam) and narrow-angle cameras (e.g., Nidek NM-200D). Wide-angle cameras provide a greater view of the retina (e.g., 120-130° field of view) than narrow-angle cameras (e.g., 30° field of view). The RetCam fundus camera, a retinal wide-field digital imaging system, allows documentation of large parts of the infant retina within minutes and several studies [101] have evaluated the value of wide-field digital imaging in screening for ROP. On the opposite side, the poor quality of wide field infant images makes the analysis quite challenging and not feasible with standard tracking algorithms for adult images.

In this chapter, some considerations are made about the analysis of RetCam images with the method presented in Chapter 4. The system settings turned out to be unsuitable for working with infant images. In order to force the detection of the very thin and low-contrast vessels we had to finely tune some parameters, but this led to the extraction of an high percentage of false vessels generating from artifacts and choroid. Since the rationale of the algorithm developed for adult images seems intrinsically unusable in this situation, a novel technique for the automatic vessel identification in infant retinal images acquired with RetCam is presented. Initially the vessel structures are enhanced by means of different matched filtering techniques, and extracted from the background with a local thresholding followed by morphological operations. The second step consists in a supervised classification of vessel structures based on SVM, in order to discard segments originating from noise/artifacts or from choroidal vessels.

9.1 Introduction

Before presenting, in Sec. 9.2, novel specific techniques for the analysis of wide FOV infant images, the RetCam fundus camera and the features of the images it acquires are shortly described in this section.

9.1.1 RetCam Fundus Camera

The RetCam fundus camera (Clarity Medical System, Pleasanton, CA, USA) has a VGA sensor able to acquire videos at a resolution of 640 x 480 pixels with 120 or 130 degrees field of view. Single images are then extracted by selecting the video frames that present the highest quality in term of vessel visibility.

Some hallmark of ROP can be located in the most peripheral area of the eye, where retinal blood vessels grow during the last weeks of gestation. The digital technology of RetCam provides images that give information about the entire extension of the lesion, because of the wide field of view. On the other side, the analysis of RetCam images is a difficult, time consuming and subjective issue. The ophthalmologist has to evaluate a large number of images that may present pathology at different severity.

The main drawbacks of RetCam infant images (if compared to images provided by standard fundus cameras used for the screening of adult eyes) are:

- low contrast
- presence of interlacing artifacts since images are actually isolated video frames
- very narrow blood vessels, due to the very wide field of view coupled with a small VGA sensor
- non uniform illumination in the wide captured field of view
- strong visibility of choroidal vessels (related to the lack of pigmentation of infants choroid)

All these aspects make the automatic analysis of RetCam images quite challenging. Traditional algorithms that successfully perform vessel tracking on standard fundus images show poor performance on these images acquired from newborns and customized techniques are necessary. Two models of RetCam fundus camera are shown in Figure 9.1.

Figure 9.1 Two models of RetCam Clarity fundus camera: on the left RetCam II and on the right RetCam 3.

9.2 Methods

The proposed analysis of RetCam infant images is aimed at automatically extracting the retinal vessel network. Only the position of vessels (identified by their centerline) is considered here and no effort is provided to evaluate vessel diameters, since most of the structures of interest have a caliber ranging between 1 and 3 pixels in this kind of images [96].

In this section some considerations are reported about the unsuitability of the method proposed in Chapter 4 for the analysis RetCam infant images. The multidirectional graph search approach for the extraction of the vascular network was tried and showed poor performance because of the low quality and the peculiar characteristics of RetCam images. In Sec. 9.2.2 a novel automatic tracking technique is presented.

9.2.1 Multidirectional Graph Search Approach in RetCam Images

As mentioned above, the characteristics of the images acquired with RetCam make their analysis challenging. Other than the anatomical aspects (such as the strong visibility of choroidal vessels) the morphological aspect of the vessels, related to the technical features of the acquisition instrument, are critical. The very wide field of view, coupled with the low resolution VGA sensor of RetCam, make the vessels to appear as very thin structures, poorly contrasted and almost evanescent in some regions. The method presented in Chapter 4 was tested with such images and its initial performance turned out to be poor because of two main causes: a) the inability to find an adequate number of reliable seed points and b) the difficulty to track vessels as minimum path structures. Both the mentioned problems lead to a partial identification of the network, where only few vessel segments can be extracted (Figure 9.2). We tried to appropriately tune some parameters in order to adapt the method to the RetCam images. In the seed finding procedure described in Sec. 4.2.2 the threshold to select the candidate points was lowered: this produced the effect of increasing the number of seeds extracted, but it also brought the unavoidable drawback of including a lot of false positives points, originating from noise, artifacts or gray level variations related to choroidal structures. In order to facilitate the evolution of the minimum cost paths inside the vessels the preprocessing procedure described in Sec. 4.2.1 was revised and the dimensions of the structuring elements used for the morphological operations were modified according to the resolution and the size of RetCam images. In this case the preprocessing is not aimed at removing the central reflex (not visible in these images), but at emphasizing the dark regions related to the presence of retinal vessels against brighter background pixels. Lastly, the false vessel detection module described in Sec. 4.3 was unsuitable with RetCam images and could not be applied: the eigenvector ν^- is unstable because it is sensitive to noise, which sometimes has a scale comparable with the very thin vessels. Thus it was not possible to identify an interval of confidence to discriminate between values of d related to true or false vessels.

Anyway, after tuning the algorithm as described above, we tested it on the 20 images belonging to the Clarity ROP Dataset. Vessels automatically detected were compared with the ones manually traced in the ground-truth images. We obtained a *sensitivity* of 0.75 and a *false vessel detection* of 0.33. Even if the sensitivity is good, on average one third of the extracted segments are false vessels and this is not acceptable if we aim at using the segmentation to compute clinical diagnostic indexes to assess the presence and/or the gravity of ROP. In Sec. 9.3 and 9.4 results presented above will be discussed and compared with the ones obtained with the novel method described in the following sections.

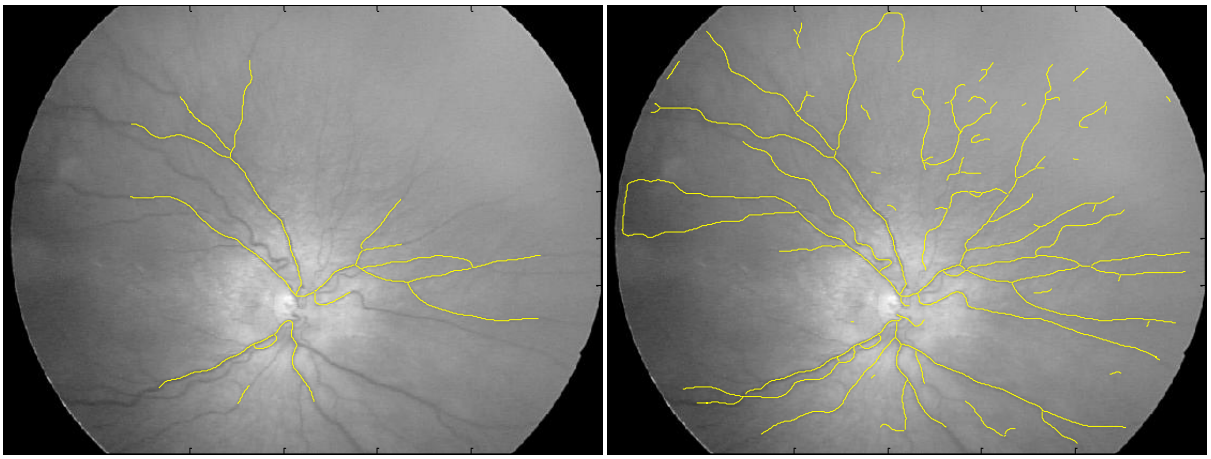

(a) (b)

Figure 9.2 Example of vessel axis tracking results with the multidirectional graph search approach on a RetCam image (a) with the original algorithm for adult image settings and (b) after tuning the algorithm.

9.2.2 A novel approach

To overcome the problems described in the previous section, a novel method is proposed for the automatic extraction of the vessel axis network in infant RetCam images. The technique includes a preprocessing step to enhance the image quality. The vessels are extracted by means of morphological operations and the vascular segments are classified as true or false vessels using a Support Vector Machines (SVM) supervised approach.

9.2.2.1 Preprocessing: Image Quality Enhancement

As previously mentioned, during the acquisition the RetCam fundus camera registers a video and the images are single frames, manually selected, presenting a good contrast between vessels and background. Because of the motion of the eyes, such frames are affected by interlacing artifacts and a deinterlacing algorithm is used to limit this problem. Two sub-images I_O and I_E are extracted from the original image I. They are made up respectively with the odd and the even horizontal lines of I. The missing lines of I_O and I_E (i.e. the even and the odd lines respectively) are interpolated, obtaining respectively I_O^I and I_E^I. Finally I_O^I and I_E^I are aligned maximizing the 2D correlation coefficient and the final deinterlaced image I_D is created by merging the odd and even lines of I_O^I and I_E^I respectively. The effect of the described deinterlacing preprocessing can be appreciated in Figure 9.3.

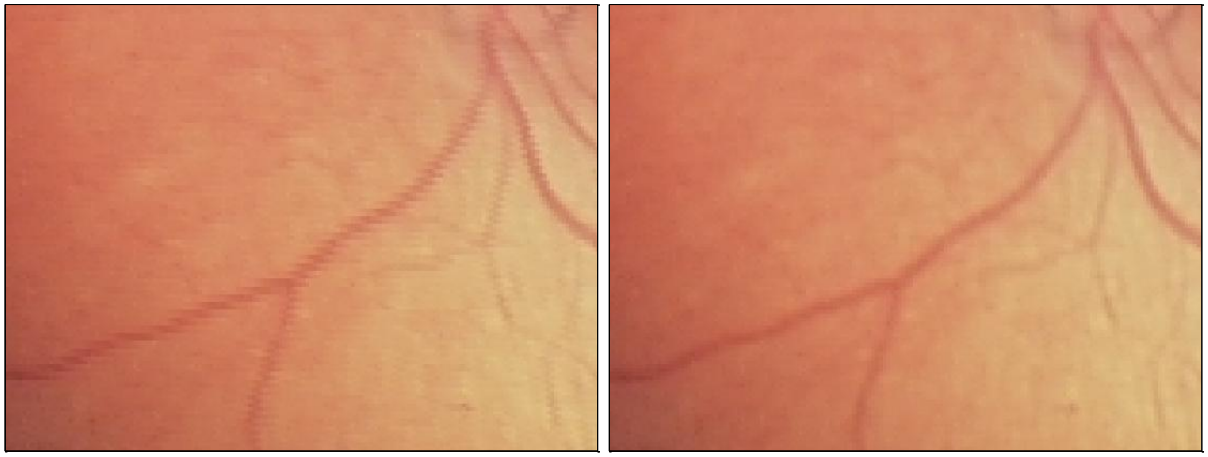

(a) (b)

Figure 9.3 Particular of a RetCam image affected by the interlacing artifact (a) and the result of the deinterlacing preprocessing (b).

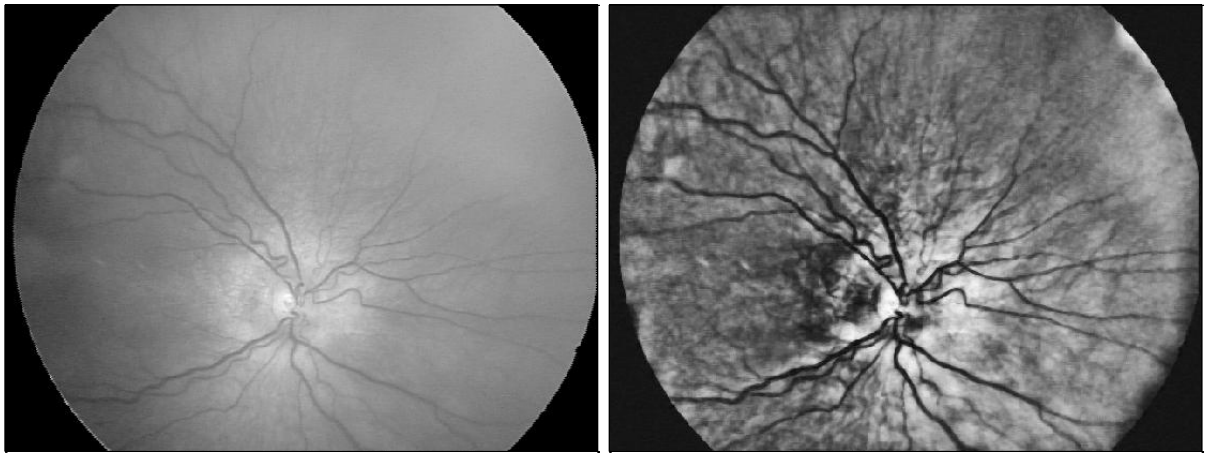

(a) (b)

Figure 9.4 Example of application of the image enhancement preprocessing: (a) original image green channel; (b) enhanced image.

The following steps are aimed at equalizing the illumination and emphasizing the contrast between the vessel structures and the background.

The green channel is extracted from the RGB image and the local average intensity, computed inside N pixel sized blocks, is subtracted from the image, in order to equalize the background illumination.

To increase the contrast, a histogram matching technique was adopted: the image histogram is matched to a Gaussian function having mean $\mu = 0.4$ and standard deviation $\sigma = 0.2$ (in a 0-1 range of pixel intensity). This approach standardizes the gray level distribution of the images that will be processed, by limiting the high intensity variability of images acquired with RetCam. Moreover, the chosen σ ensures that a consistent part of the gray level range is used and in most cases the original gray level range is stretched to match the target Gaussian function. The enhanced image is decomposed in its directional components by applying a directional filter bank as de-

scribed in [102]. Every component is processed with a median filter in order to limit the noise originating from the histogram stretching and finally a new image is made up by averaging the filtered directional components. In Figure 9.4 the effect of illumination equalization and contrast enhancement is displayed.

9.2.2.2 Filtering

In order to identify the vessel structures in the image, two different filtering techniques were applied. Both the techniques are based on the Laplacian of Gaussian (LoG) kernel: the Laplacian is an isotropic measure of the 2nd spatial derivative of an image; it highlights the regions of rapid intensity changes and it is therefore used for edge detection [103]. Because the kernel approximates a second derivative measurement, it is very sensitive to noise. To counter this fact, the image is often Gaussian-smoothed before applying the Laplacian filter.

This step reduces the high frequency noise components before the differentiation step. In practice, since the convolution operation is associative, the Gaussian smoothing filter and the Laplacian filter can be convolved, creating the Laplacian of Gaussian kernel.

The first filter used is based on a traditional LoG symmetric kernel, designed as:

$$H1 = Q * \exp(-0.5 * (x^2 + y^2)/\sigma^2) \tag{9.1}$$

where σ is the standard deviation that assumes different values according to the used scale and Q is a normalizing factor defined as:

$$Q = A * (1 - k * (x^2 + y^2)/\sigma^2) \tag{9.2}$$

with A = 1 and k = 0.5.

The second filter used is a directional version of the LoG and it uses a kernel built starting from an asymmetric Gaussian function:

$$H2_\theta = G_{\theta,xx} + G_{\theta,yy} \tag{9.3}$$

where $G_{\theta,xx} = dG_\theta/d^2x$, $G_{\theta,yy} = dG_\theta/d^2y$ and

$$G_\theta = \frac{1}{2\pi|\Sigma|^{1/2}} \exp(-0.5 * X_\theta \Sigma^{-1} X_\theta^T) \tag{9.4}$$

with $\Sigma = \begin{bmatrix} \sigma_x^2 & 0 \\ 0 & \sigma_y^2 \end{bmatrix}$ where σ_x assumes different values according to the filter scale and $\sigma_y = \sigma_x/3$.

$$X_\theta = [x, y] * R_\theta \tag{9.5}$$

where R_θ is the rotation matrix for the angle θ.

The LoG directional filter was evaluated at seven directions from 0 to 180° and both symmetric and asymmetric filters were analyzed at six different scales. When the scale (and direction for the asymmetric kernel) matches the size (and the direction) of the vessel, the filter response will be maximum. Therefore the final filter response is computed in the following way:

- for the asymmetric filter, at every fixed scale the outputs from different directions are averaged.
- for both the symmetric and asymmetric case the highest response among all scales is kept for every pixel of the image.

Both filters emphasize the vascular structures with different behaviors: the symmetric kernel provides a coarse description of vessels presenting higher responses with larger structures, while the asymmetric kernel provides a finer description of thin structures, highlighting low-contrast capillaries and maintaining details on thin vessels laying one near another.

9.2.2.3 Extraction of the Axis Network

The filter outputs are characterized by bright vessel structures on a dark background. The segmentation of vessel structures is performed by applying a local threshold to the filtered images. This provides binary masks, where pixels that belong to vessels are set to 1 and everything else is set to 0. A morphological skeletonization is used in order to thin all the identified structures and extract the network composed by their axes. It is important to notice that two versions of vessel axis network are now available: one coming from the symmetric LoG and another from the asymmetric LoG filter.

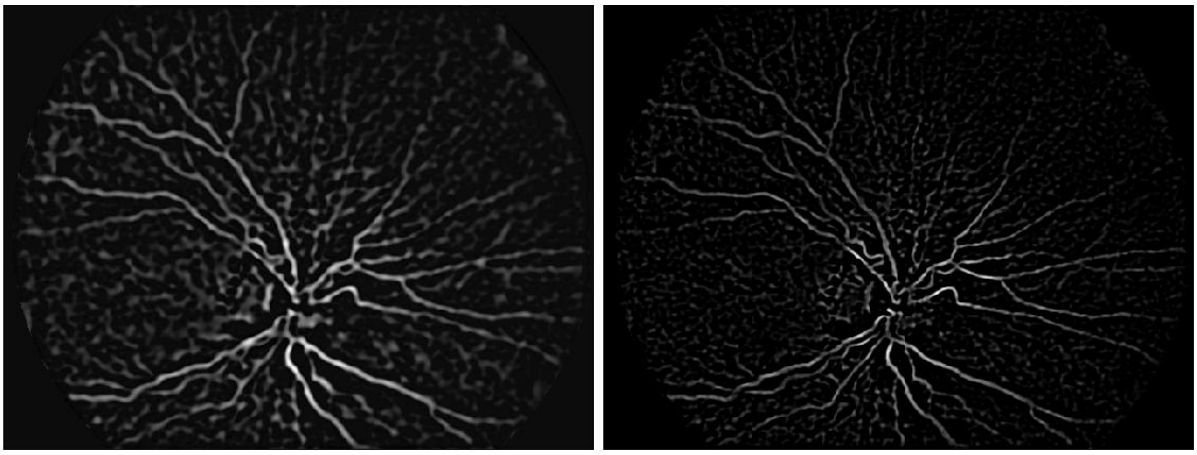

(a) (b)

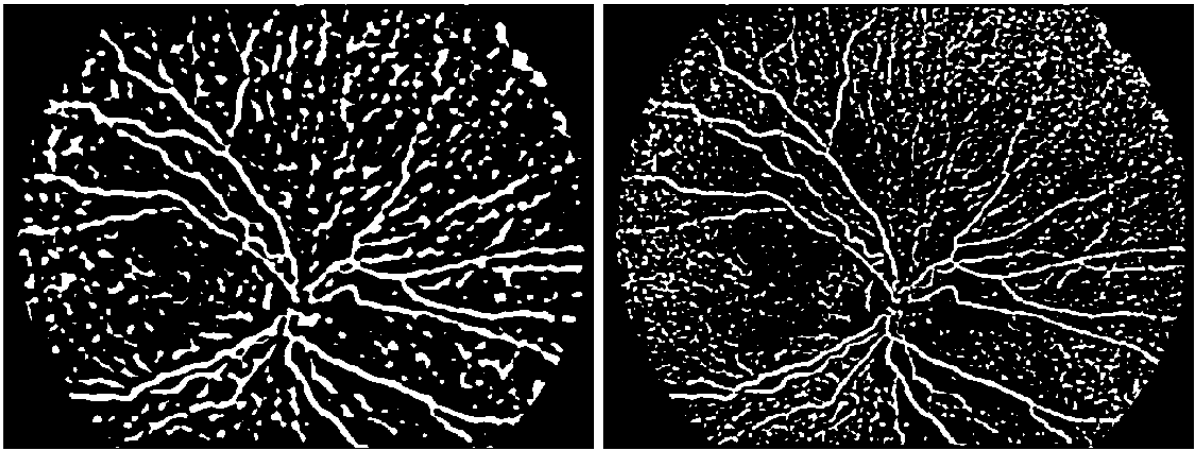

(c) (d)

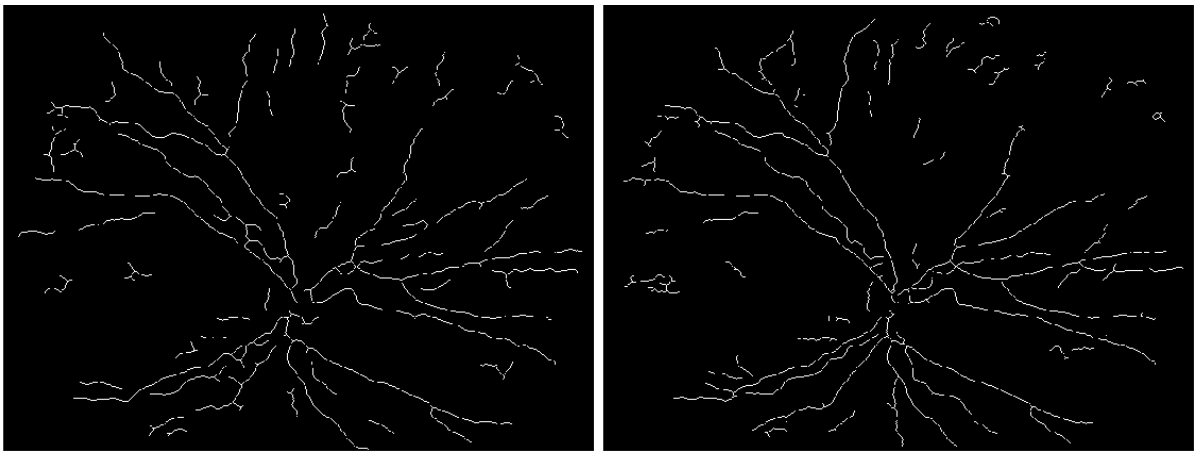

(e) (f)

Figure 9.5 Example of filtering and extraction of the axis network applied to the image displayed in Figure 9.4. Symmetric LoG filter: (a) output of the filter, (c) result of the local thresholding and (e) axis network obtained with the skeletonization. Asymmetric LoG filter: (b) output of the filter, (d) result of the local thresholding and (f) axis network obtained with the skeletonization.

9.2.2.4 Classification

The networks obtained so far include segments that correspond to axes of true vessels and segments originating from noisy structures, artifacts and choroidal vessels. A supervised classification procedure, based on Support Vector Machines (SVM) is used to discriminate and discard segments that do not correspond to a true vessel axis.

Support Vector Machines

SVM is a supervised learning method used for classification and regression. A classification task usually involves separating data into training and testing sets. Each instance in the training set contains one "target value" (i.e. the class labels) and several "attributes" (i.e. the features or observed variables). The goal of SVM is to produce a model (based on the training data) which predicts the target values of the test data given only the test data attributes.

Given a training set of instance-label pairs $(\boldsymbol{x}_i, y_i)$, $i = 1,...,l$ where $\boldsymbol{x}_i \in R^n$ and $\boldsymbol{y} \in \{1, -1\}^l$, the support vector machines require the solution of the following optimization problem:

$$\min_{w,b,\sigma} \ \frac{1}{2} \boldsymbol{w}^T \boldsymbol{w} + C \ \sum_{i=1}^{l} \xi_i \tag{9.6}$$

$$\text{subject to} \quad y_i \ (w^T \phi(x_i) + b) \geq 1 - \xi_i \ , \quad \xi_i \geq 0$$

Here training vectors $\boldsymbol{x}_i$ are mapped into a higher (possibly infinite) dimensional space by the function $\boldsymbol{\Phi}$. SVM finds a linear separating hyperplane with the maximal margin in this higher dimensional space. C > 0 is the penalty parameter of the error term. Furthermore, $K(\boldsymbol{x}_i, \boldsymbol{x}_j) \equiv \boldsymbol{\Phi}(\boldsymbol{x}_i)^T \ \boldsymbol{\Phi}(\boldsymbol{x}_j)$ is called the kernel function. For this work the Radial Basis Function (RBF) was used as kernel:

$$K(\boldsymbol{x}_i, \boldsymbol{x}_j) = exp\left(-\gamma \left\| \boldsymbol{x}_i - \boldsymbol{x}_j \right\|^2\right) \tag{9.7}$$

where $\gamma > 0$ is a parameter. This kernel nonlinearly maps samples into a higher dimensional space so that, unlike the linear kernel, it can handle the case where the relation between class labels and attributes is nonlinear. Furthermore, the linear kernel is a special case of RBF [104]. Another reason to choose this kernel is to limit the complexity of the model, since for example the polynomial kernel has more hyperparameters than the RBF kernel. Finally, the RBF kernel has fewer numerical problems [105].

In order to use SVM, we proceeded with the following steps:

- We divided data in two sets: a training set and a testing set.
- From every vessel segment belonging to images in both sets we extracted and scaled features used to train the classifier and to test the learned model.
- In the training phase, we used a cross-validation approach to find the model (i.e., estimate the two parameters C and γ) that provides the highest accuracy for the classification.

We used the derived model to classify vessel segments that belongs to the testing set into "vessel" or "non-vessel" classes.

Training and Testing Sets

We applied the preprocessing, the filtering techniques and the skeletonization operation described above to the 20 RetCam images chosen as ground-truth, in order to obtain for every image two possible vessel axis networks (one for the symmetric and one for the asymmetric LoG filter).

We divided the 20 image set in two subsets. A training set including the axis segments from six images was used to train the SVM (2792 segments obtained from the asymmetric LoG filter and 1772 segments obtained from the symmetric LoG filter) and all the segments in the remaining 14 images were used to test the classifier.

Used Features

In order to train the SVM model (and to use it to classify vessels) every vessel segment has to be described by some features capable to assign the segment to the corresponding class.

Given a vessel segment and one of the two filter outputs (see Sec. 9.2.2.2), the selected features are:

- The cross section average intensity profiles extracted from the filter output at every used scale (six values).
- The cross section average intensity profile extracted from the final filter output.
- The cross section average intensity profile extracted from the green channel of the image.
- The average intensity level computed along the segment, evaluated separately on the six filter scales, on the final filer output and on the green channel of the image (eight values).

- The standard deviation of the intensity level computed along the segment, evaluated separately on the six filter scales, on the final filer output and on the green channel of the image (eight values).

To define the average intensity profiles mentioned above, let us consider a vessel segment that can be expressed in curvilinear coordinates as a curve $S(i)$, $i \in [1, \dots, N_s]$. For every i, we extract a profile P_i^s orthogonal to the direction of $S(i)$ and centered in $S(i)$. All the P_i^s profiles extracted for the segment are averaged to obtain the average intensity profile P^s .

The average intensity level along the segment is computed by averaging the intensity values in $S(i)$ and similarly for the standard deviation of the intensity level along the segment. Given the output of a filter, all the described features are collected for every vessel segment in the training set and used along with the known segments class label to train the SVM model.

Two models M_1 and M_2 are estimated, using the data extracted from the output of the symmetric and the asymmetric LoG filters respectively. Given an estimated model M_i and a new vessel segment T, the features extracted from T are used as input to M_i in order to obtain a classification for T as "vessel" or "non-vessel".

As described in the following sections, predictions provided by the two models M_1 and M_2 on new segments will be combined to obtain the final classification results.

Training the Models

There are two parameters to be estimated for an RBF kernel: C and γ. It is not known beforehand which C and γ are best for a given problem; consequently, some kind of model selection (parameter search) must be done. The goal is to identify good (C, γ) so that the classifier can accurately predict unknown data (i.e. testing data). As discussed above, a common strategy is to separate the data set into two parts, of which one is considered unknown. The prediction accuracy obtained from the "unknown" set reflects the performance on classifying an independent data set. An improved version of this procedure is known as cross-validation and it was applied during the training phase in order to assess the accuracy of the learned model.

In v-fold cross-validation, we first divide the training set into v subsets of equal size. Sequentially one subset is tested using the classifier trained on the remaining v-1 subsets. Thus, each instance of the whole training set is predicted once, so the cross-validation accuracy is the percentage of data which are correctly classified. Other than providing a reliable classification accuracy for the trained model, the cross-validation procedure can prevent the overfitting problem.

We set $v = 5$ and a grid-search on C and γ using cross-validation was performed. Various pairs of (C, γ) values were tried and the one with the best cross-validation accuracy was chosen. A coarse grid was first used for the two parameters

($C = 2^{-5}, 2^{-3}, 2^{-1}, 2, 2^{3}, \ldots, 2^{19}$ and $\gamma = 2^{-15}, 2^{-13}, \ldots, 2^{5}$) and after identifying a "good" region on the grid, a finer grid search on that region was used.

For the model M_1 (obtained using the symmetric LoG filter) we obtained a cross validation accuracy of 82.7 % and for M_2 (obtained using the asymmetric LoG filter) we obtained a cross validation accuracy of 85.1 %.

Combining the two Models to Classify new Data

After using the models M_1 and M_2 to classify unknown segments in the testing set, we observed that both of them misclassified some true vessel as "non-vessel" and some false vessel as "vessel", but somehow the two models seemed to be complementary. So we decided to combine the two predictions in order to get a more correct final classification for unknown segments.

Given an image I, let us define V_1 and V_2 the set of vessel segments belonging to I classified as "vessels" by M_1 and M_2 respectively. Let $V_{1*2} = V_1 \cap V_2$, and $V_{1+2} = V_1 \cup V_2$. Finally let V_I be the set of all the segments extracted with both the symmetric and asymmetric LoG filters on image I.

V_{1*2} contains the segments that are most likely to be "vessels" since they are confirmed by both the models. Starting from this, we created a new set V_{1c2} by adding to V_{1*2} the segments belonging to $\{V_{1+2} \setminus V_{1*2}\}$ that touch some segment in V_{1*2} at least with one end-point. In this way, segments that are misclassified as "non-vessels" by only one of the two models are recovered, as long as they are connected to the initial network composed by the segments that are most likely "vessels". At the same time, the small and isolated segments, originating from noise or artifacts, that are misclassified as "vessels" by one model, are eliminated.

Finally, we created a new set V_{FINAL} by adding to V_{1c2} the segments in $\{V_I \setminus V_{1c2}\}$ that touch some segment in V_{1c2} with both end-points. In this way, segments that are misclassified as "non-vessels" by both models are recovered, as long as they link disconnected vessels in the network previously extracted.

In Figure 9.6 the final tracking result is presented for a RetCam image. The improvement brought by the new proposed method (with respect to the multidirectional graph search approach in RetCam images) can be qualitatively appreciated by comparing this image with Figure 9.2.

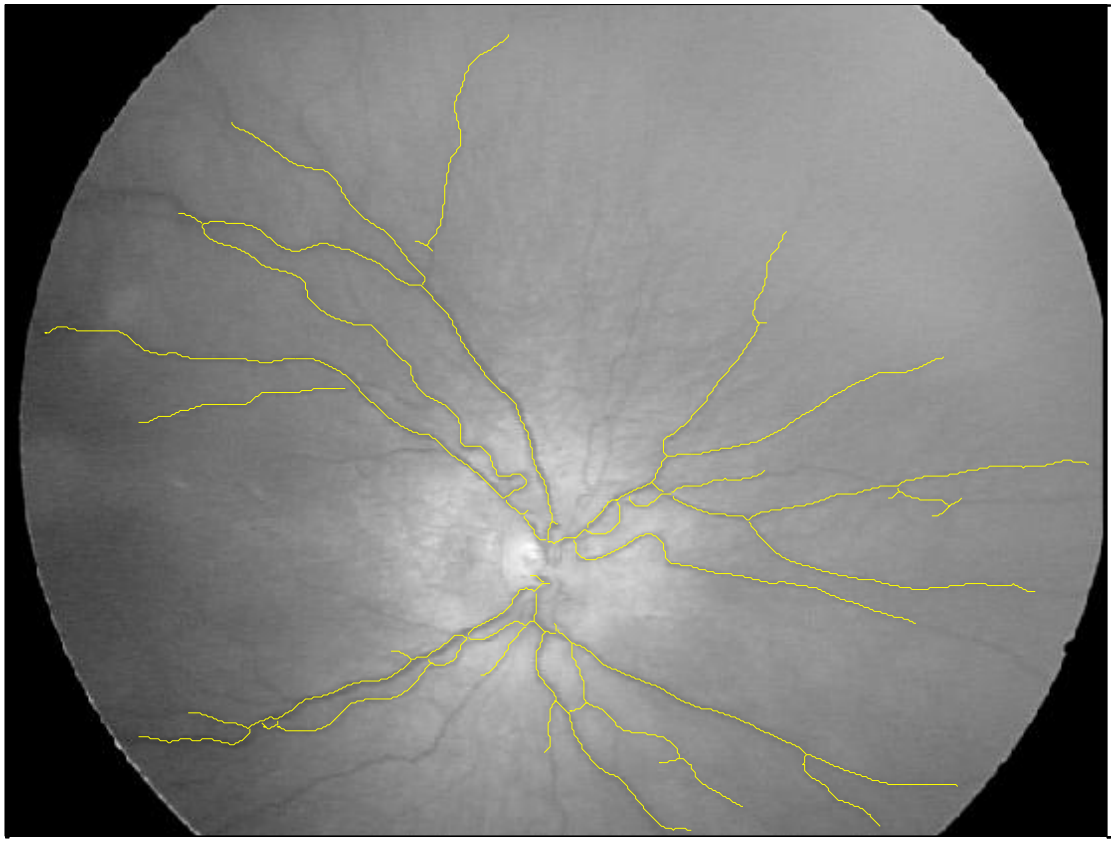

Figure 9.6 The final tracking result on a RetcCam image after combining the classification of the two estimated SVM models.

9.3 Results

Vessels manually traced in the ground-truth images were compared with vessels automatically detected by the proposed algorithm, in order to evaluate its *sensitivity* and *false vessel detection*.

The *sensitivity* is defined as the fraction of the length of correctly detected vessels over the total length of the ground-truth vessels. The *false vessels detection* is defined as the fraction of the length of the false vessels over the length of all detected vessels.

In Table 9.1, average, maximum and minimum sensitivity and false vessel detection are reported for the complete set of 20 images:

	AVERAGE	**MIN**	**MAX**
SENSITIVITY	0.7259	0.5455	0.9714
FALSE VESSEL DETECTION	0.1971	0.0761	0.5216

Table 9.1: Average, maximum and minimum sensitivity and false vessel detection for the complete set of 20 images.

In Table 9.2, average, maximum and minimum sensitivity and false vessel detection rate are reported only for the 14 images belonging to the testing set:

	AVERAGE	**MIN**	**MAX**
SENSITIVITY	0.7141	0.5455	0.9714
FALSE VESSEL DETECTION	0.2106	0.0761	0.5216

Table 9.2: Average, maximum and minimum sensitivity and false vessel detection for the testing set images.

The results obtained by the proposed method are satisfactory, as on average more than 70% of the retinal vessels are correctly detected and only 20% of the detected vessels are false detections.

The high variability of the results (e.g., see MIN vs MAX for the two performance parameters) is a direct consequence of the high variability in the quality of the 20 images. In fact, the dataset includes images with different contrast between vessels and background, different illumination and variable retinal transparency (leading to variable visibility of choroidal vessels).

Since there is a minimal difference between the mean *sensitivity* and *false vessel detection* values computed for the whole set of images and for the testing set only, we can deduce that the six images chosen as training set represented a good sampling set, able to summarize the features of the whole set of 20 ground truth images.

9.4 Conclusion

In order to automatically segment the vessel network in wide FOV infant images we first tried the multidirectional graph search approach initially designed for the analysis of good quality adult retina images. As described in Sec. 9.2.1 the algorithm turned out to be unsuitable for RetCam infant images and we tried to tune some parameters in order to improve the tracking performance. Even in this case, in spite of a good sensitivity (75%), the method provided a very high false vessel detection percentage (33%) that suggested moving toward a novel customized technique.

The proposed novel approach includes a preprocessing step to enhance the image quality. Two LoG filters are applied and the vessels are extracted by means of morphological operations. As a last step the vascular segments are classified as true or false vessels using a Support Vector Machines (SVM) supervised approach. The sensitivity of such method on the testing set is 71%, which is slightly lower than the sensitivity obtained with the multidirectional graph search approach. On the other side, the false vessel detection percentage is now 21%, which represents a significant improvement with respect to the multidirectional graph search approach.

It is worth noticing that the tracking sensitivity obtained in RetCam images is comparable to the sensitivity reached by algorithms tested on some publicly available adult image datasets, such as DRIVE and STARE. However, to our knowledge, there is no public image dataset of RetCam images, so at this time it is not possible to compare the performance of the proposed technique against other methods presented in literature.

Moreover, to our knowledge, not many tracking algorithms in literature were tested on wide FOV infant images acquired with RetCam, and only a very few authors reported quantitative performance. Namely, Heneghan et al. in [47] reported very high sensitivity and specificity, but they were computed on a very small 260 x 260 pixel selection of a typical wide FOV image.

A fundamental aim in the analysis of RetCam images acquired from newborns is to obtain clinical indexes that can improve the diagnosis and follow-up of ROP. The results of this work are only the first step towards the more complete objective. Computation of tortuosity of the blood vessels and classification of images into different ROP severity categories will be the important future steps.

Moreover, in order to provide the clinicians with a tool that automatically provides the value of parameters describing the real condition of the eye and the stage of the disease, a further important step will be to deploy the software along with an intuitive and easy to use interface.

Chapter 10

Conclusions

10.1 Achievement of the Objectives

The aim of this project was to develop a set of algorithms for the automatic analysis of the vessel network in different kind of retinal images and to implement intuitive and easy to use software systems in order to help clinicians in the diagnosis and the follow up of retinopathies.

Images acquired from adults and infants present different characteristics: this is related to the anatomical differences, but also to the different fundus cameras used for image acquisition and to the various acquisition protocols. As a consequence, algorithms designed to analyze adult retinal images usually turn out to be unsuitable with newborns images. Therefore, we developed algorithms customized for the different kinds of images to analyze and, in particular, in this thesis we presented three systems, designed respectively for the analysis of adult images, small FOV infant images acquired with Nidek NM200D and wide FOV infant images acquired with RetCam.

Starting from the mentioned analysis methods we implemented two intuitive and easy to use software systems for the extraction of geometrical parameters having clinical relevance.

The achievements obtained will be summarized in the following sections.

10.1.1 Retinal Vessel Network Extraction in Adult and Infant Images

Most of the early symptoms indicating the onset of retinopathies are related to morphological features of the retinal vascular tree. In order to detect and quantitatively describe these diagnostic signs, the layout and the dimension of all the relevant vessels contained in the image has to be extracted.

The rationale of our method for the analysis of adult images was to consider the image as a weighted un-oriented sparse graph where each node represents a pixel. The graph edges describe the 8-adjacency among pixels in the image. Under the assumption that vessels are minimum cost paths connecting remote nodes, we employed

a graph search approach in order to identify their axes (Chapter 4). Then the vessel diameters are extracted by means of an efficient mono-dimensional matched filtering approach. The orientation of the filter kernel is chosen according to the information provided by the axis and the appropriate scale is computed by means of an initial diameter estimation performed on the vessels cross section profiles before the filtering process (Chapter 5).

Many automatic techniques for vessel identification have been proposed in the literature, with various degrees of complexity and accuracy (Sec. 4.1). The motivations that lead to the development of a new method can be summarized in three points: computational speed, robustness against non-connected vessels, flexibility to accommodate different magnification and resolution of retinal adult images.

These points were solved by using a tracking technique, which analyzes portion of images only in the surrounding of already identified vessel points. This approach allowed the evaluation of a small fraction of all image pixels. The tracking of non-connected vessels, due to presence of retinal lesions or to focal decrease in image contrast, requires the tracking procedure to start from different points along a vessel. This is achieved by using a sparse approach, in which a set of widespread starting points (seeds) within an image is identified. These seeds provide the mean to track every vessel even if not connected from the vessel tree, with reasonable chance. The vessel caliber extraction provided by the matched filters and fuzzy c-means clustering approach solves the problem of identifying contrast variation along a vessel, and of tuning the algorithm parameters for different image sources. Appropriate kernel orientation and scale are preventively evaluated, in order to improve the filter precision and efficiency. Then, an adaptive correction step allows managing critical situations (presence of noise, lack of contrast, *etc...*) in which the algorithm would fail to detect the correct diameters.

In Chapter 7 an *ad-hoc* method is presented for the analysis of newborns images acquired with Nidek NM200D. Because of the large variability and the poor quality of such images we opted for a semi-automatic approach to perform tracking on vessels and to quantitatively assess vascular tortuosity and width. Vessels to be analyzed are selected by manually drawing an approximate centerline inside their boundaries. Starting from this *a priori* information, the vessel edges are detected by means of a filtering technique based on Canny method. Refined axis and calibers along the vessel are then obtained by appropriately linking pairs of points on opposite edges.

To our knowledge there are not automatic methods in literature presenting results on Nidek NM200D infant images. Some semi-automatic methods were presented and all of them perform a first tracking procedure and then ask the user to manually correct and complete the identified vascular structures and to discard false vessels originating from noise or image artifacts (which can be a long and tedious task with this kind of images). We tried to change this common procedure in order to make the analysis more direct and efficient. As the first step the user is asked to manually identify only the vessel portions considered important for the clinical evaluation and

the method provides precise and objective information about every single vessel selected.

In Chapter 9 a novel method is proposed for the automatic extraction of the vessel axis network in RetCam images acquired from newborns. The technique includes a preprocessing step to enhance the image quality. The interlacing artifacts are removed with a deinterlacing algorithm and the vascular structures are emphasized by means of LoG filters. The vessels are extracted by means of morphological operations and the vascular segments are classified as true or false vessels using an SVM supervised approach. The algorithm performance in terms of sensitivity and false vessel detection percentage can be considered promising but further steps will be necessary, in order to exploit the geometrical characteristics of the network to compute a tortuosity clinical index and to classify images into different ROP gravity categories..

10.1.2 Tools for Clinical Use

With sustained hypertension, vessel walls are damaged and the morphology of the vascular tree changes as a consequence of the increased hydrostatic pressure. This damage and changes, lead to the appearance of specific signs as generalized narrowing and vessel tortuosity. These signs usually appear long before any malignant hypertensive retinopathy, and therefore all these vascular changes have to be identified and evaluated, in order to provide a sensible and robust diagnostic and prognostic tool to evaluate the retinopathy.

In Chapter 6, we described a computerized system to quantitatively assess the CRAE, CRVE and AVR parameters in retinal images from normal, hypertensive or diabetic adult subjects. Its purpose is to allow clinicians to recover the quantitative estimation of these parameters in an objective, fast and user-friendly way. The first phase performs the vascular network segmentation by means of the algorithm proposed in Chapter 4 and Chapter 5, coupled with an artery/vein classifier. In the second phase, the user evaluates the results provided and confirms them or applies the needed corrections via a user-friendly editing interface, which is capable of detecting the troubled situations to be presented to the user for expert assistance. The vascular parameters are finally computed. Repeatability and accuracy of the complete system were assessed by having three users independently analyze retinal images from the database provided by the University of Wisconsin, whose analysis results were used as reference for accuracy. The overall repeatability between users and accuracy with respect to reference results were assessed by the correlation coefficients.

Retinopathy of prematurity (ROP) is a potentially blinding disease that occurs in premature infants, and affects the postnatal maturation of the retinal blood vessels. Many significant pathological signs have been identified for ROP, including an abnormal increase in vessel width and tortuosity. Expert screening by pediatric ophthalmologists or retina specialists for repeated exams to detect treatment-requiring

disease according to the evolving definitions is crucial. Such screening is not always directly available for the lack of experts at the neonatal intensive care units.

In Chapter 8 we proposed a web based system to objectively assess the vessel width and tortuosity in retinal images acquired with Nidek NM200D in both normal and diseased infants with ROP. The aim of the tool is to allow clinicians to estimate the ROP signs in a quantitative and reproducible way, with a fast and easy to use interface.

At the beginning of the procedure, the client can choose an image from the local drivers and upload it to the server. After image submission, a GUI is automatically loaded on client-side, to provide for manual input. The GUI allows the client to select the vessel to be analyzed and to set up some parameters useful for the subsequent analysis. As second step the selected vessels are segmented by the algorithm presented in Chapter 7, running server-side. The vascular parameters are finally computed and displayed to the user's browser by means of a second GUI. Repeatability and accuracy of the complete system were assessed by having three users independently analyze retinal vessels from the databases provided by the Scheie Eye Institute and by the Children Hospital of Philadelphia. The overall repeatability between users and accuracy with respect to reference results were assessed by the Pearson's correlation coefficients, the p-values from ANOVA and paired t-tests and the ICC analysis.

10.2 Final Summary and Collaborations

This thesis concentrated on the extraction and the analysis of the features of the vascular apparatus: the vessel network identification (veins and arteries) will allow the assessment of its main geometrical characteristics (length, direction, caliber, bifurcation, tortuosity, etc.). From these findings, specific indexes of diagnostic relevance have been computed, providing the clinicians with information regarding the patient's retinopathy degree, whose significance is crucial for the diagnosis of retinal pathologies.

We developed algorithms customized for the different kinds of images to analyze, in order to achieve satisfactory performance regardless of the varying attributes related to the acquisition system or to the patient age. In particular, in this thesis we presented three systems, designed respectively for the analysis of adult images, infant images acquired with Nidek NM200D and infant images acquired with RetCam.

Starting from the proposed algorithms for image analysis, we developed two easy-to-use software systems, AVRnet and ROPnet, aimed at supporting the clinicians with the screening and the diagnosis of retinopathies.

AVRnet was proposed for the analysis of adult retinal images and it is currently the object of clinical evaluation at the Department of Ophthalmology and Visual Sciences, University of Wisconsin, USA, the world leading center for clinical trial re-

tinal image analysis, whose Fundus Photograph Reading Center is considering the adoption of the system as standard tool for the extraction of diagnostic features.

In addition, a recent collaboration with the Department of Twin Research & Genetic Epidemiology, of the King's College London Division of Genetics and Molecular Medicine, St Thomas' Hospital, UK, has involved the analysis of more than 2000 retinal fundus images with our software for the estimation of clinical indexes in retinal vessels.

The interface and the functionality of ROPnet have been designed in collaboration with the Departments of Ophthalmology of the Children's Hospital and the Scheie Eye Institute of Philadelphia, US, with the aim of meeting the requirements of the clinicians for what concerns both the tool performance and usability. The accuracy of parameters extracted by ROPnet (i.e. vessel width and tortuosity) was confirmed by the high correlation obtained comparing automatic results with a ground truth manually provided by retina experts. Moreover, the web tool was already used for some preliminary clinical study and we are currently investigating the reliability of extracted clinical indexes for the diagnosis and classification of ROP.

The system specifications for the analysis of ROP images acquired with RetCam were discussed directly with Clarity Medical Systems, the manufacturer of the mentioned fundus camera. In this project, we obtained on a preliminary set of images high sensitivity and specificity in the retinal vessel segmentation, which is a particularly difficult task on RetCam infant images. The techniques for the extraction of clinical parameters starting from the vessel morphology are currently under development.

In perspective, practical and easily deployable tools such as those we propose might significantly contribute to the mass-screening and the monitoring of the progression of hypertensive/diabetic retinopathies and of ROP.

The results achieved in the preliminary trials, carried out in cooperation with relevant international clinical research groups, attest the quality of the developed methodologies and bode well for their future clinical adoption.

References

[1] C. Gilbert, A. Fielder, L. Gordillo, G. Quinn, R. Semiglia, P. Visintin, and A. Zin, Characteristics of infants with severe retinopathy of prematurity in countries with low, moderate, and high levels of development: implications for screening programs. Pediatrics, (May 2005); 115(5): e518-25.

[2] J. A. Pugh, J. M. Jacobson, W. A. J. Van Heuven, J. A. Watters, M. R. Tuley, D. R. Lairson, R. J. Lorimor, A. S. Kapadia, and R. Velez, Screening for diabetic retinopathy. the wide angle retinal camera, Diabetes Care 16 (1993), no. 6, 889-895.

[3] D. J. Taylor, J. Fisher, J. Jacob, and J. E. Tooke, The use of digital cameras in a mobile retinal screening environment., Diabetic Medicine 16 (1999), 680-686.

[4] H. M. Herbert, K. Jordan, and D. W. Flanagan, Is screening with digital imaging using one retinal view adquate?, Eye 17 (2003), no. 3, 497-500.

[5] L. Varma, G. Prakash, and H. K. Tewari, Diabetic retinopathy: time for action. no complacency, please!, Bullettin of the World Health Organization 80 (2002), 419.

[6] C. D. Murray, The physiological principle of minimum work. i. the vascular system and the cost of blood volume., Proceedings of the National Academy of Science 12 (1926), 207-214.

[7] A. V. Stanton, B. Wasan, A. Cerutti, S. Ford, R. Marsh, P. P. Sever, S. A. Thom, and A. D. Hughes, Vascular network changes in the retina with age and hypertension, Journal of Hypertension 13 (1995), 1724-1728.

[8] Early Treatement Diabetic Retinopathy Study Research Group, Grading diabetic retinopathy from stereoscopic fundus photographs - an extension of the modified airlie house classification. Ophthalmology 98 (1991), 786-806.

[9] N. M Keith, H. P. Wegener, and N. W. Barker, Some different types of essential hypertension: their course and prognosis, American Journal of Medicine Science 197 (1939), 336-354.

[10] H. G. Scheie, Evaluation of ophthalmoscopic changes of hypertension and arterial sclerosis, Archives of Ophthalmology 49 (1953), no. 2, 117-138.

[11] S. Chatterjee, S. Chattopahya, M. Hope-Ross, and P. L. Lip, Hypertensionand the eye: changing perspectives, Journal of Human Hypertension 16 (2002), 667-675.

[12] The Diabetic Retinopathy Study Research Group, A modification of the airlie house classification of diabetic retinopathy, Investigative Ophthalmology and Visual Science 21 (1981), 210-226.

[13] Early Treatment Diabetic Retinopathy Study Research Group, Early treatment diabetic retinopathy study design and baseline patient characteristics, Ophthalmology 98 (1991), 741-756.

[14] C. P. Wilkinosn, F. L. Ferries, R. E. Klein, P. P. Lee, C. D. Agardh, M. Davies, D. Dills, A. Kampik, R. Pararajasegaram, and J. T. Vardaguer representing the global Diabetic Retinopathy Project Group, Proposed international clinical diabetic retinopathy and diabetic macular edema disease severity scale, Ophthalmolgy 110 (2003), 1677-1612.

[15] Committee for the Classification of Retinopathy of Prematurity, The International Classification of Retinopathy of Prematurity revisited. Arch Ophthalmol. 123 (2005) no. 7, 991–999.

[16] J.J. Staal, M.D. Abramoff, M. Niemeijer, M.A. Viergever, B. van Ginneken, "Ridge based vessel segmentation in color images of the retina", IEEE Transactions on Medical Imaging, 2004, vol. 23, pp. 501-509.

[17] M. Niemeijer, J.J. Staal, B. van Ginneken, M. Loog, M.D. Abramoff, "Comparative study of retinal vessel segmentation methods on a new publicly available database", in: SPIE Medical Imaging, Editor(s): J. Michael Fitzpatrick, M. Sonka, SPIE, 2004, vol. 5370, pp. 648-656.

[18] A. Hoover, V. Kouznetsova, M. H. Goldbaum, Locating Blood Vessels in Retinal Images by Piece-wise Threhsold Probing of a Matched Filter Response, IEEE Transactions on Medical Imaging, (March 2000) vol. 19 no. 3, pp. 203-210

[19] The DCCT Group, Color photography vs. fluorescein angiography in the detection of diabetic retinopathy in the Diabetes Control and Complications Trial, Arch Ophthalmol. (1987) 105: 1344-51.

[20] Early Treatment Diabetic Retinopathy Study Research Group, Grading diabetic retinopathy from stereoscopic fundus photographs- an extension of the modified Airlie House classification, Ophthalmology (1991) 98: 786-806.

[21] L. Tramontan, A. Ruggeri, “Computer Estimation of the AVR Parameter in Diabetic Retinopathy” IFMBE Proceedings WC 2009 “World Congress on Medical Physics and Biomedical Engineering”, Vol. 25, (2009), Munich, Germany

[22] S. Bursell, J. D. Cavallerano, A. A. Cavallerano, A. C. Clermont, D. Birkmire-Peters, L. P. Aiello, L. M. Aiello, and the Joslin Vision Network Research Team, Stereo nonmydriatic digital-video color retinal imaging compared with early treatement diabetic retinopathy study seven standard field 35-mm stereo color for determining level of diabetic retinopathy, Ophthalmology 108 (2001), no. 3, 572-585.

[23] L. D. Hubbard, R. J. Brothers, W. N. King, L. X. Clegg, R. Klein, L. S. Cooper, A. R. Sharrett, M. D. Davis, and J. Cai, Methods for evaluation of retinal microvascular abnormalities associated with hypertension/sclerosis in the atherosclerosis risk in communities study, Ophthalmology 106 (1999), no. 12, 2269-2280.

[24] M. Sonka, M. D. Winniford, and S. M. Collins, Robust simultaneous detection of coronary borders in complex images, IEEE Transactions on Medical Imaging 14 (1995), no. 1, 151-161.

[25] P. H. Eichel, E. J. Delp, K. Koral, and A. J. Buda, A method for a fully automatic definition of coronary arterial edges from cineangiograms, IEEE Transactions on Medical Imaging 7 (1998), no. 4, 313-320.

[26] E. Grisan, M. Foracchia, and A. Ruggeri, Normalization of luminance and contrast in fundus images. Medical Image Analysis (2003) 2: 179-190

[27] I. Liu and Y. Sun, Recursive tracking of vascular networks in angiograms based on the detection-deletion scheme, IEEE Transactions on Medical Imaging 12 (1993), no. 2, 334-341.

[28] F. P. Miles and A. L. Nuttall, Matched filter estimation of serial blood vessel diameters from video images, IEEE Transactions on Medical Imaging 12 (1993), no. 2, 147-152.

[29] M. A. T. Figueiredo and J. M. N. Leitao, A non smoothing approach to the estimation of vessel contours in angiograms, IEEE Transactions on Medical Imaging 14 (1995), no. 1, 162-172.

[30] T. N. Pappas and J. S. Lim, A new method for estimation of coronary artery dimensions in angiograms, IEEE Transactions on Acoustics, Speech, and Signal Processing 36 (1988), no. 9, 1501-1513.

[31] Y. Sun, Automated identification of vessel contours in coronary arteriograms by an adaptive tracking algorithm, IEEE Transactions on Medical Imaging 8 (1989), no. 1, 78-88.

[32] S. R. Fleagle, M. R. Johnson, C. J. Wilbricht, D. J. Skorton, R. F. Wilson, C. W. White, M. L. Marcus, and S. M. Collins, Automated analysis of coronary arterial morphology in cineangiograms: Geometric and physiologic validation in humans, IEEE Transactions on Medical Imaging 8 (1989), no. 4, 387-400.

[33] M. Sonka, C. J. Wilbricht, S. R. Fleagle, S. K. Tadikonda, M. Winniford, and S. M. Collins, Simultaneous detection of both coronary borders, IEEE Transactions on Medical Imaging 12 (1993), no. 3, 588-599.

[34] Y. Sun, R. J. Lucariello, and S. A. Chiaramida, Directional low-pass filtering for improved accuracy and reproducibility of stenosis quantification in coronary arteriograms, IEEE Transactions on Medical Imaging 14 (1995), no. 2, 242-248.

[35] K. V. Chandrinos, M. Pilu, R. B. Fisher, and P.E. Trahanias, Image processing techniques for the quantification of atherosclerotic changes, Proceedings MEDICO98 (June 1998) (Limassol, Cyprus).

[36] A. Sen, L. Lan, K. Doi, and K. R. Hoffmann, Quantitative evaluation of vessel tracking techniques on coronary angiograms, Medical Physics 26 (1999), no. 5, 698-706.

[37] S. Chaudhuri, S. Chatterjee, N. Katz, M. Nelson, and M. Goldbaum, Detection of blood vessels in retinal images using two-dimensional matched filters, IEEE Transactions on Medical Imaging 8 (1989), no. 3, 263-269.

[38] L. Zhou, S. Rzeszotarski, L. J. Singermann, and J. Chokreff, The detection and quantification of retinopathy using digital angiograms, IEEE Transactions on Medical Imaging 13 (1994), no. 4, 619-626.

[39] Y. A. Tolias and S. M. Panas, A fuzzy vessel tracking algorithm for retinal images based on fuzzy clustering, IEEE Transactions on Medical Imaging 17 (1998), no. 2, 263-273.

[40] A. Can, H. Shen, J. N. Turner, H. L. Tanenbaum, and B. Roysam, Rapid automated tracing and feature extraction from retinal fundus images using direct exploratory algorithms, IEEE Transactions on Information Technology in Biomedicine 3 (1999), no. 2, 125-138.

[41] J.-H. Yu, B.-N. Hung, and H.-C. Sun, Automatic recognition of retiopathy from retinal images, Proceedings of the annual international conference IEEE/EMBS 1990, IEEE, 1990, pp. 171-173.

[42] Y. Wang and S. C. Lee, A fast method for automated detection of blood vessels in retinal images, Proceedings of the 31st Asilomar Conference on Signal, System, and Computers, 1997.

[43] M. E. Martinez-Perez, A. D. Hughes, A. V. Stanton, S. A. Thom, A. A. Bharath, and K. H. Parker, Scale-space analysis for the characterization of retinal blood vessels, MIUA99 On-line proceedings (http://www-ipg.umds.ac.uk/miua/proceedings/IE index.html), Medical Image Understanding and Analysis (July 1999).

[44] M. Goldbaum, N. Katz, S. Chatterjee, and M. Nelson, Image understanding for automated retinal diagnoses, IEEE Symposium for computer applications in clinical medicine, (1989), pp. 756-760.

[45] T. Chanwimaluang and G. Fan, "An efficient algorithm for extraction of anatomical structures in retinal images", Proceedings of the IEEE International Conference on Image Processing (Barcelona, (ES)), (September 2003).

[46] N. Patton, T. M. Aslam, T. Macgillivray, I. J. Deary, B. Dhillon, R. H. Eikelboom, et al. Retinal image analysis: concepts, applications and potential, Prog Retin Eye Res (2006); 25:99–127.

[47] C. Heneghan, J. Flynn, M. O'Keefe, and M. Cahill, Characterization of changes in blood vessel width and tortuosity in retinopathy of prematurity using image analysis, Medical image analysis 6 (2002), 407-429.

[48] B. Kochner, D. Schuhmann, M. Michaelis, G. Mann, K-H. Englmeier, Course tracking and contour extraction of retinal vessels from color fundus photographs: most efficient use of steerable filters for model based image analysis, SPIE conference image processing, (1998) vol. 3338. p. 755–61.

[49] J. Lowell, A. Hunter, D. Steel, A. Basu, R. Ryder, R. L. Kennedy, Measurement of retinal vessel widths from fundus images based on 2-D Modeling, IEEE Trans Med Imaging (2004); 23:1196–204.

[50] C-W. Yang, D-J. Ma, S-C. Chao, C-M. Wang, C. H. Wen, S. C. Lo, et al., A computeraided diagnostic detection system of venous beading in retinal images. Opt Eng (2000); 39:1293–303.

[51] F. Zana, J. Klein, A multimodal registration algorithm of eye fundus images using vessels detection and Hough transform, IEEE Trans Med Imaging (1999); 18:419–28.

[52] P. Gregson, Z. Shen, R. Scott, V. Kozousek, Automated grading of venous beading. Comput Biomed Res (1995); 28:291–304.

[53] A. M. Mendonca, and A. Campilho, Segmentation of retinal blood vessels by combining the detection of centerlines and morphological reconstruction, IEEE Trans. Med. Imaging (2006) 25(9): 1200-1213.

[54] K. Akita, H. Kuga, A computer method of understanding ocular fundus images. Pattern Recognit (1982); 15:431–43.

[55] G. Gardner, D. Keating, T. Williamson, and A. Elliot, Automatic detection of diabetic retinopathy using an artificial neural network: a screening tool, British Journal of Ophthalmology 80 (1996), 940-944.

[56] C. Sinthanayothin, J. F. Boyce, H. L. Cook, T. H. Williamson, Automated localization of the optic disc, fovea, and retinal blood vessels from digital color fundus images. Br J Ophthalmol (1999); 83:902–10.

[57] J. V. B. Soares, J. J. G. Leandro, R. M. Cesar Jr., H. F. Jelinek and M. J. Cree Retinal vessel segmentation using the 2D Gabor wavelet and supervised classification, IEEE Trans. Med. Imag., (Sep. 2006) vol. 25, pp. 1214-1222.

[58] E. Ricci, and R. Perfetti, Retinal blood vessel segmentation using line operators and support vector classification, IEEE Trans. Med. Imag. v26. 1357-1365.

[59] E. W. Dijkstra, A note on two problems in connection with graphs, Numerische Mathematik, (1959) 1:269--271.

[60] L. Sint and D. de Champeaux, An Improved Bidirectional Heuristic Search Algorithm, J. ACM 24, 2 (Apr. 1977), pp 177-191.

[61] C. Sun and S. Pallottino, Circular shortest path in images, Pattern Recognition, (March 2003) vol. 36, no. 3, pp. 711--721.

[62] A. Frangi et al., Multiscale vessel enhacement filtering, Medical Image Computing and Computer-Assisted Intervention (1995) 1496: 130-137

[63] S. M. Kay, Fundamentals of Statistical Signal Processing. New Jersey: Prentice-Hall (1998).

[64] M. Sofka and C. V. Stewart, Retinal vessel centerline extraction using multiscale matched filters, confidence and edge measures, IEEE TMI (2006) 25: 1531-1546.

[65] M. Jacob and M. Unser, Design of steerable filters for feature detection using canny-like criteria. IEEE Trans. on Pattern Analysis and Machine Intelligence (2004) 26(8):1007-1019.

[66] C. Tomasi and R. Manduchi, Bilateral Filtering for Gray and Color Images. Proceedings of the Sixth International Conference on Computer Vision (1998) 839-846.

[67] J. C. Dunn, A Fuzzy Relative of the ISODATA Process and Its Use in Detecting Compact Well-Separated Clusters, Journal of Cybernetics (1973) 3(3): 32-57.

[68] M. D. Knudtson, K. E. Lee, L. H. Hubbard, T. Y. Wong, R. Klein, B. E. K. Klein, Revised formulas for summarizing retinal vessel diameters, Current Eye Research, (2003) vol. 27, no. 3: 143-149.

[69] T. Y. Wong, M. Knudtson, R. Klein, B. E. K. Klein, S. M. Meuer, L. D. Hubbard, Computer-assisted measurement of retinal vessel diameters in the Beaver Dam eye study, Ophthalmology, (2004) vol. 111: 1183–90.

[70] H. Li, W. Hsu, M. L. Lee, T. Y. Wong, Automatic grading of retinal vessel caliber, IEEE Trans Biomed Eng, (2005) vol. 52: 1352-5.

[71] W. C. Owens, E. U. Owens, Retrolental fibroplasia in premature infants, Am J Ophthalmol (1949); 32:1–18.

[72] J. D. Baum, Retinal photography in premature infants: forme fruste retrolental fibroplasia. Proc Roy Soc Med (1971); 64:777–9.

[73] J. D. Kingham, Acute retrolental fibroplasia, Arch Ophthalmol (1977); 95:39–47.

[74] Y. Uemura, Current status of retrolental fibroplasia: report of the joint committee for the study of retrolental fibroplasia in Japan, Jpn J Ophthalmol (1977); 21:366–78.

[75] D. B. Schaffer, L. Johnson, G. E. Quin, et al. A classification of retrolental fibroplasia to evaluate vitamin E therapy, Am J Ophthalmol (1979); 86:1749–60.

[76] R. A. Saunders, E. C. Bluestein, R. B. Sinatra, et al. The predictive value of posterior pole vessels in retinopathy of prematurity, J Pediatr Ophthalmol Strabismus (1995); 32:302–4.

[77] Joint Working Party of the Royal College of Ophthalmologists and British Association of Perinatal Medicine. Retinopathy of Prematurity: guidelines for Screening and Treatment, Early Hum Dev (1996); 46:239–58.

[78] J. J. Capowski, J. A. Klystra, S. F. Freedman, A numerical index based on spatial frequency for the tortuosity of retinal vessels and its application to plus disease in retinopathy of prematurity, Retina (1995); 15:490–500.

[79] D. K. Wallace, J. A. Kylstra, D. A. Chesnutt, Prognostic significance of vascular dilation and tortuosity insufficient for plus disease in retinopathy of prematurity, J AAPOS (2000); 4:224–9.

[80] S. F. Freedman, J. A. Klystra, M. S. Capowski, et al., Observer sensitivity to retinal vessel diameter and tortuosity in retinopathy of prematurity: a model system, J Pediatr Ophthalmol Strabismus (1996); 33:248–54.

[81] W. E. Hart, M. Goldbaum, B. Côté, P. Kube, and M. R. Nelson, Measurement and classification of retinal vascular tortuosity, International Journal of Medical Informatics 53 (1999), no. 2-3, 239-252.

[82] L. Sukkaew, B. Uyyanonvara, S. Barman, A. Fielder, K. Cocker, Automatic extraction of the structure of the retinal blood vessel network of premature infants, Journal of the Medical Association of Thailand. (2007); 90(9): 1780-92.

[83] M. E. Martinez-Perez, A. D. Hughes, A. V. Stanton, S. A. Thom, A. A. Bharath, and K. H. Parker, Retinal vascular tree morphology: a semi automatic quantification, IEEE Transactions on Biomedical Engineering 49 (2002), no. 8, 912-917.

[84] C. M. Wilson, K. D: Cocker, M. J. Moseley, et al., Computerized analysis of retinal vessel width and tortuosity in premature infants, Investigative ophthalmology & visual science (2008); 49(8):3577-85.

[85] D. K. Wallace, Computer-Assisted Quantification of Vascular Tortuosity in Retinopathy of Prematurity (an American Ophthalmological Society Thesis), Transactions of the American Ophthalmological Society (2007); 105:594-615.

[86] J. Canny, A Computational Approach To Edge Detection, IEEE Trans. Pattern Analysis and Machine Intelligence (1986), 8(6):679–698.

[87] E. Grisan, M. Foracchia, A. Ruggeri, "A novel method for the automatic grading of retinal vessel tortuosity", IEEE Transactions on Medical Imaging, (2008), 27(3), 310-319.

[88] Cryotherapy for Retinopathy of Prematurity Cooperative Group, Multicenter trial of cryotherapy for retinopathy of prematurity. One-year outcome—structure and function, Arch Ophthalmol (1990); 108:1408–16.

[89] Screening examination of premature infants for retinopathy of prematurity. A joint statement of the American Academy of Pediatrics, the American Association for Pediatric Ophthalmology and Strabismus, and the American Academy of Ophthalmology, Pediatrics (1997); 100(2 Pt I):273.

[90] Canadian Association of Pediatric Ophthalmologists Ad Hoc Committee on Standards of Screening Examination for Retinopathy of Prematurity, Guidelines for screening examination for retinopathy of prematurity, Can J Ophthalmol (2000); 35: 251–2.

[91] Retinopathy of prematurity: guidelines for screening and treatment, The report of a joint working party of the Royal College of Ophthalmologists and the British Association of Perinatal Medicine, Early Human Dev (1996); 46:239–58.

[92] D. B. Schaffer, B. Tung, R. J. Hardy, Guidelines for follow-up of retinopathy of prematurity, In: Flynn JT, Tasman W, eds. Retinopathy of Prematurity: A Clinician's Guide. New York: Springer-Verlag; (1992): 45–53.

[93] A. Ells, W. Hindle, Commentary on guidelines for screening for retinopathy of prematurity, Can J Ophthalmol (2000); 35:253–4.

[94] R. J. Hardy, E. A. Palmer, D. B. Schaffer, et al., Multicenter Trial of Cryotherapy for Retinopathy of Prematurity Cooperative Group. Outcome-based management of retinopathy of prematurity, J AAPOS (1997); 1:46–54.

[95] D. K. Wallace, J. Jomier, S. R. Aylward, M. B. Landers III, Computer automated quantification of plus disease in retinopathy of prematurity, J AAPOS (2003); 7:126-30.

[96] C. R. Swanson, K. D. Cocker, K. H. Parker, M. J. Moseley, S. M. E. Wren, A. R. Fielder, Semi-automated computer analysis of vessel growth in preterm infants without and with ROP, Br J Ophthalmol (2003); 87:1474-7.

[97] R. Gelman, M. E. Martinez-Perez, D. K. Vanderveen, A. Moskowitz, A. B. Fulton, Diagnosis of plus disease in retinopathy of using retinal image multiscale analysis, Invest Ophthalmol Vis Sci (2005); 46:4734-8.

[98] D. K. Wallace, Z. Zhao, S. F. Freedman, A pilot study using "ROPtool" to quantify plus disease in retinopathy of prematurity, JAAPOS (2007); 11(4):381-387.

[99] D. K. Wallace, S. F. Freedman, Z. Zhao, S. H. Jung, Accuracy of ROPtool vs. individual examiners in assessing retinal vascular tortuosity, Arch Ophthalmol (2007); 125:1523-30.

[100] L. M. Sherry, J. J. Wang, E. Rochtchina, T. Wong, R. Klein, L. Hubbard, P. Mitchell, Reliability of computer-assisted retinal vessel measurement in a population, Clin Experiment Ophthalmol. (2002); 30(3):179-82.

[101] B. Lorenz, K. Spasovska, H. Elflein, et al., Wide-field digital imaging based telemedicine for screening for acute retinopathy of prematurity (ROP). Six-year results of a multicenter field study, Graefes Arch Clin Ophthalmol. (2009); 247(9):1251-1262.

[102] T. H. T. Phan, A. U. Khan, L. Young-Koo, L. Sungyoung, K. Tae-Seong, Vessel enhancement filter using directional filter bank, Computer Vision and Image Understanding (2009) 113(1): 101-112.

[103] R. Haralick and L. Shapiro, Computer and Robot Vision, Vol. 1, Addison-Wesley Publishing Company, (1992), pp 346 – 351.

[104] S. S. Keerthi, and Lin C.J., Asymptotic behaviors of support vector machines with Gaussian kernel, Neural Computation, (2003) 15(7):1667-1689.

[105] C. W. Hsu, C. C. Chang, and C. J. Lin, A practical guide to support vector classification, http://www.csie.ntu.edu.tw/~cjlin/papers/guide/guide.pdf.

[106] K. S. Johnson, M. D. Mills, K. A. Karp, et al., Semiautomated analysis of retinal vessel diameter in retinopathy of prematurity patients with and without plus disease, Am J Ophthalmol. (2007); 143(4):723–725.

Acknowledgements

I am grateful to Prof. A. Ruggeri, who asked me to work on retinal image analysis, for his continuous support and encouragement. I would also like to thank Prof. E. Grisan, for inspiring and helping me with his deep experience and exciting new ideas. I would like to express my gratitude to Prof. A. Cenedese and Prof. R. Frezza, for encouraging me to undertake the doctoral experience three years ago.
A special mention is deserved by the colleagues and friends with whom I shared the office in the last years: Elisa, Enea, Lara, Luca, Parnian. This thesis would not have been possible without their cooperation and support, but most importantly, without their friendship I would be much poorer now. As Sid would say: "I don't know about you guys but we were the weirdest herd I have ever seen".
For their valuable contribution to various parts of this project, I would like to thank all the students that collaborated at it.
I am grateful to the secretaries and to the technical and administrative staff at the Departments of Information Engineering.
Finally a thanks to all the friends I met during my doctoral adventure, who shared with me happy lunch times, challenging lessons, and many happy and sad moments in the last years.
Lastly, and most importantly, I wish to thank my parents and Irene. To them I dedicate this thesis.